NORTHWESTERN UNIVERSITY

Examination and Mitigation of Electron Interception Processes in Dye-sensitized Solar Cells through Redox Shuttle and Photoelectrode Modification

A DISSERTATION

SUBMITTED TO THE GRADUATE SCHOOL IN PARTIAL FULFILLMENT OF THE REQUIREMENTS

for the degree

DOCTOR OF PHILOSOPHY

Field of Chemistry

By

William Lawrence Hoffeditz

EVANSTON, ILLINOIS

March 2017

Abstract

Examination and Mitigation of Electron Interception Processes in Dye-sensitized Solar Cells through Redox Shuttle and Photoelectrode Modification

With the dual challenges of meeting global energy demand and mitigating anthropogenic climate change, significant effort is being applied to generating power from renewable sources. The dye-sensitized solar cell (DSC) is a photovoltaic technology capable of generating electricity from sunlight, but suffers losses in efficiency due to deleterious electron transfer processes. Controlling these processes is essential if DSCs are to continue to advance, and this dissertation focuses on isolation, interrogation, and mitigation of these processes via controllable inorganic redox/coordination chemistry and atomic layer deposition (ALD).

The redox shuttle is often the subject of innovation in DSCs, the goal being to increase obtainable photovoltage without sacrificing photocurrent. A copper redox shuttle with a favorable (II/I) redox potential for DSC use and intriguing inner-sphere reorganization energy was investigated. The shuttle completely replaces its tetradentate coordinating ligand upon oxidation with multiple pyridine molecules. This new species displays markedly slower electron interception, necessitating fabrication of a new counter electrode in order for the shuttle to function. Upon reduction, the tetradentate ligand re-coordinates, creating a dual-species shuttle that outperforms either species as a Cu(II/I) shuttle in isolation.

Photoelectrode modification is also the subject of innovation in DSCs. ALD is ideally suited for this type of innovation as it can coat high aspect surfaces with metal-oxide films of uniform

thickness. The ALD post-treatment technique is described and used to deposit Al_2O_3 around a TiO_2 adsorbed zinc-porphyrin dye. This technique is shown to prevent dye degradation from ambient air and/or light. Additionally, the architecture allows the study of dye-influenced electron interception processes. It was found that the presence of dye increased interception, which was attributed to dye-mediated electron hopping and/or superexchange mechanisms.

Finally, ALD was used to fabricate thin-film Nb_2O_5, which is a promising overcoat material to potentially improved photovoltage without harming charge injection. The conduction band potential of films specifically fabricated via ALD was thus determined and compared to that of TiO_2 films fabricated by ALD. Taken together, the research presented herein increases the underlying understanding of the numerous complicated electron transfer processes in DSC-type devices and offers new strategies to combat deleterious processes, specifically electron interception.

Acknowledgements

A large number of people have helped me throughout the years I've done research at Northwestern. I want to start by thanking Professor Joe Hupp for not firing me right away and allowing me to focus on classes when I almost failed out of graduate school in the 1st quarter. I've learned a lot about numerous topics (and a lot of good jokes) from my years in his research group. Professor Mike Pellin, my co-advisor that I turned out not doing any actual work for, deserves a thank you as well, for both the aforementioned lack of work (and how he was ok with it) and the helpful discussions I know he had with Joe, even if I wasn't always there to hear them. Also thank you to Prof. Omar K. Farha for having some patience with me, of all people. My parents also demonstrated a large amount of patience, asking only on rare occasions when I would be finished and not pursuing the topic further once answered. But that's not why I'm thanking them, it's just an anecdote to show how awesome they are. That's why I'm thanking them: because they are awesome parents and I'm lucky to have them.

The biggest acknowledgement goes to Prof. (née post doc) Mike Katz, who was a strong friend and excellent mentor in our time together. He taught me a lot of good stuff about how to think about and actually be excited about your science. Jason Avila also deserves a shout out. I've had to refigure out how to do a lot of things since he's no longer around to ask. He's also a solid friend, even if his dog never lets me pet her. Reaching way back into 2011, Chaiya Prasittichai was helpful in getting started with my projects here and himself laid a good amount of the groundwork necessary to take some of my work where it ended up going

I've made numerous friends in my time at NU, and several deserve specific mentions, especially "the hosts with the mosts" Scotty and Alyssa Dyar, George E. Cutsail 3h.D, Cliff "I like the hours at Intel" Engel, and Henry HEITZER! Heitzer. Eric "What time are you heading home" Margulies, Brandon "let's talk about stuff I'd rather not discuss in public in the hallway" Rugg, Stephanie "Tiny Jew" Zaleski, Cao Hanh "Dana" Duyen, America Joe Christenson, Princess Rachel Klett, Prof. Ho-Jin Son, Pink "Ashlee" Howarth, Aaron "Firsty" Peters, John Young "Zhanyong" Li, and Joe "Minnejota" Mondloch have all also been influential in my life and in my time here.. Pravas Deria made a dye for me, which was nice of him. Nick Jackson is also deserving of special mention as he did some theory for me that was used in this thesis.

And, as always, an anti-acknowledgement to Benjamin M. Klahr, whose subversive efforts and general subterfuge have hindered me every step of the way.

List of Abbreviations

ALD	Atomic Layer Deposition
CV	Cyclic Voltammetry/Cyclic Voltammogram
EIS	Electrochemical Impedance Spectroscopy
FTO	Fluorine-Doped Tin Oxide
LSV	Linear Sweep Voltammetry
Ppm	Parts Per Million
TTIP	Titanium(IV) Isopropoxide
XPS	X-ray Photoelectron Spectroscopy
DSC(s)	Dye-Sensitized Solar Cell(S)
CB	Conduction Band
VB	Valence Band
ET	Electron Transfer
EPR	Electron Paramagnetic Resonance
ACN	Acetonitrile
OCVD	Open Circuit Voltage Decay
UV-Vis	Ultraviolet-Visible
IO	Inverse Opal
PCE	Photo Conversion Efficiency
IPCE	Incident Photon-to-Electron Conversion Efficiency
CPE	Constant Phase Element
SCL	Space-charge Layer

OPV	Organic Photovoltaic
FF	Fill Factor
SEM	Scanning Electron Microscopy
SEM/EDS	Scanning Electron Microscopy/Energy-dispersive X-ray Specstrocopy
J-V	Current density-Voltage
PV	Photovoltaic
QCM	Quartz Crystal Microbalance
THF	Tetrahydrofuran
ALD-PT	Atomic Layer Deposition Post-Treatment
$TBAPF_6$	Tetrabutylammonium Hexafluorophosphate
WE	Working Electrode
LUMO	Lowest Unoccupied Molecular Orbital
HOMO	Highest Occupied Molecular Orbital
Ca.	Circa (Latin version)
DFT	Density Functional Theory

Table of Contents

List of Figures

List of Tables

Chapter 1. Introduction to the Energy Problem and Dye-Sensitized Solar Cells

1.1. Climate Change and the Energy Problem

Mitigating anthropomorphic climate change due to greenhouse gas emission while simultaneously meeting dramatically increasing global energy demands is the largest challenge facing humanity today. The United States Energy Information Association (EIA), a statistical and analytical agency within the U.S. Department of Energy, projects that world energy consumption will grow approximately 48% from 2012 levels by 2040.[1] As shown in Figure 1.1 a majority of this energy will be derived from fossil fuel (*i.e.*, coal, petroleum, or natural gas) combustion.

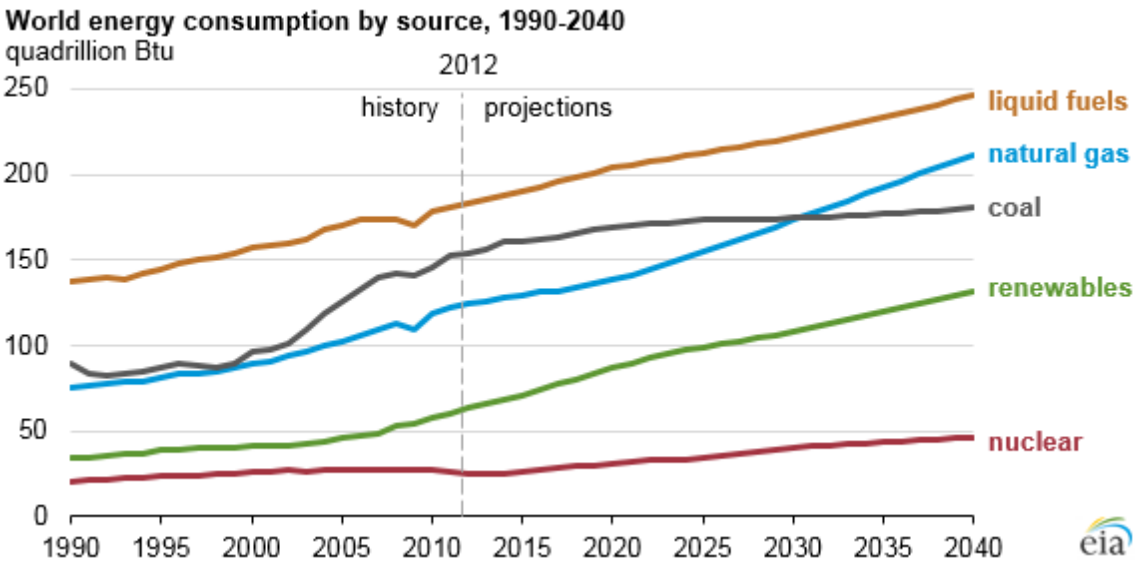

Figure 1.1. World Energy Consumption by Source, 1990-2040.
The projected worldwide energy consumption by type of energy source through the year 2040. Projections are made by the U.S Energy Information Administration and contained in the International Energy Outlook 2016, which was released May 11, 2016 (see reference 1).

Though improvements in hydraulic fracturing (often referred to as "fracking") and discovery of new fossil fuel reservoirs have eased concerns about fossil fuel scarcity, combustion of these fuels results in the formation of carbon dioxide (CO_2) and other greenhouse gases.

Anthropogenic CO_2 has already contributed to the highest atmospheric concentration of CO_2 in human history, and increasing combustion of fossil fuels to meet increased energy demands would only compound the problem.

The Intergovernmental Panel on Climate Change (IPCC), an international organization established by the United Nations Environment Program to analyze data produced world-wide relating to climate change, emphasized in its 2014 Fifth Assessment Report on climate change mitigation that, even if century-long CO_2 atmospheric concentration goals are met, peak concentrations must also be limited to avoid significant temperature changes.[2] The report finds that, in order to have >50% probability of limiting global temperature change to 1.5 °C relative to pre-industrial levels, CO_2 concentrations in 2100 must be below 430 ppm. Note that, after the United Nations Climate Change Conference in Paris, temperature changes less than 1.5 °C are considered necessary to avoid catastrophic coastal flooding for numerous island nations.[3] CO_2 concentrations near 500 ppm in 2100 are more likely than not to prevent temperature changes of more than 2 °C relative to pre-industrial levels. However, if concentrations spike to ~530 ppm, even temporarily, temperature increases exceeding 2 °C become just as likely. [2] With CO_2 concentrations already exceeding 400 ppm and rising, meeting these benchmarks will be exceptionally difficult. In fact, in some model systems, any scenario in which 530 ppm atmospheric CO_2 concentrations are possible involves ~0 global net emission of carbon into the atmosphere, see Figure 1.2.[4]

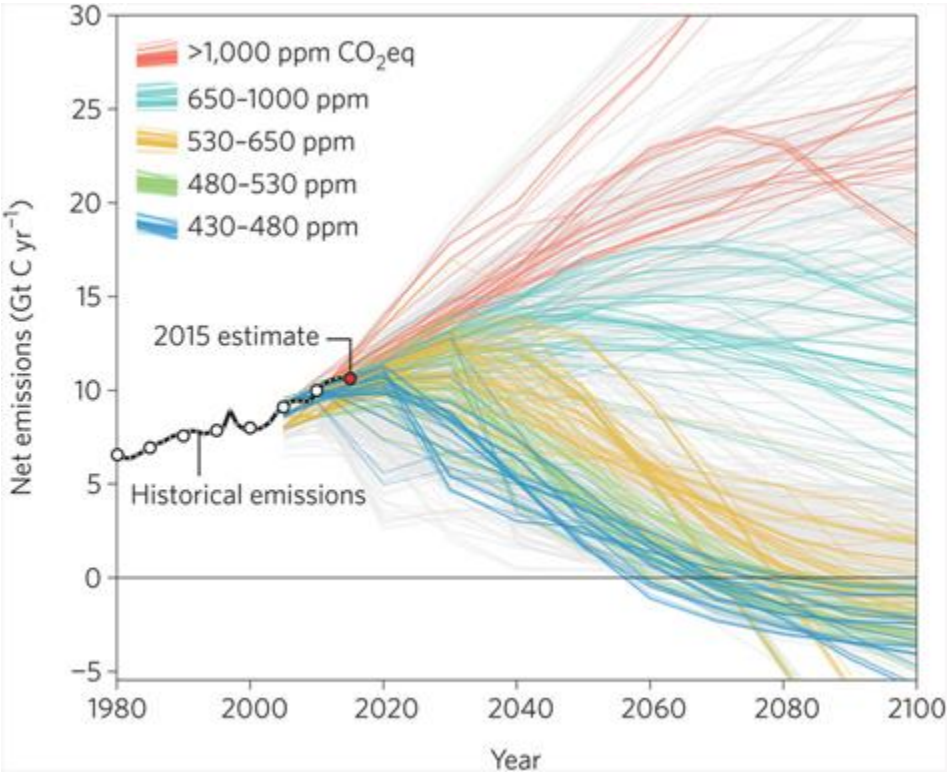

Figure 1.2. Projected Atmospheric CO_2 Concentrations by Year Based on Net Emissions. Projected atmospheric CO_2 concentrations are in parts per million and grouped by color into emission scenarios representing specific atmospheric CO_2 concentration ranges. Note that, in this projection, net emissions must approach 0 in order to avoid >500 ppm atmospheric CO_2 concentrations in 2100. Reprinted with permission from Smith, P., et al. Biophysical and Economic Limits to Negative CO_2 Emissions. *Nature Clim. Change* **2016,** *6*, 42-50. Copyright 2015, Macmillan Publishers Limited.

The energy supply sector is the largest contributor to anthropogenic greenhouse gas emissions; therefore, any projected future scenario that sees CO_2 concentrations remain below even 500 ppm involves a near quadrupling of the energy supply share of zero and low carbon energy production.[2]

Renewable energy technologies, such as wind or solar, are some of the most obvious ways in which carbon-free energy can be generated. However, solar far outstrips wind in theoretical power potential.[5] In fact, photovoltaic cells with 15% efficiency could generate a theoretical ~2500 TW of energy per year, over 150 times that of wind power and over 80 times the

anticipated global energy requirements in 2050. This theoretical output is not obtainable given covering the entirety of available land area with solar cells is impractical,[citation needed] but the point remains that the sun is capable of meeting the planet's energy needs if its energy can be adequately harvested.

One device capable of harvesting the sun's energy is the dye-sensitized solar cell (DSC). DSCs first found success with O'Regan and Grätzel in 1991, the major breakthrough being utilization of high area TiO_2 nanoparticulate films as the photoelectrode.[6] Though power conversion efficiencies (PCE) remained nearly stagnant at ~ 11% for much of the 1990s and 2000s, detailed studies across the two decades led to a more thorough understanding of the various processes of DSC operation. This increased understanding of function finally allowed DSCs to break through this artificial efficiency ceiling, with current PCEs crossing 13%. While DSCs have recently declined in popularity as an alternative photovoltaic device due to the emergence of perovskite solar cells, the basic architecture of dye sensitization is still utilized in various solar energy/fuels applications.[7-12] Thus, understanding and advancing the underlying science of DSCs is still of value to the photovoltaic community at large. The following sections will describe how DSCs function, where and how they can be improved, and the techniques utilized in this dissertation to accomplish these goals.

1.2. Introduction to Dye-sensitized Solar Cells

1.2.1. Components of Dye-sensitized Solar Cells

DSCs utilize four main components: a semiconductor electrode, a dye, an electron shuttle, and a counter electrode (sometimes referred to as the dark electrode). Generally, these four

components are brought together using a transparent conducting oxide (TCO), usually either fluorine-doped tin oxide (FTO) or tin-doped indium oxide (ITO), see Figure 1.3.

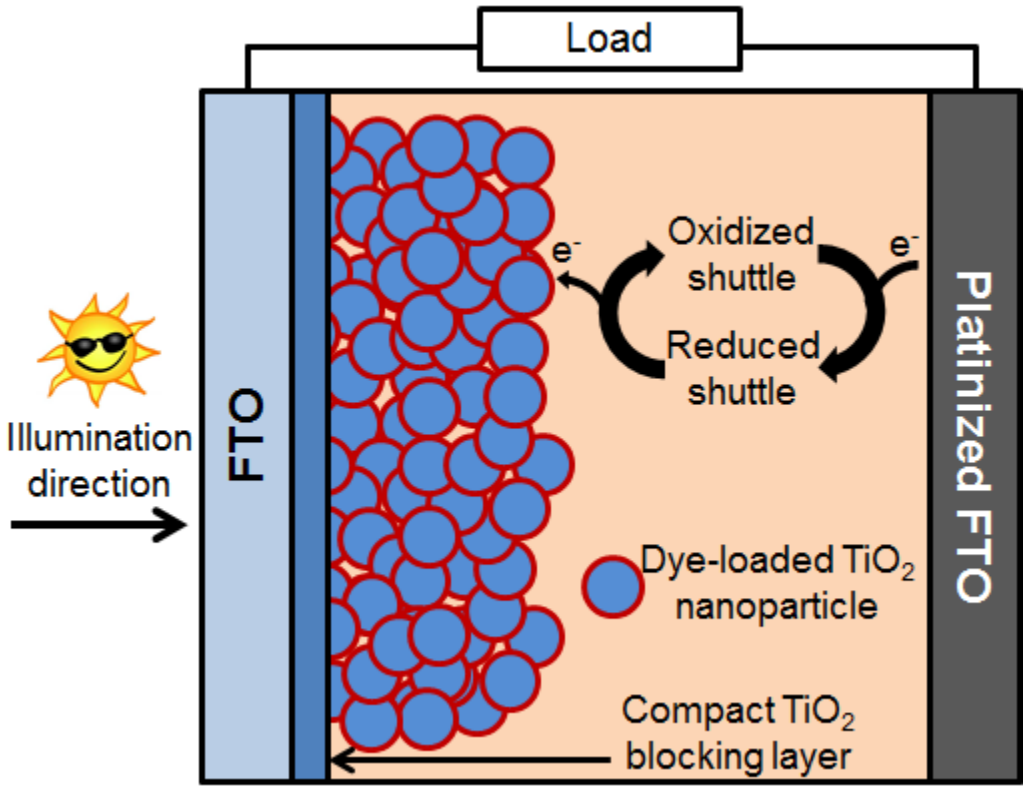

Figure 1.3. Pictorial Representation of a Typical DSC and Components.
The DSC depicted is not to scale. As FTO is the only TCO used in this dissertation, it has been included in place of the more generic TCO.

As shown in Figure 1.3, the most commonly used semiconductor for DSCs is TiO_2. Nanoparticulate TiO_2 is used to increase the available surface area for dye adsorption, which dramatically increases the amount of dye adsorbed and thus the light harvesting. The dye is adsorbed through some form of anchoring group, with carboxylic acid being the most common. Both inorganic ruthenium-based dyes[13, 14] and organic porphyrin[15, 16] or thiophene[17-19] based dyes have been used with success in DSCs. A compact TiO_2 blocking layer coats the FTO (in this dissertation, only FTO is used as the TCO), preventing contact between the FTO and the redox

shuttle in solution.[20, 21] Initial successful iterations of DSCs used exclusively the complex, two-electron triiodide/iodide (I_3^-/I^-) redox couple as the electron shuttle.[22] More recently, iodide-based shuttles have been replaced by simpler, one-electron outer-sphere redox shuttles based on trisbipyridylcobalt(III/II) ($Co(bpy)_3^{3+/2+}$) and its derivatives. In theory, any reversible redox couple with an appropriate redox potential is capable of serving as an electron shuttle, but not all redox couples will be efficient electron shuttles for DSCs. What makes a particular redox couple a well performing electron shuttle will be discussed in more detail both later in this introduction and in Chapter 2 of this dissertation. Finally, a counter electrode is fabricated via coating a TCO with a (typically) platinum catalyst, though gold,[23, 24] carbon,[25, 26] and certain polymers[27, 28] have been used with success as well.

1.2.2. Operating Processes in Dye-sensitized Solar Cells

The DSC components described briefly in Section 1.2.1 work together to perform the core function of DSCs, namely to extract potential energy from the sun via collection of photon-induced excited electrons from a dye. An overview of this process is given in Figure 1.4, with the various possible pathways of electron travel designated by arrows labeled with their rate constants k_n, where n denotes the assigned process number.

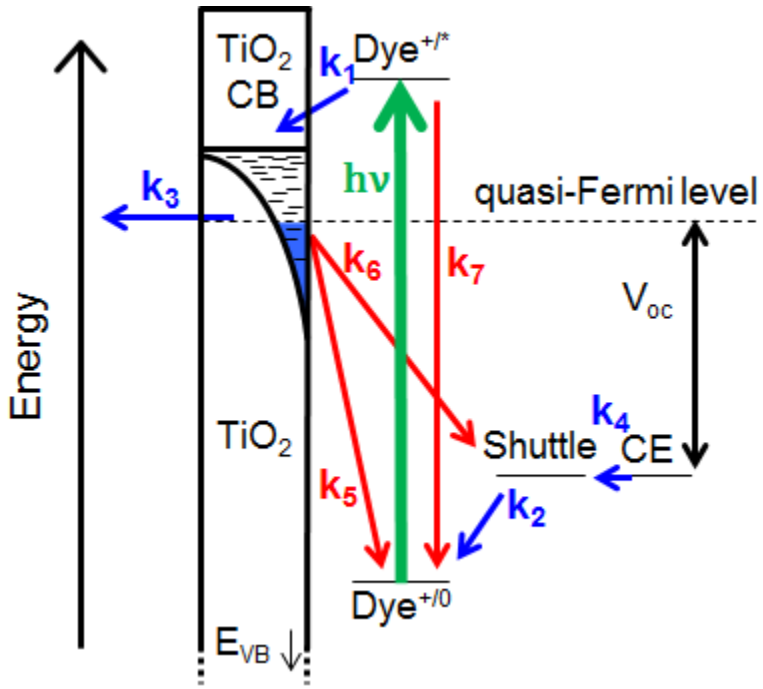

Figure 1.4. Schematic Representation of the Electron Transfer Processes in a DSC.
The processes and associated rate constants that can occur in DSCs are labeled k_n, with n being the process number and k representing the associated rate constant. Processes 1-4 are necessary, beneficial processes, processes 5-7 are parasitic, deleterious processes, and hν is light absorption. These processes are denoted by arrows, which also approximate the possible paths of electrons in DSCs. 1) charge injection; 2) dye regeneration by the redox shuttle; 3) charge collection at FTO; 4) redox shuttle regeneration at the counter electrode (CE); 5) recombination between electrons in the TiO_2 conduction band (CB) and the oxidized dye; 6) interception of CB electrons by the oxidized form of the redox shuttle; 7) relaxation of the excited electron on the dye to the ground state. The curved line below the CB represents the exponential distribution of sub-band gap trap states in the TiO_2 and their partial filling up to the quasi-Fermi level when the device is operating. The open-circuit voltage (V_{oc}) is the potential difference between the quasi-Fermi level and the CE.

While Figure 1.4 does not explicitly show the external load (as is seen in Figure 1.3) that completes the circuit, all relevant processes in a functioning DSC are shown. These processes all have associated rate constants for the transfer of an electron (depicted in Figure 1.4 as k_n, where n is the process number) that determine how quickly a given process occurs. Processes 1-4 are beneficial processes, while processes 5-7 are considered parasitic. In any operating DSC, light absorption by the dye adsorbed on TiO_2, promoting an electron to an excited state, must necessarily occur before any of the operational processes can take place. This is followed by

charge injection (process 1). Charge injection results in an oxidized dye that must be reduced before additional light absorption and charge injection can occur. This is accomplished by the reduced form of the redox couple, which serves as an electron shuttle, via process 2: dye regeneration. The newly generated oxidized form of the redox shuttle then begins diffusing toward the counter electrode to be reduced. Meanwhile, the injected electron in TiO_2 diffuses toward the underlying FTO for process 3, charge collection. Once charge collection occurs, the electron leaves the DSC through the external circuit, expunging its excess potential energy in the form of work and returning to the DSC at the counter electrode. Once at the counter electrode, the electron reduces the redox shuttle during process 4, allowing the shuttle to continue regenerating the dye and completing the circuit.

Processes 5-7 in Figure 1.4 are considered parasitic processes and are deleterious to the performance of the DSC. These three processes, which are referred to as recombination, interception, and relaxation, respectively, can limit the extractable photocurrent and/or voltage in an operating DSC. Recombination (Figure 1.4 process 5) is an electron in the TiO_2 CB reducing an oxidized dye on the TiO_2 surface (as opposed to being collected at the TCO); interception (Figure 1.4 process 6) is similar, except the oxidized half of the redox shuttle is reduced instead. Finally, excited state relaxation (Figure 1.4 process 7) is a result of the dye excited state decaying to its ground state before injection can take place.

1.2.3. Competitive Processes and DSC Performance: Extractable Photocurrent

The relative rates/rate constants of the aforementioned processes (k_n) determine the extractable photocurrent in DSCs. The theoretical maximum extractable photocurrent is dependent on the light harvesting efficiency of the device, which in turn is dependent on the

properties of the dye utilized (such as size, extinction coefficient, and visible light absorption) and the thickness the TiO_2 nanoparticulate layer, which determines the actual number of dye molecules available for light absorption. The actual photocurrent extracted from a device, however, depends on charge injection (k_1) and charge collection (k_3). Charge injection is a prerequisite for charge collection and therefore charge injection efficiency determines the maximum possible charge collected. The efficiency of charge injection is in turn determined by the relative location of the dye excited state to the TiO_2 conduction band (CB) and also the electronic coupling between the dye and TiO_2. If the dye excited state is too low in energy, injection will be inefficient, leading to increased relaxation (process 7). The same is true if the electronic coupling between the molecular orbitals on which the dye excited state is localized and the TiO_2 CB is weak. Generally, this relaxation process is avoided via judicious engineering of the dye or selection of dyes with appropriate excited state energies that allow for efficient charge injection. Injection efficiency can all so be affected by coating of the TiO_2 nanoparticulate layer with an insulating metal oxide such as Al_2O_3 (a technique that slows charge interception processes and will be discussed in detail later). In these cases, the resultant energetic barrier to injection reduces injection efficiency (thus increasing losses to relaxation) despite the otherwise suitable properties of the dye.[29-31]

The efficiency of charge collection is defined by the percentage of injected electrons that are actually collected at the FTO. The injected electrons in the TiO_2 CB move toward the FTO via a diffusion like process controlled primarily by thermal excitation from sub-CB trap states, and this diffusion constant is light intensity and TiO_2 morphology dependent.[32, 33] The “random walk” nature of this diffusion gives arise to a property known as “collection length”, denoted

here as *L*, which is the film thickness over which injected electrons can be collected. Because diffusion takes place at a constant rate for a given film morphology/light intensity, the magnitude of *L* will be primarily dependent on the rates of recombination (k_5) and interception (k_6), which compete with the rate of diffusion/collection (k_3). If *L* is on par with or thicker than the TiO_2 nanoparticle film, collection will be efficient.[16, 17] Note that, because charge injection must necessarily take place before charge collection can occur, the deleterious excited state relaxation process does not directly affect charge collection.

As noted above, *L*, and thus charge collection efficiency for a given device, is dependent on the relative rates of recombination and interception. In addition to competing with the rate of diffusion, the rate of recombination in DSCs is also in direct competition with the rate of dye regeneration by the redox shuttle (k_2). If the rate of regeneration by the redox shuttle is suitably fast, whether due to a fast rate constant, a large driving force, or a high concentration of the appropriate reducing species, recombination between electrons in TiO_2 and the dye should be mostly negligible and thus should not significantly affect the collection length. The simplest way to ensure regeneration is fast involves utilizing a redox shuttle with sufficient driving force (*i.e.*, potential difference between the redox potential and the dye ground state) for dye regeneration, Figure 1.5.[34, 35]

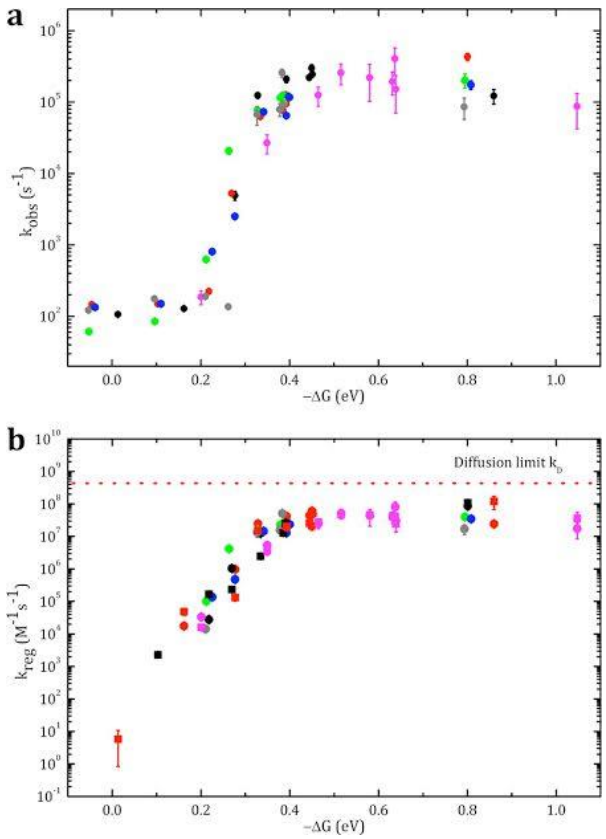

Figure 1.5. Effect of Driving Force on Rate of Dye Regeneration by Redox Shuttle
The observed rate constant of regeneration (a) of a series of carbazole-based dyes with ferrocene derivatives possessing various driving forces for regeneration and (b) the calculated rate constant for regeneration using the data in (a). Reprinted (adapted) with permission from Daeneke, T.; Mozer, A. J.; Uemura, Y.; Makuta, S.; Fekete, M.; Tachibana, Y.; Koumura, N.; Bach, U.; Spiccia, L. Dye Regeneration Kinetics in Dye-Sensitized Solar Cells. *J. Am. Chem. Soc.* **2012,** *134*, 16925-16928. DOI: 10.1021/ja3054578. Copyright © 2012 American Chemical Society.

As evident in Figure 1.5, insufficient driving force slows dye regeneration to the point where the rate for recombination becomes competitive, leading to increased recombination and thus decreased charge collection. In an ideal case, the dye could be efficiently regenerated with minimum driving force so as to limit the loss in device potential associated with high driving force regeneration (see Section 1.2.4). However, due to the numerous competing rates in DSCs, even near-barrierless (*i.e.* no inherent resistance to oxidation/reduction for the redox couple)

shuttles such as the ferrocene derivatives in Figure 1.5 still require ~200-250 mV driving force for regeneration to be competitive with the deleterious processes.

The other process affecting collection efficiency, charge interception, is perhaps the most deleterious process in DSCs, and understanding and/or controlling this process is the focus of a majority of this dissertation. This process affects *L* via interception of a TiO_2 CB electron by the oxidized half of the redox shuttle (k_7) before the electron can diffuse to the FTO. The rate of this process is dependent both on the inherent rate of redox self-exchange for the redox couple and also the driving force (in this case the potential difference between the TiO_2 CB electron and the redox potential of the shuttle) for electron transfer to the shuttle. If this rate is sufficiently fast relative to the rate of electron collection, the interception process will limit charge collection efficiency and thus overall photocurrent.

1.2.4. Competitive Processes and DSC Performance: Extractable Voltage

Section 1.2.3 discussed how photocurrent is affected by the relative rates of the various processes in DSCs, but these processes also affect the extractable voltage in a device. The maximum extractable voltage in a DSC is defined by the potential difference between the TiO_2 CB and the redox potential of the electron shuttle. The actual extracted voltage depends on the difference between the quasi-Fermi level in the TiO_2 and the redox potential of the shuttle (see Figure 1.4). In *n*-type semiconductors such as TiO_2, the Fermi level is located nearer to the CB than to the valence band, and is defined as the potential at which the probability of an electron occupying a state at that potential is exactly 50%. The quasi-Fermi level is analogous to the Fermi level except the semiconductor is displaced from equilibrium, whether by an applied potential, illumination, or, as in the case of DSCs, both. Thus, in theory one should be able to

increase the obtainable voltage of a DSC by switching to a redox shuttle with a lower redox potential. Unfortunately, improving voltage is not that simple, both because of the necessary driving force for dye regeneration described in Section 1.2.3 (and shown in Figure 1.5) and the processes that will be outlined further in this section.

It is useful at this point to introduce the term dark current. While a more complete discussion of dark current's effect on DSC performance takes place in the following Section 1.2.5, it will suffice for now to define dark current as a collective term for electrons flowing in the opposite direction of what is desirable in an operating DSC. It therefore consists mostly of electrons lost from the TiO_2 CB to the redox shuttle via interception. As more electrons are lost to interception, the magnitude of the dark current increases. Dark current, being current that flows in the opposite direction, is opposite in sign to the current resulting from electron collection at FTO and therefore subtracts from the extractable photocurrent. Recall that the rate of interception is dependent on the driving force for electron transfer, which in turn is dependent on the potential difference between the electron and the shuttle redox potential. The quasi-Fermi level potential is the approximate potential of the electron in the TiO_2 and is responsible for the driving force for interception. Thus, as the quasi-Fermi level increases, so does the driving force for interception. If the redox shuttle undergoes fast self-exchange (*i.e.*, the intrinsic rate at which the reduced form of the shuttle transfers an electron to the oxidized form), a smaller driving force threshold will be necessary for interception. The larger the necessary driving force for interception, the higher the potential the TiO_2 quasi-Fermi level can reach before interception becomes so rapid as to outpace charge collection. As mentioned, the larger the maximum potential difference between the quasi-Fermi level and the redox potential of the shuttle that still allows for net positive electron

collection, the larger the extractable voltage will be. Thus, ideal DSC redox shuttles will be resistive to reduction, requiring a large driving force or a catalyst, such as platinum, a common dark electrode material, to be reduced. Note that, because of the numerous competitive rates in DSCs, this resistivity must be asymmetrical; namely, if the shuttle is also resistive to oxidation, dye regeneration will become inefficient and thus recombination, as opposed to interception, will become a primary limiting factor in DSC performance.

1.2.5. Current-Voltage Curves and Power Conversion Efficiency

Having established how the electron transfer processes depicted in Figure 1.4 affect performance in DSCs, the DSC "figure of merit" for determining power conversion efficiency (PCE), photocurrent density-voltage curves (J-V curves), can finally be described. J-V curves are obtained by measuring the current extracted from a DSC under constant illumination as the potential is linearly swept to increasingly higher energy. An annotated example J-V curve is shown in Figure 1.6, and the information extracted from these curves, namely the short-circuit photocurrent density (J_{sc}), the open-circuit voltage (V_{oc}) and the fill factor (FF), are used to calculate PCE via Equation 1.1.

$$\eta = \frac{J_{sc} \times V_{oc} \times FF}{P_{in}} \qquad (1.1)$$

where P_{in} is the incident power illuminating the device. If J_{sc} is in units of milliamps and V_{oc} is in volts, then Equation 1.2 can be divided by 100% to give η as a percentage. For example, a device with 20 mA/cm^2 J_{sc}, 1 volt V_{oc}, and a FF of 0.75 results in a PCE of 20%.

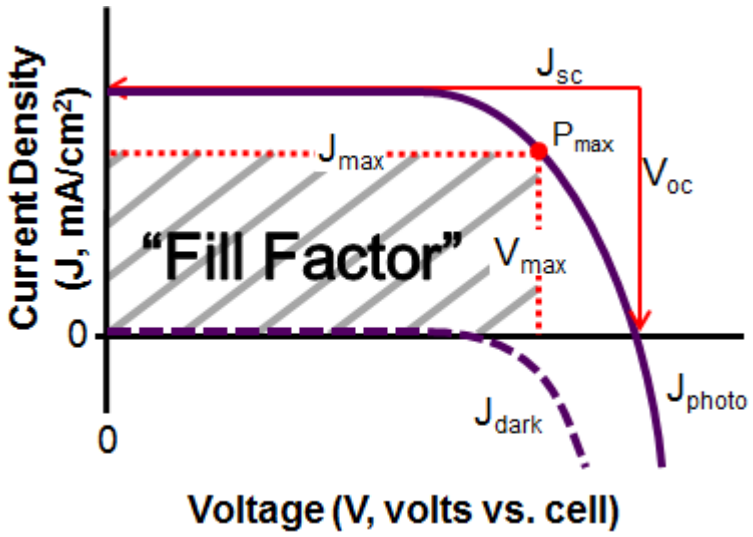

Figure 1.6. Schematic Representation of (Photo)current Density-Voltage (J-V) Curve
The DSC "figure of merit" is the J-V curve. Parameters shown in this schematic representation include the short-circuit current density (J_{sc}), the open circuit voltage (V_{oc}) and a pictorial representation of the concept of "Fill Factor"/the maximum power point (P_{max}). Also shown is dark current. See main text for full discussion of all parameters.

Figure 1.6 depicts the three primary values in solar cell PCE calculation, J_{sc}, V_{oc}, and FF. J_{sc} is defined by the magnitude of current density (typically reported in milliamps per square centimeter) when the device voltage is equal to 0. For DSCs, we consider current flowing through the device in the desired direction (*i.e.*, electrons that are collected at the FTO) to be positive in sign while any current flowing in the opposite direction (*i.e.*, electrons intercepted by the redox shuttle) is negative in sign. As alluded to in Section 1.2.4, this opposite direction current is referred to as dark current, or J_{dark}, owing to the fact it will flow without illumination once a particular potential threshold is reached. At any given potential, the measured current J is defined by Equation 1.2:

$$J = J'_{theo}\eta_{inj} + J_{dark} \qquad (1.2)$$

where J'_{theo} is the theoretically possible current based on the light absorption of the dye and η_{inj} is the injection efficiency. Together, these terms represent the maximum possible current available for collection at the FTO. Note that J_{dark}, which is determined by Equation 1.3, will be opposite in sign to J based on the sign conventions for current outline above.

$$J_{dark} = J_{in} + J_{rec} \tag{1.3}$$

J_{in} and J_{rec} represent the interception current and the recombination current, respectively. When J is equal to 0, meaning the net current flow is 0, $J'_{theo}\eta_{inj}$ is equal to $-J_{dark}$, meaning current is flowing as fast forward as it is backward. The voltage at which this is true is known as the open circuit voltage, V_{oc}. As denoted in Figure 1.4, V_{oc} is also defined as the potential difference between the quasi-Fermi level in TiO_2 and the redox potential of the electron shuttle. Because J_{dark} is determined by J_{in} and J_{rec} which in turn depend on the rate of the interception and recombination processes, respectively, slowing either process (but especially interception) should lead to an increase in V_{oc}, all else being equal.

The final term in Equation 1.1 that is derived from the J-V curve is the fill factor, FF. Fill factor is a measure of the squareness of the J-V curve, and is calculated by taking the maximum value of the product of J and V divided by the product of J_{sc} and V_{oc} for all values of J and V, as shown in Equation 1.4.

$$FF = \max\left(\frac{J \times V}{J_{sc} \times V_{oc}}\right) \tag{1.4}$$

In this way, J_{max} and V_{max} are also determined, being the current density and voltage whose product results in the maximum value when divided by the product of J_{sc} and V_{oc}. Where J_{max}

and V_{max} fall on the J-V curve is known as the maximum power point (hence the subscript "max"), which is the photocurrent density and voltage at which a DSC will operate most efficiently. Thus, J_{sc} and V_{oc} set the maximum possible photocurrent and voltage, and fill factor adjusts for how much of this current and voltage can actually be extracted in a working device. As will be discussed in greater detail in Chapter 3, poor FF is often the result of undesirable resistances somewhere in the DSC circuit. Two types of resistances affect FF: series resistance and shunt resistance. Series resistance is resistance to electron flow in desired directions and should be minimized; shunt resistance is the resistance to electron flow through undesirable pathways, such as directly between FTO and the dark electrode, and must therefore be as large as possible. Examples of the effect of these resistances on J-V curves are shown in Figure 1.7.[36]

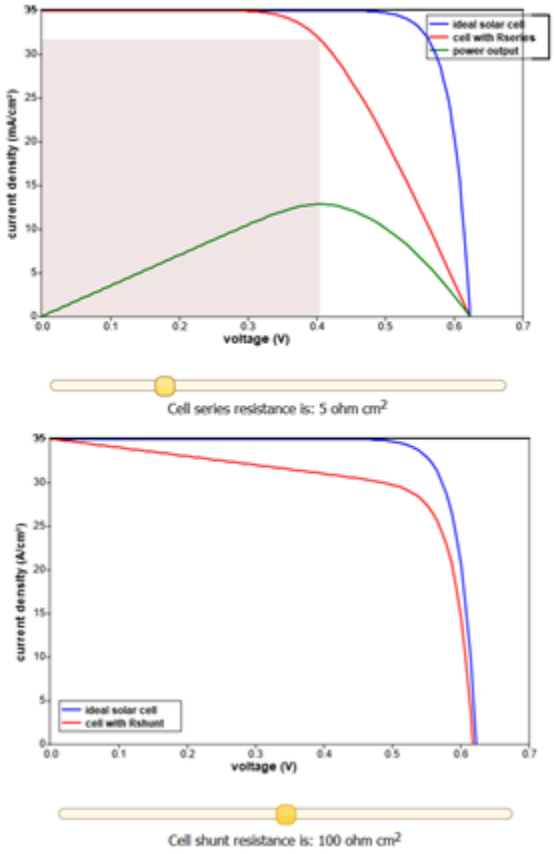

Figure 1.7. Example of the Effect of Series and Shunt Resistances on J-V Curve Fill Factor
The effect of series resistance (top) and shunt resistance (bottom) on the fill factor of a J-V curve for a Si-based photovoltaic. In both graphs, the blue J-V curve represents an ideal device and the red J-V curve represents a device suffering from the specified resistance. The magnitude of the resistance is depicted below the appropriate graph, being 5 ohm cm^2 for series resistance and 100 ohm cm^2 for shunt resistance. Also shown in the top graph is the fill factor of the red J-V curve, demonstrating the deleterious effects of the series resistance. Images screen shot from pveducation.org.

Note that even 5 ohm cm^2 of series resistance can dramatically decrease FF, while 100 ohm cm^2 shunt resistance is not enough to prevent FF decrease. Often, these resistances are simply the result of poor device craftsmanship, but some molecular shuttles have been known to demonstrate poor fill factor with particular dark electrodes due to over-large series resistances (see Chapter 3 of this dissertation, elsewhere[23, 37]). Regardless of the origin, the equal weight

given to FF in Equation 1.1 and the example J-V curves in Figure 1.7 clearly demonstrate the importance of this term to overall device efficiency.

At this time, it should be noted that no DSC devices in this dissertation approach state of the art PCEs, which have been pushed above 13%. In fact, the best PCE you will see in this dissertation is somewhere in the neighborhood of 1.5%. Often, PCE is not calculated for DSCs shown and instead only the relevant J_{sc} or V_{oc} are discussed and/or compared. This is because record breaking DSC PCEs are not the goal of this research. The goal of the research presented herein is to add to the knowledge of the inner workings of DSCs, examining new strategies and attempting to better understand existing strategies that may be utilized to improve DSCs or any photovoltaic that takes advantage of DSC-type architecture. Thus, with the basic working principles of DSCs established, the discussion in the following sections examines how the competition between the various process rates mediates, and at times hinders, the performance of actual DSC devices. Various strategies for augmenting these rates are discussed, before finally a summary of the strategies used in this dissertation are described.

1.3. The Redox Shuttle as a Efficiency Bottleneck in DSCs

1.3.1. Back Electron Transfer and the Iodide Problem in DSCs

If one were to visit the website of the National Renewable Energy Lab in Golden, Colorado, and navigate to the "Best Research Cell Efficiency" chart, one would notice an oddity among the "Emerging PV" devices.[38] Namely, one type of device, despite having nearly a decade's worth head start, plateaued several years after its inception and has seen little improvement in PCE the last 20 years. This device is the dye-sensitized solar cell. While other "Emerging PV"

devices have enjoyed generally consistent growth, DSCs have remained near the ~11-12% PCE level they reached in the mid-90s. One reason DSCs have failed to enjoy the same kind of continuous growth as the other technologies is the same reason they enjoyed such high PCE at their outset: the triiodide/iodide redox mediator. Triiodide, with its multispecies and slow reduction kinetics, perfectly complements the complicated, competitive, and numerous electron transfer processes (and their associated rates) necessary for DSCs to function (see Section 1.2.2).[39, 40] However, the slow kinetics associated with triiodide reduction and the large overpotential required for dye regeneration by I^- limits the obtainable V_{oc} to around 0.85 V and restricts the utilization of new dyes.[13, 39, 41-44]

Thus, concerted effort was made to find a replacement redox shuttle for I_3^-/I^-. One of the most promising candidates was trisbipyridine cobalt (III/II), or $Co(bpy)_3^{3+/2+}$. It was hypothesized that cobalt's relatively slow self-exchange rate, which is due to a large internal reorganization energy because of the low spin d^6 to high spin d^7 transition when cobalt(III) is reduced, would create a large enough barrier to electron interception to allow efficient DSC operation. Coupled with the more positive (lower in energy) redox potential of $Co(bpy)_3^{3+/2+}$ compared to I_3^-/I^-, $Co(bpy)_3^{3+/2+}$ might be expected to improve the voltage of DSCs without harming the photocurrent.[24, 45, 46] It was quickly apparent that this was not the case. The rate of interception by the oxidized cobalt(III) in solution was too fast, and therefore traditional DSC device designs failed. The triiodide/iodide redox couple, despite its obvious faults, was uniquely suited to give highly efficient DSCs. However, it also capped device efficiency at around 11% (see Figure 1.8), a plateau which had already been reached.[13]

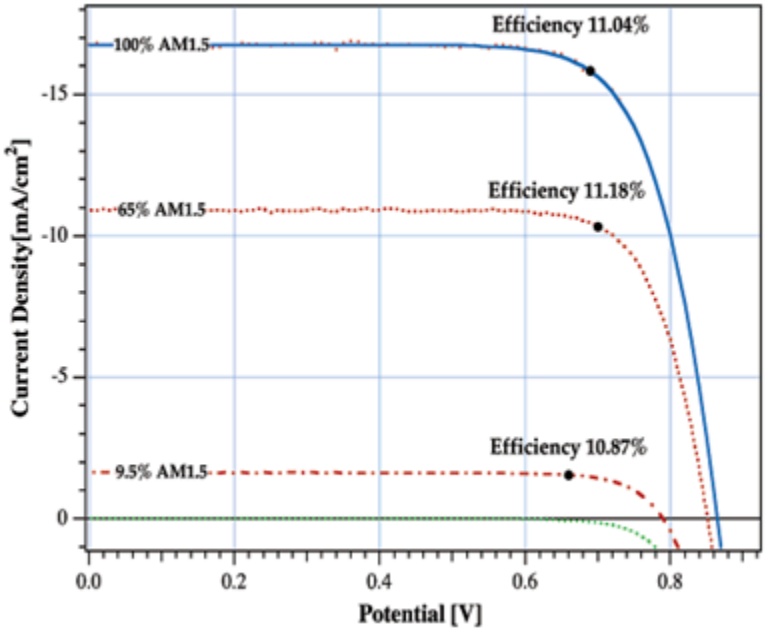

Figure 1.8. J-V Curve for High PCE I_3^-/I^- and Ru-dye DSC.
J-V curve for a one-time record DSC using the I_3^-/I^- redox mediator with the ruthenium based N719 dye. Reprinted (adapted) with permission from Grätzel, M. Solar Energy Conversion by Dye-Sensitized Photovoltaic Cells. *Inorg. Chem.* **2005,** *44*, 6841-6851. DOI: 10.1021/ic0508371, Copyright © 2005 American Chemical Society.

1.3.2. Replacing Iodide and Overcoming Interception with Cobalt-based Shuttles

More recent DSC research focused on understanding how exactly iodide-based devices functioned so well and if this knowledge could be exploited in the service of cobalt redox shuttles. As discussed previously, DSCs are composed of a series of electron transfer processes constantly competing against one another; if the rates of the desired processes are sufficiently fast compared to the rates of the undesired processes, an efficient DSC will result. In DSCs, it is generally easier to slow things down than to speed them up. Therefore, attempts to slow the rate of interception by cobalt shuttles, which would in turn allow cobalt's more desirable properties to shine through, were the primary focus of cobalt studies.

Initially, it was discovered that incorporation of bulky *tert*-butyl groups in the 4,4' positions on the 2,2'-bipyridine in $Co(bpy)_3^{3+/2+}$ created enough of a steric/distance barrier to interception to allow for PCEs approaching ~80% those of the analogous I_3^-/I^- device.[24] Advancing on the strategy of steric/distance barriers to slow interception, dyes with bulky carbon chains as substituents were employed with cobalt-based shuttles.[45] The increased distance between shuttle and TiO_2 electrode again slowed interception so that $Co(bpy)_3^{3+/2+}$ and its derivatives could act as viable shuttles. Despite this improvement, $Co(bpy)_3^{3+/2+}$ devices suffered from a significant drawback: the bulky cobalt shuttles suffered from slow mass transport through the porous TiO_2 nanoparticle network.[47] Taking all of this information together, DSC researchers were able to construct a device exceeding 13% PCE by 1) utilizing the $Co(bpy)_3^{3+/2+}$ redox mediator, 2) incorporating bulky alkyl chains into the dye to increase spatial separation of the shuttle and the underlying nanoparticles, and 3) utilizing a high-extinction coefficient dye with thinner than normal TiO_2 nanoparticle layers, thus limiting both the time available for interception by $Co(bpy)_3^{3+}$ before collection and the detrimental effects of slow mass transport in the mesoporous layer.[48] In fact, the strategy of bulky functional groups on the dye, high extinction coefficient dyes, and thin electrodes is able to slow electron interception to the point that even ferrocene, whose rate of redox self-exchange is nearly barrierless, could be utilized in efficient DSCs.[17, 30] However, these innovations are not without fault. As an example, there will always be a limit to how thin TiO_2 films can be to adequately harvest light, and even the highest efficiency devices using $Co(bpy)_3^{3+/2+}$, a specifically engineered dye, and thin TiO_2 electrodes are still negatively affected by slow mass transport.[48]

1.3.3. Copper-based Redox Shuttles as an Alternative to Cobalt for DSCs

While they are the most successful DSC redox shuttle to date, cobalt-based shuttles are not the only viable alternative redox shuttle. DSCs constructed with copper-based coordination complexes as redox mediators have obtained promising efficiencies approaching 10%.[49, 50] When compared to cobalt polypyridyl shuttles, an attractive feature of copper-based shuttles is their smaller coordination number; the previously described cobalt shuttles are all 6-coordinate species, as would be expected from cobalt's preferred octahedral geometry. Alternatively, copper complexes, especially those employing chelating ligands, are 4- or sometimes 5-coordinate species (the 5th coordination site typically being occupied by a solvent molecule if chelating ligands are employed). Thus, copper-based redox shuttles are generally smaller in physical size compared to cobalt shuttles and are less likely to suffer from slow mass transport.

Copper-based shuttles are also particularly interesting because of both their wide range of accessible redox potentials based on the coordinating ligand identity (differing from cobalt complexes, which are generally limited to redox tuning via substituents on the polypyridyl ligand) and their relatively slow self-exchange kinetics due to large reorganizational energies associated with a change in coordination number/geometry during redox chemistry.[51] The modularity in redox potential inherent to copper complexes (for example, inclusion of two additional methyl groups on a bipyridyl ligand can change the redox potential of the species by nearly 100 mV)[49] reduces some of the constraints on dye design, making it possible to tailor the shuttle to the dye, as opposed to the other way around. Further, the change in coordination number/geometry can potentially be exploited to slow electron interception, improving both charge collection and obtainable voltages.

1.4. Atomic Layer Deposition as a Strategy to Improve DSC Performance

1.4.1. Atomic Layer Deposition

Atomic layer deposition (ALD) is a self-limiting method of growing metals, oxides, or sulfides with sub-nanometer precision (Figure 1.9). In ALD, a metal precursor that can react only with surface sites (often hydroxyls or sulfides) but not itself is introduced to a substrate.

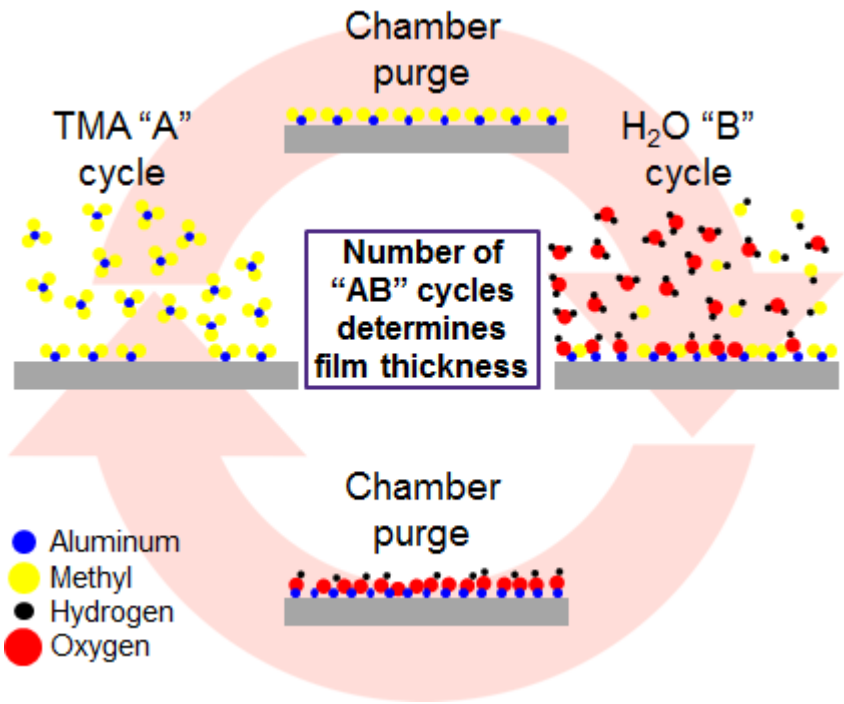

Figure 1.9. Cartoon Representation of ALD process.
A cartoon representation of the trimethylaluminum (TMA) and water ALD process. TMA is introduced to the reaction chamber in the A cycle, where it reacts with the surface. After purging the chamber of excess TMA, water is introduced in the B cycle, reacting with methyl groups still coordinated to aluminum and forming some aluminum oxide surface. This surface can be reacted once again with TMA, restarting the cycle. The number of AB cycles will determine the film thickness.

This metal precursor forms some fraction of a monolayer (depending on the bulkiness of the metal precursor) on the surface but does not deposit beyond that monolayer. Subsequent introduction of an oxygen or sulfur source (or, as sometimes necessary for ALD metal growth, a reductant such as H_2) generates a new layer of reactive surface sites, similar to the initial surface. The introduction of the metal precursor is often referred to as the "A" cycle with the regeneration of surface active sites being the "B" cycle. Thus, repetitive AB cycles will result in the layer by layer growth of the desired metal, oxide, or sulfide, with the thickness of the deposited film being controlled by the number of cycles employed.

1.4.2. ALD of Thin Insulating Layers to Improve DSC Performance

The strategies discussed in Sections 1.3.2 and 1.3.3 are not the only methods for improving DSC performance. One strategy that has also enjoyed success, especially when used in conjunction with outer-sphere transition metal redox shuttles, is ALD of more insulating metal oxides over the underlying TiO_2 nanoparticulate film. Thin layers of Al_2O_3 ALD improved the PCE performance of ferrocene as a redox shuttle due to slowing electron interception,[30] and thin layers of Al_2O_3 also improved the performance of DSCs utilizing N719 dye and I_3^-/I^- redox shuttle when SnO_2 electrodes were used in place of TiO_2.[31] Importantly, this effect is due to actual slowing of the electron interception rate, not simply changing driving forces by moving the CB of the underlying semiconductor.[52, 53] Unfortunately (yet predictably), Al_2O_3 barrier layers beyond certain thicknesses quickly begin to deleteriously affect charge injection. [29-31]

Various other insulating oxides have also been utilized and shown to positively affect the rates of electron interception, especially Nb_2O_5.[54-57] Nb_2O_5 is particularly interesting in that its CB energy is proximal, but higher in energy, to that of TiO_2. This potentially allows for

realization of slowed charge interception from the underlying TiO_2 CB without severely limiting charge injection in the way seen with Al_2O_3 overlayers.

1.4.3. Post-treatment ALD for Suppressing Dye Aggregation and Reducing Charge Interception

One strategy for avoiding the charge injection issues described in Section 1.4.1 is ALD post-treatment (ALD-PT). ALD-PT involves using milder ALD conditions and precursors to deposit metal oxide *around* dyes that are already adsorbed to the TiO_2 (or other semiconductor) surface, thereby blocking only interception and not charge injection. Deposition of SiO_2 around an organic dye, in addition to providing a barrier layer to electron interception, dramatically reduced dye aggregation on the surface, thus improving charge injection efficiency.[58] TiO_2 deposited via ALD was used in a similar fashion, again reducing dye aggregation in a DSC using an organic dye but also improving the wettability of device,[59] and ALD-PT with Al_2O_3 was shown to have a similar effect on aggregation while also slowing interception in DSCs.[60]

ALD-PT has also been shown to enhance the stability of dyes on surfaces, especially under conditions that typically result in dye desorption. The same TiO_2 ALD-PT method mentioned above also resulted in significant stabilization of the organic dye on the TiO_2 surface when the film was soaked in pH ~11 ethanol; without ALD-PT, dye desorption was almost immediately apparent, but TiO_2 ALD-PT stabilized the dye on the surface for months.[59] ALD-PT of Al_2O_3 has been shown to stabilize ruthenium dyes on a surface so that they might be used for heterogeneous catalysis[7] and has also been employed in a dye-sensitized solar fuel device for the production of hydrogen. In the latter case, Al_2O_3 not only reduced aggregation and improved

stability, but also served to spatially separate a catalyst from the dye, limiting the undesirable electron recombination between them.[8]

1.5. DSCs, Redox Shuttles, ALD, and the Studies Presented Herein

The above sections outlined the working principles of DSCs, what their current limitations are, and how the field has approached overcoming said limitations. This dissertation follows in the same vein, attempting to add to the base of knowledge from which winning strategies can be developed to bring efficiency gains to both DSCs and DSC-like devices. As the title suggests, the primary goal of this work is to better understand existing pathways for electron interception and investigate methods for slowing this process. This was approached either by direct interrogation and attempted modulation of electron interception by redox shuttles or by investigation of the physical properties of materials that offer the promise to reduce electron interception in future systems.

This dissertation begins with a new copper-based redox shuttle for DSCs, finding that a mixed sulfur-nitrogen chelating ligand can be coordinatively replaced by Lewis-basic 4-*tert*-butylpyridine (TBP), but only when the copper center is in the 2+ oxidation state; copper(I) re-coordinates the original ligand. This multispecies redox shuttle is characterized, and its effect on the electron transfer processes in DSCs is established. The multispecies shuttle is highly resistant to electron interception, and this results in a promising ~250% increase in obtained photocurrent density. Incidentally, the TBP-coordinated, copper(II) half of the redox shuttle is so resistive to reduction as to require a new counter electrode for efficient reduction of the shuttle. Chapter 3

describes this new counter electrode while also examining the deleterious effect of the charge transfer resistance at traditional DSC counter electrodes.

Chapter 4 presents a slight break in theme as electron interception plays only a cursory role. A porphyrin dye adsorbed on a TiO_2 surface is protected from air and light degradation by Al_2O_3 ALD-PT. The PT process is shown to be observable by in-reactor quartz crystal microbalance (QCM), and ALD-PT is shown capable of preserving the light harvesting properties of the porphyrin dye over 1+ months of exposure to ambient light and air (compared to less than 72 hours without ALD-PT). While ALD-PT has the expected (and previously observed) effect on DSC behavior, the retention of light harvesting capabilities, even under aggressive conditions such as direct LED illumination in an oxygen-rich solution, is promising for use in DSC-like architectures as photocatalytic devices.

In a return to electron interception, Chapter 5 studies the same system as in Chapter 4 (a TiO_2 adsorbed porphyrin dye with Al_2O_3 ALD-PT), but instead studies how electron superexchange from TiO_2 through the surface adsorbed dye influences electron interception by a cobalt-based redox shuttle. Attempts are made to quantify this process by comparing the magnitudes of dark current and the lifetimes of electrons in the TiO_2 conduction band in the presence and absence of surface-adsorbed dye.

Finally, Chapter 6 attempts to determine the location of the conduction band of Nb_2O_5 fabricated specifically by ALD. Comparisons of CB location for this potentially useful blocking layer/TiO_2 replacement material are made with the CB location of TiO_2, also fabricated via ALD. By Mott-Schottky analysis of film capacitances obtained via electrochemical impedance

spectroscopy, the Nb_2O_5 CB is estimated to be 40-60 mV more negative (higher in energy) than that of TiO_2.

Chapter 2. A Multi-species Copper Redox Shuttle for Dye-sensitized Solar Cells*

2.1. Introduction and Background Information

As discussed in the introduction to this dissertation, dye-sensitized solar cells (DSCs) are an established alternative photovoltaic technology. Following O'Regan and Grätzel's 1991 breakthrough, device power conversion efficiencies (PCEs) were quickly pushed above 10%.[6, 14] Over the next two decades, however, relatively little improvement in efficiency was realized, but comprehensive studies of the electron transfer (ET) properties of triiodide/iodide and other shuttles identified key requirements for the success of any redox shuttle.[41, 44, 61, 62] One point made abundantly clear was that large barriers for electron transfer to/from the triiodide/iodide were responsible for the superior performance but also limited future improvement of DSC devices. Triiodide/iodide and its multi-electron/atom oxidation/reduction processes helped to slow undesirable back electron transfer (*i.e.*, interception of injected electrons by triiodide), allowing for record PCEs but resulting in large kinetic overpotentials for dye regeneration.[39, 63] Even with DSCs engineered to yield sizable EQEs (external quantum efficiencies, *i.e.*, incident-photon-to-current conversion efficiencies), this large but necessary overpotential limited the maximum attainable PCE values to around 11%. Thus, to surpass this limit, alternative shuttles would be necessary. This chapter explores one such alternative that is based on a copper coordination complex that exists in two distinct forms depending on the oxidation state of the copper.

Coordination complexes of cobalt,[16, 24, 47, 64] copper,[65, 66] nickel,[67] and iron,[17, 30] as well as organic redox couples[68] and solid-state hole transporting materials[69, 70] have all been previously examined as potential replacements for triiodide/iodide. In most cases, these replacements lacked the asymmetrical redox behavior inherent to triiodide/iodide (*i.e.*, the species engaging in

forward ET is not simply a less highly charged version of the atom or molecule resisting back ET), and failed to improve overall PCEs. More recently, however, DSCs utilizing tris(2,2'-bipyridine)cobalt(III)/(II) ($Co(bpy)_3^{3+/2+}$) and its derivatives as shuttles have achieved PCEs of greater than 13%.[48] The impressive and record setting PCEs are a result of designing dyes, electrodes, and shuttles in such a way that suitably fast dye regeneration can be achieved at overpotentials nearly 200 mV smaller than required with I^-, yet with interception of dye-injected electrons remaining slow enough to ensure large charge-collection yields. In the case of $Co(bpy)_3^{3+/2+}$ shuttles, bulky functional groups on high extinction coefficient dyes (which allow for comparatively thin electrodes) serve to slow electron interception to acceptable rates, permitting other beneficial characteristics of the shuttle (such as spin-engendered amplification of reorganization energies) to manifest themselves, thereby yielding improved cell performance.[16, 48, 64]

The innovations above that allowed $Co(bpy)_3^{3+/2+}$ to succeed as a redox shuttle emphasize slowing electron interception rates by increasing relevant charge-transfer distances, decreasing distances over which charge must be collected, and lessening the photoelectrode's exposed surface area. Taking inspiration from the complicated electron transfer properties of triiodide/iodide, we present an alternative strategy: modifying the electronic and coordination environment of a transition metal ion in a way that introduces asymmetrical rates of electron transfer. In this chapter, we subsequently accomplish this with copper(II/I) species. Copper based redox couples are well known to change coordination geometry as a function of metal oxidation state. Copper(I) complexes generally adopt 4-coordinate tetrahedral geometries while copper(II) complexes typically adopt a 5-coordinatate square pyramidal, 5-coordinate trigonal bipyramidal,

or 6-coordinate octahedral geometry.[51, 71] The fifth (or fifth + sixth) coordination site is typically satisfied by recruiting a solvent molecule. This difference in coordination geometry between the oxidized and reduced forms of the shuttle molecule results in a significant reorganization energy, as evidenced, for example,[51, 71, 72] by considerably slower electron self-exchange rates for Cu(II)/(I) couples relative to similarly sized redox couples lacking substantial inner-sphere bond-length or chemical-composition changes.[72, 73] This behavior has not escaped notice by the DSC research community, and indeed, interesting examples of the use of copper complexes as redox shuttles in dye cells have been reported.[65, 66, 74]

Here, we go a step further by coupling ET not only to a change in coordination geometry, but also to a wholesale change of the composition of the coordination environment. To motivate the change, we take advantage of the preference of Cu(I), but not Cu(II), for highly polarizable ligands—in this instance one featuring sulfur atoms. We employ a pseudo-macrocycle, 1,8-bis(2-pyridyl)-3,6-dithiaoctane (PDTO) as a tetradentate ligand for Cu(I) (Figure 2.1), such that the loss of coordination of sulfur atoms upon oxidation of the metal center facilitates the loss as well of coordination by less highly polarizable nitrogen atoms. The preference of Cu(II) for less highly polarizable ligands is satisfied by 4-*tert*-butylpyridine (TBP) already present at high concentration because of its known ability to favorably influence DSC open-circuit voltages (V_{oc}).[14, 75-77] Thus, in a mixture of Cu(I) and Cu(II), two very different species – $Cu(PDTO)^{+}$ and $Cu(TBP)_{4+x}(ACN)_y^{2+}$ – are formed. Importantly, they are interconvertible based on transfer of a single electron; see Figure 2.1.

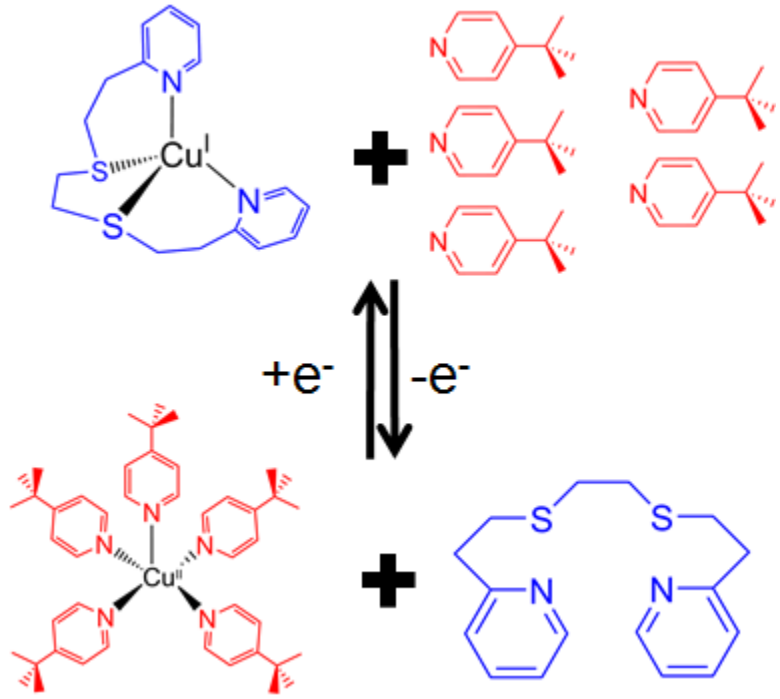

Figure 2.1. Rearrangement of Copper Coordination Sphere Upon Electron Transfer
In the 1+ oxidation state, the copper center is coordinated to the PDTO ligand (blue). Upon oxidation to Cu(II), the copper center sheds the PDTO ligand and instead coordinates 4-6 TBP (red) molecules (5-site coordination shown here for simplicity). This process is shown to be reversible.

These species work in complementary fashion to yield DSCs characterized by good dye regeneration but dramatically decreased rates of back ET. An important consequence is greater power conversion efficiency compared to efficiencies of cells containing shuttles based on only one of the two coordination motifs.

2.2. Experimental Methods and Instrumentation

2.2.1. Reagents

Unless otherwise noted, chemicals were purchased from Sigma Aldrich (St. Louis, MO) and used as received. The reagents used in synthesis and study of redox shuttles include 1,2-dithioethane, 2-vinylpyridine, 4-*tert*-butylpyridine, copper(II) triflate, copper (shot),

tetrakis(acetonitrile)copper(I) tetrafluoroborate, cobalt nitrate, 2,2'-bipyridine, ammonium hexafluorophosphate, tetrabutylammonium hexafluorophosphate, iodine, and 1-butyl-3-methylimidazolium iodide. Hexachloroplatinic acid in isopropanol was used in the preparation of platinum counter electrodes Acetonitrile was the primary experimental solvent, with methanol, hexanes, and dichloromethane employed for syntheses or crystallizations. All solvents were used as received with no special care taken to ensure dryness.

Titanium(IV) isopropoxide (Sigma Aldrich, 99.999% trace metal basis) was used as an ALD precursor to fabricate ALD TiO_2 blocking layers. TiO_2 nanoparticle paste (18NR-T) was purchased from Dyesol (Queanbeyan, NSW, Australia). FTO glass (8 Ohm resistance), was purchased from Hartford Glass (Hartford City, IN).

2.2.2. Synthesis of PDTO Ligand

1,8-bis(2-pyridyl)-3,6-dithiaoctance (PDTO) was synthesized based on the procedure of Goodwin and Lions.[78] Neat 1,2-dithioethane was combined with neat 2-vinylpyridine in a 1:2.1 ratio, covered, and stirred for 1 hour before being allowed to stand overnight. The resulting solid mass was dissolved in a minimum of dichloromethane and PDTO was extracted from residual 2-vinylpyridine and/or any polyvinylpyridine that may have formed during the reaction via sonication with hot hexanes. Upon cooling, PDTO crystallized from hexanes and was confirmed via NMR (not shown). Yield was not calculated.

2.2.3. Synthesis of $Cu(PDTO)^{2+}$, $Co(bpy)^{2+}$, and $Co(bpy)^{3+}$

$Cu(PDTO)(CF_3SO_3)_2$ was generated via addition of $Cu(CF_3SO_3)_2$ to PDTO in methanol (1:1.1 mole ratio) followed by rotary evaporation. $Co(bpy)^{2+}$ was synthesized via addition of 3.1

mole equivalents of 2,2'-bipyridine to a solution of $Co(NO_3)_2$ in methanol. A ten-fold excess of ammonium hexaflurophosphate was subsequently added to metathesize the nitrate salt to the hexafluorophosphate salt, which was precipitated from solution by addition of water, resulting in a [tris-(2,2'-bipyridine)cobalt(II)]hexafluorophosphate salt ($Co(bpy)_3^{2+}$). $Co(bpy)_3^{3+}$ was synthesized via oxidation of $Co(bpy)_3^{2+}$ with excess $NOBF_4$ in acetonitrile. Any remaining $NOBF_4$ was removed by filtration and $Co(bpy)_3^{3+}$ was isolated as a hexafluorophosphate salt by the same method as $Co(bpy)_3^{2+}$.

2.2.4. Dye Synthesis

Carbz-PAHTDTT was the dye used for all solar cells. The full name of Carbz-PAHDTT is 3-(5-{6-[5-(2-{4-[Bis-(4-carbazol-9-yl-phenyl)-amino]-phenyl}-vinyl)-3-hexyl-thien-2-yl]-dithieno[3,2-b;2',3'-d] thiophen -2-yl}-4-hexyl-thien-2-yl)-2-cyano-acrylic acid. This dye was synthesized for me by someone with far more skill than I named Prof. Pravas Deria according to literature procedure.[17] The dye structure is shown in Figure 2.2.

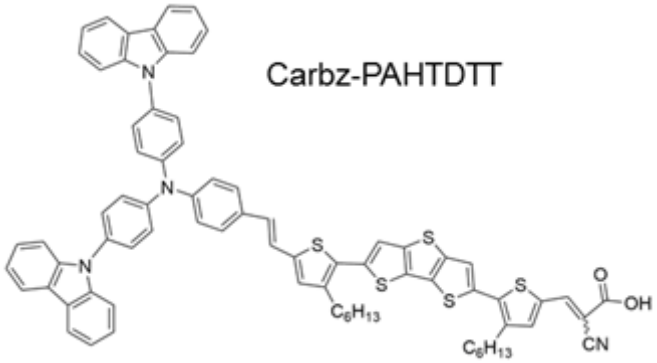

Figure 2.2. Carbz-PAHTDTT Dye.
Structure of 3-(5-{6-[5-(2-{4-[Bis-(4-carbazol-9-yl-phenyl)-amino]-phenyl}-vinyl)-3-hexyl-thien-2-yl]-dithieno[3,2-b;2',3'-d] thiophen -2-yl}-4-hexyl-thien-2-yl)-2-cyano-acrylic acid, referred to in the text as Carbz-PAHTDTT.

2.2.5. Electron Paramagnetic Resonance Spectroscopy

X-band (~9.32 GHz) continuous wave electron paramagnetic resonance (EPR) spectra were collected by George E. Cutsail III on a modified Varian E-4 with 100 kHz field modulation at room temperature or 77 K with a finger liquid nitrogen dewar. Note all frozen solution samples for EPR spectroscopy were in ethanol solvent. Simulations of EPR spectra were performed using the MATLAB EasySpin v4.5 toolbox (easyspin.org).[79]

2.2.6. X-Ray Crystallography

Slow evaporation of a dichloromethane solution containing nominally $Cu(PDTO)^{2+}$ and TBP at 1:10 Cu:TBP ratio yielded purple, x-ray quality single crystals. Single crystal diffraction data was collected on a Bruker Kappa Appex MoKα Triumph edition X-ray instrument.

2.2.7. UV-Vis Spectroscopy

UV-Vis experiments were performed on a Cary-5000 UV-Vis-NIR spectrophotometer. Tetrakis(acetonitrile)copper(I) tetrafluoroborate was the Cu(I) source and copper(II) triflate was the Cu(II) source for all UV-Vis TBP or PDTO titrations. Quartz cuvettes with pathlength of 1 cm were used for all UV-Vis experiments. The concentration of analyte varied depending on the absorbance feature being interrogated.

2.2.8. Electrochemical/Photoelectrochemical Setup

Cyclic voltammetry was performed with a CHI900 potentiostat by using a platinum disk as a working electrode, platinum mesh as a counter electrode, and KCl saturated silver/silver chloride as a reference electrode. The scan rate was 0.05 V/s. All other electrochemistry measurements (including 2-electrode photocurrent/voltage measurements) were performed using a Solartron

Analytical Modulab with a 1 MS/s potentiostat. Three-electrode dark current and open-circuit voltage decay (OCVD) measurements utilized a KCl saturated Ag/AgCl reference electrode, a platinum mesh counter electrode, and an undyed nanoparticulate TiO_2 film working electrode. The light source for photoelectrochemical measurments was a Jobin-Yvon Fluorolog-3 fluorimeter with a xenon-arc lamp and an AM-1.5 filter.

2.2.9. Redox Shuttle/Electrolyte Solution Composition

For three-electrode dark current/voltage and OCVD measurements, only the oxidized half of the redox couple was present (*i.e.*, I_3^-, $Co(bpy)_3^{3+}$, and $Cu(PDTO)^{2+}/Cu(TBP)_{4+x}(ACN)_y^{2+}$). These electrolyte solutions utilized ACN as the solvent and included 0.1 M tetrabutylammonium hexafluorophosphate as a supporting electrolyte. The desired amount of TBP was added stepwise via micropipette. The same procedure was used for CV analyte solutions.

The redox electrolyte used in DSC fabrication consisted initially of 0.5 M $Cu(PDTO)^+$ and 0.05 M $Cu(PDTO)^{2+}$ in ACN. The $Cu(PDTO)^+$ was generated in situ by addition of an excess of copper shot to a solution consisting of 0.25 M $Cu(PDTO)^{2+}$ and 0.25 M PDTO (copper shot reduces Cu(II) via a comproportionation reaction, so non-coordinated PDTO is necessary to coordinate the newly formed Cu(I) species in solution). The resulting $Cu(PDTO)^+$ solution was syringe filtered to remove the copper shot. Solid $Cu(PDTO)^{2+}$ was then added to a 1 mL aliquot of $Cu(PDTO)^+$ to reach the desired 0.05 M $Cu(PDTO)^{2+}$ concentration. The desired amount of TBP (0.1, 0.2, or 0.5 M) was added to complete the electrolyte.

2.2.10. Electrode and DSC Fabrication

TiO_2 nanoparticulate working electrodes were fabricated on 1.5 cm x 1.5 cm FTO glass that had been cleaned via sequential sonication in detergent, acetone, and isopropanol before being blown dry by nitrogen. This FTO was coated with a 10 nm TiO_2 blocking layer via atomic layer deposition (ALD, Ultratech/Cambridge Nanotech Savannah 100) from the TTIP precursor and water. The reaction chamber was at 200 °C and the TTIP precursor was at 90 °C. The deposition recipe was as follows: 0.1 s TTIP pulse, 8 s exposure, 8 s purge; 0.015 s H_2O pulse, 8 s exposure, 8 s purge. 300 cycles resulted in thin TiO_2 films ~10 nm thick that were annealed at 500 °C (2 hour ramp, 1 hour soak) in air. TiO_2 nanoparticle films were deposited via the doctor blade technique with a scotch tape mask (area ~ 0.12 cm^2, thickness ~ 8 micrometers) and annealed via a 2 hour ramp to 300 °C, a 15 minute soak, a 30 minute ramp to 375 °C, a 15 min soak, a 30 min ramp to 450 °C, followed by a final 30 min soak at 450 °C before the furnace temperature was allowed to decay to room temperature naturally (the furnace door remained closed).

Platinum counter electrodes were prepared one of two ways. For most experiments, the Pt counter electrode was fabricated via thermal decomposition at 500 °C of H_2PtCl_6 (2 mM in isopropanol) on a 2 x 2 cm piece of FTO glass with a machined hole for electrolyte loading. For devices containing 0.5 M TBP in the redox electrolyte, a high area inverse opal (IO) coated with platinum from ALD was used. The fabrication of this electrode is described in detail in Chapter 4.

DSCs were constructed following standard procedures. The aforementioned TiO_2 photoelectrodes were dye-loaded overnight in a 3:2 mixture of chloroform and ethanol containing the Carbz-PAHTDTT dye (0.2 mM) and chenodeoxycholic acid (20 mM, to reduce

aggregation of surface-adsorbed dye molecules). The dye loaded electrodes were sandwiched with the Pt counter electrodes with a Surlyn (Solaronix Meltonix 1170-25) spacer. Following electrode sandwiching, silver epoxy was used to adhere tinned copper wires to both the photo and counter electrodes to allow for facile attachment of potentiostat electrodes. The electrolyte solution was incorporated via vacuum back loading through the pre-drilled hole in the dark electrode. This hole was sealed via Surlyn and a glass cover slide with a soldering iron. Devices were measured within 1 hour of electrolyte incorporation.

2.3. Results and Discussion

2.3.1. X-Ray Crystallography

Figure 2.3 shows the structure of a single crystal grown via slow evaporation of a solution of dichloromethane containing $Cu(PDTO)^{2+}$ and TBP at a 1:10 mole ratio.

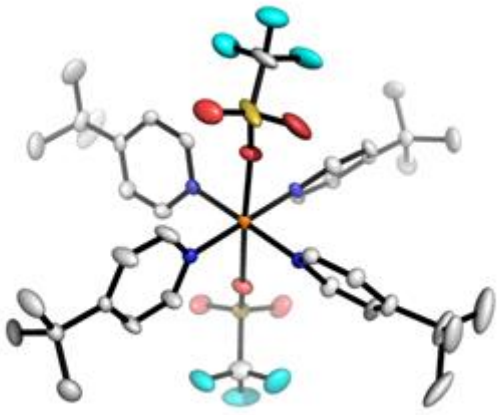

Figure 2.3. Crystal Structure of $Cu(TBP)_4(CF_3SO_3)_2$.
Structure of $Cu(TBP)_4(triflate)_2$ species obtained after slow evaporation of $Cu(PDTO)^{2+}$ in the presence of TBP. The asymmetric unit contains two crystallographically unique Cu(II) centers showing similar coordination geometries and metric parameters. Only the coordination geometry of Cu(II) is illustrated above. Color scheme: Copper (orange), nitrogen (blue), oxygen (red), sulfur (yellow), fluorine (cyan), and carbon (gray).

Despite the opportunity for chelation presented by PDTO, the trans complex of $[Cu(TBP)_4(CF_3SO_3)_2]$ is formed, *i.e.*, PDTO is completely displaced by the more Lewis-basic TBP ligand. Given that the DSC redox electrolyte employs acetonitrile as solvent and contains an excess of TBP, solution-phase coordination of triflate anions is unlikely. The species present in solution is most likely a 4, 5, or 6 coordinated TBP complex, denoted $Cu(TBP)_{4+x}(ACN)_y^{2+}$, where acetonitrile solvent occupies any copper(II) sites not filled by TBP.

2.3.2. EPR Spectroscopy

Electron paramagnetic resonance (EPR) spectroscopy was employed to elucidate and differentiate the possible copper(II) species present in solution. The X-band (~ 9.32 GHz) continuous wave EPR spectrum of $Cu(PDTO)^{2+}$ reveals a single Cu(II) species, distinct from the metalating $Cu(CF_3SO_3)_2$ salt (Figure 2.5). The $Cu(PDTO)^{2+}$ EPR spectrum is axial, $g_{||} = 2.168$, and $g_{\perp} = 2.038$, characteristic of a Cu(II) center; see Figure 2.4 A.

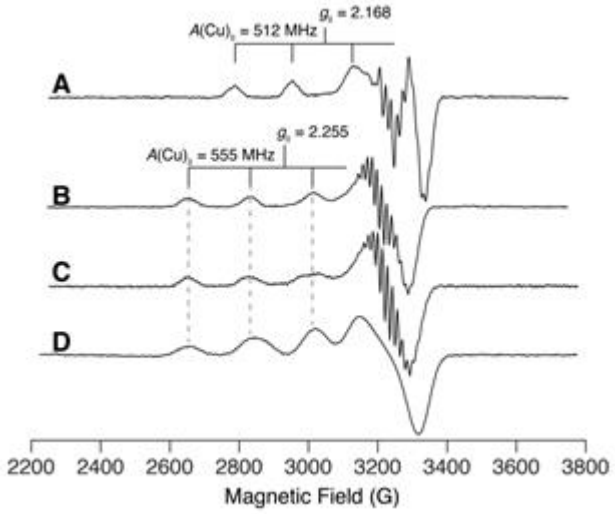

Figure 2.4. X-Band Continuous Wave EPR Spectra of Cu(II) Species.
X-band (9.230–9.234 GHz) continuous wave EPR of (A) $Cu(PDTO)^{2+}$, (B) $Cu(PDTO)^{2+}$ + TBP(excess), (C) the frozen solution of the ethanol-dissolved crystalline powder of $Cu(TBP)_4(CF_3SO_3)_2$ denoted $Cu(TBP)_x^{2+}$, (D) and crystalline powder of $Cu(TBP)_4(CF_3SO_3)_2$. $g_{\|}$ and $A(Cu)\|$ values are indicated within the figure, with B-D having equivalent parameters. Complete EPR parameters with simulations (*g*-values and hyperfine couplings) are detailed in Table 2.1. A-C were collected with 4 G modulation amplitude, 1 sec time constant, and 8 minute scan time at 77 K. D was collected with 4 G modulation amplitude, 30 ms time constant, and 2 min scan time at room temperature.

Table 2.1. Copper EPR Spectral Parameters.

	$g_{\perp}$	$g_{\|}$	$A(Cu)_{\perp}$[a]	$A(Cu)_{\|}$	$A(^{14}N)_{\perp}$	$A(^{14}N)_{\|}$
$Cu(CF_3SO_3)_4^{2+}$	2.085	2.432	35	340	–	–
Cu(PDTO)	2.0384	2.168	75	512	50.5 38.5	38 38
Cu(PDTO)+TBP[b]	2.054	2.255	47	555	39	30.5
Cu(TBP)[b]	2.054	2.255	47	555	39	30.5
Cu(TBP) (powder)	2.05	2.25	80	560	–	–

[a]All hyperfine values are given in units of MHz.
[b]Simulated with 5 equivalent nitrogen (^{14}N) nuclei.

The copper hyperfine coupling observed along $g_{\|}$ is $A(^{63,65}Cu)_{\|}$ = 512 MHz as determined by simulation (Figure 2.5). Resolved ^{14}N hyperfine coupling is observed in the $g_{\perp}$ region from the two nitrogen donors.

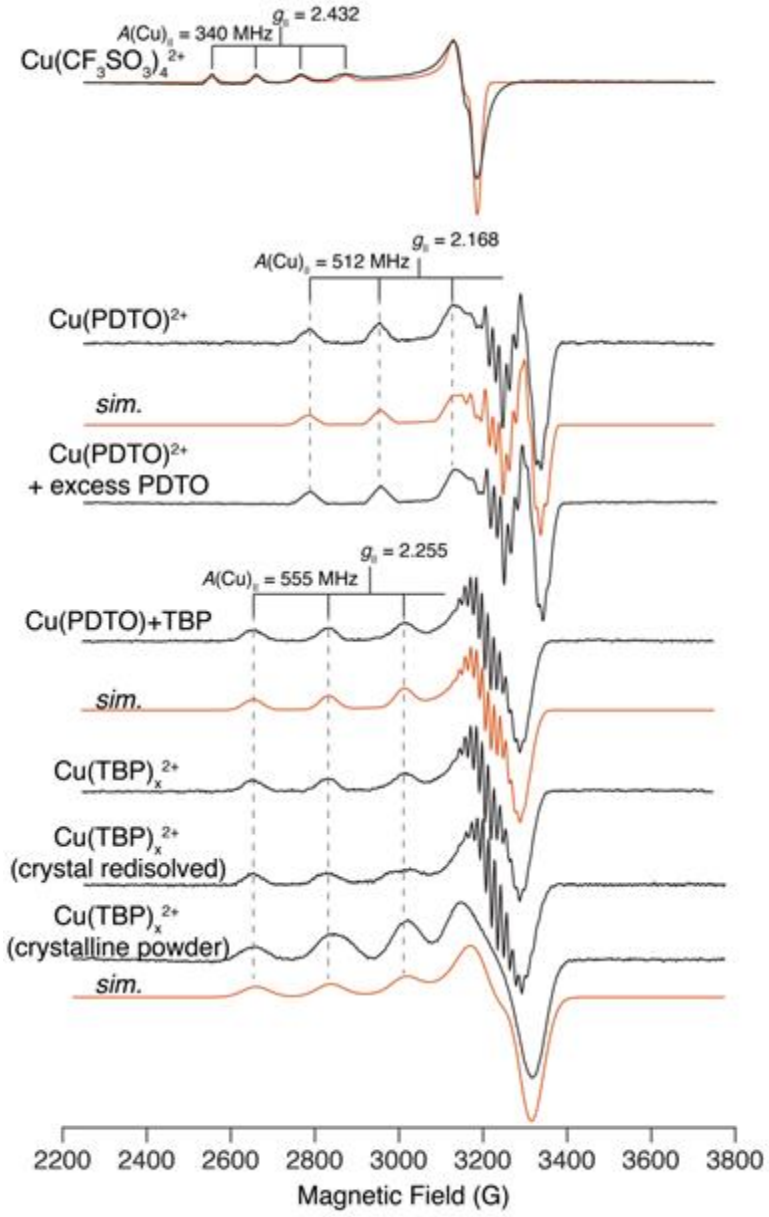

Figure 2.5. Collected and Simulated EPR Spectra.
The spectra were collected in the same manner as those in Figure 2.4. Simulation parameters are given in Table 2.1.

The X-band EPR of $Cu(PDTO)^{2+}$ is well simulated with two coordinating nitrogens, $A(^{14}N\text{-}1)_{\parallel} = A(^{14}N\text{-}2)_{\parallel}$ = 38 MHz for each nitrogen $A(^{14}N\text{-}1)_{\perp}$ = 38.5 and $A(^{14}N\text{-}2)_{\perp}$ = 50.5 MHz, supported by Q-band ENDOR spectroscopy (Figure 2.6).

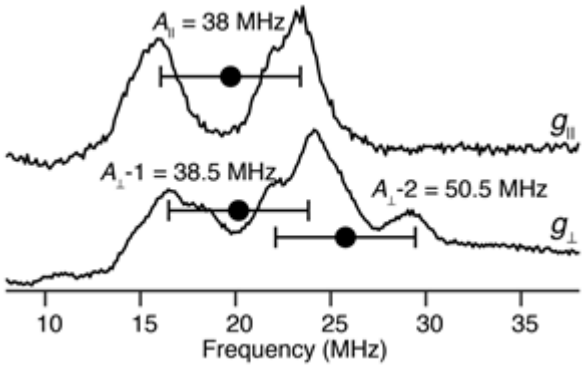

Figure 2.6. Q-band pulsed Davies ENDOR spectra of Cu(PDTO)$^{2+}$.
Q-band (34.93 GHz) pulsed Davies ENDOR spectra of Cu(PDTO)$^{2+}$ at $g_{\|}$ (11680 G) and $g_{\perp}$ (12140 G) taken at 2 K collected on instrumentation previously described.[80] The observed ^{14}N couplings are $A/2$ centered (circles) split by $2\nu_n$ (goalposts). At $g_{\|}$, only a single doublet is observed corresponding to overlapping $A_{\|}$ for two nitrogens. At $g_{\perp}$, two nitrogens are resolved with couplings of $A(^{14}\text{N-1})_{\perp}$ = 38.5 and $A(^{14}\text{N-2})_{\perp}$ = 50.5 MHz. These ^{14}N hyperfine coupling values are employed in the corresponding X-band EPR simulation of Cu(PDTO)$^{2+}$. *Conditions.* Pulse sequence: $\pi - T_{RF} - \pi/2 - \tau - \pi - \tau$ –echo; π = 80 ns; τ = 600 ns; T_{RF} = 15 µs; repetition time = 20 ms.

Upon the addition of excess TBP to the Cu(PDTO)$^{2+}$ solution, a new EPR spectrum corresponding to a single Cu(II) species is observed, Figure 2.4 B. The $g_{\|}$ value dramatically shifts to a lower magnetic field, $g_{\|}$ = 2.255, and the corresponding $A(\text{Cu})_{\|}$ increases to 555 MHz. The loss of the more covalently bound sulfur ligands localizes spin density on the copper center and is evidenced by the increased Cu hyperfine coupling for Cu(TBP)$_{4+x}$(EtOH)$_y^{2+}$ (note that EtOH is the solvent used in the EPR experiments, not acetonitrile). The observed $A(\text{Cu})_{\|}$ resembles that of previously characterized type-2 copper centers.[81] Once again, resolved ^{14}N hyperfine coupling of $A(^{14}\text{N})_{\perp}$ = 39 MHz is observed in the $g_{\perp}$ region, associated with coordination of four equivalent equatorial ^{14}N nuclei of the TBP ligands, corroborated by x-ray diffraction (see above).

Solutions and crystalline powders of Cu(TBP)$_{(4+x)}^{2+}$ exhibit similar g values (Figure 2.4 B and D), the latter with no resolved ^{14}N hyperfine coupling. Slight differences or shifts in g

values between the solution and crystalline powder may be attributed to crystal packing affects, and/or Jahn-Teller distortions in either sample. The EPR spectrum of the ethanol dissolved $Cu(TBP)_{(4)}(CF_3SO_3)_2^{2+}$ crystal (Figure 2.4 C) is fundamentally identical to the solution prepared $Cu(TBP)_{(4+x)}(EtOH)_y^{2+}$ sample (Figure 2.4 B), corroborating the assignment of identical ligation in the two environments.

2.3.3. Electronic Absorption Spectra

Figure 2.7 shows UV-Vis absorption spectra of a solution of nominally $Cu(PDTO)^{2+}$ in the absence and then presence of ten equivalents of TBP. The key spectral features are those between 200 and 450 nm. The prominent peak at ~360 nm for $Cu(PDTO)^{2+}$ without TBP is attributed to sulfur(PDTO)-to-copper(II) charge transfer while the feature at 260 nm results from a nitrogen(PDTO)-to-copper(II) charge transfer.[82]

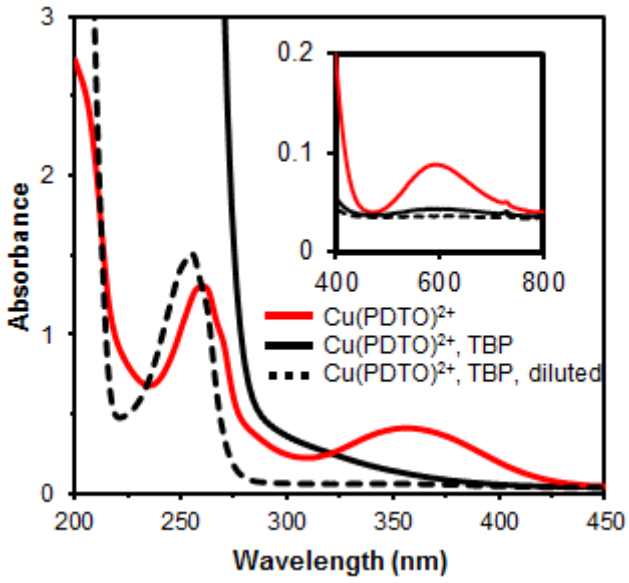

Figure 2.7. UV-Vis spectroscopy of $Cu(PDTO)^{2+}$ in acetonitrile with and without excess TBP. UV-Vis spectroscopy of $Cu(PDTO)^{2+}$ in acetonitrile without (red) and with (black) excess TBP (10 mole equivalents) in acetonitrile. The black dashed line is identical to $Cu(PDTO)^{2+}$ with TBP but diluted 5X in order to resolve the absorption feature.

In the presence of 10 mole equivalents of TBP, the 360 nm transition disappears nearly completely while a new, large TBP-related feature appears (approximately 250 nm, resolved at 5X dilution, Figure 2.7 black dashed trace). Spectral overlap between TBP and copper-pyridine transitions associated with the coordination complex complicates interpretation of the 250 nm peak, but the disappearance of the sulfur-copper charge-transfer transition at 360 nm suggests the total replacement of the PDTO ligand with coordinated TBP (consistent with the crystal structure and EPR results above). To glean information on the equilibrium of the copper system, $Cu(PDTO)^{2+}$ was titrated with TBP. The resulting UV-Vis spectra are not shown here, but a plot of the magnitude of the absorbance for the d-d transition near 600 nm versus the number of equivalents TBP added for this titration is shown in Figure 2.8.

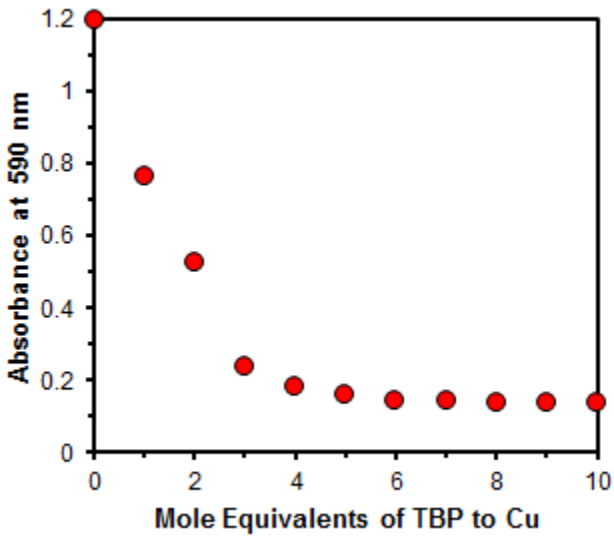

Figure 2.8. Magnitude of Absorbance at 590 nm Versus TBP Added for $Cu(PDTO)^{2+}$/TBP. Magnitude of absorbance at 590 nm for 4 mM $Cu(PDTO)^{2+}$ with added TBP. Initial additions cause sharp decreases in absorbance, but these changes decrease to ~0 around six equivalents of TBP.

Sharp decreases in absorbance are evident for the first four equivalents of TBP, with much smaller changes for the fifth and sixth, and almost no change beyond six equivalents. The

simplest interpretation is that the addition of six equivalents of TBP results in complete displacement of PDTO and that the resulting copper(II) complex coordinates five or six TBP molecules (given the known preference of copper(II) for 5- or 6-coordination).

As shown in Figure 2.9, the UV-Vis absorption spectrum of initially $Cu(ACN)_4^+$ plus one equivalent of PDTO shows transitions at 310, 260, and *ca.* 200 nm. Given the chelating nature of PDTO, this trace can be assigned as that of four-coordinate $Cu(PDTO)^+$.

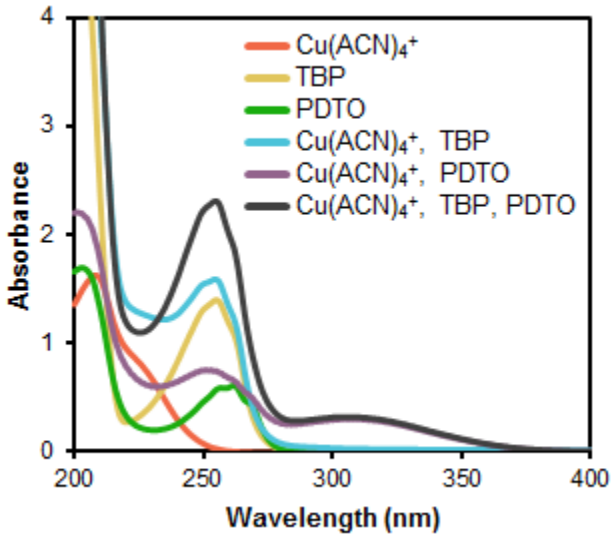

Figure 2.9. UV-Vis of $Cu(ACN)_4^+$, TBP, PDTO, and Various Combinations of the Three. Tetrakisacetonitrilecopper(I) hexafluorophosphate ($Cu(ACN)_4^+$, 1 mM) with excess TBP (10:1 ratio versus Cu) in both the presence (black) and absence (blue) of PDTO (1:1 ratio versus Cu). For comparison, the spectra of $Cu(ACN)_4^+$ alone (red), $Cu(ACN)_4^+$ with PDTO (1:1 ratio, purple), TBP alone (yellow), and PDTO alone (green) are included. These ratios were chosen to match those typically found in an operating DSC.

Notably, the addition of 10 equivalents of TBP does not diminish the broad peak at 310 nm (associated here with copper-sulfur bonding)[82] when PDTO is present. The 310 nm transition is not observed when $Cu(ACN)_4^+$ alone is combined with 10 equivalents of TBP. Furthermore, stepwise addition of PDTO to a $Cu(ACN)_4^+$-TBP mixture engenders an absorbance at 310 nm,

consistent with strong preferential binding of sulfur by copper(I), Figure 2.10. Thus, in oxidation state (I), the copper center persists as the PDTO complex under conditions where the copper(II) form is fully converted to the TBP (or TBP + ACN) complex, $Cu(TBP)_{4+x}(ACN)_y^{2+}$.

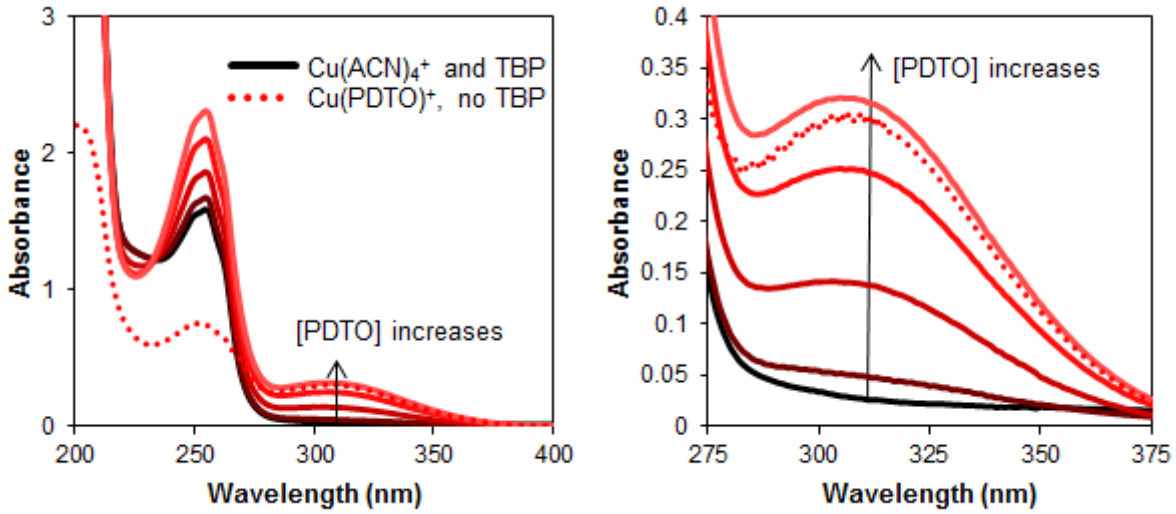

Figure 2.10. UV-Vis of $Cu(ACN)_4^+$ and TBP Titrated with PDTO.
UV-Vis spectra of tetrakisacetonitrile copper(I) hexafluorophosphate in the presence of 10 mole equivalents TBP and titrated with PDTO. The figure on the right is a magnified section of the figure on the left. The solid traces begin with no PDTO present (black), then progress to 1:100 PDTO:TBP ratio (1:10 PDTO:Cu ratio), 4:100, 7:100, and finally 1:10 PDTO:TBP (1:1 PDTO:Cu). Of particular importance is the immediate reappearance of the absorption feature associated with sulfur-copper bonds near 315 nm, even when TBP is present in 100X higher concentration. The dotted red line represents $Cu(ACN)_4^+$ in the presence of one mole equivalent of PDTO and the absence of TBP. The large difference in absorbance at ~250 is likely due to the location of a main absorbance feature of TBP in the same area (see Figure 2.9).

2.3.4. Dark Electrochemical Behavior

Three-electrode dark voltammetry and open-circuit-voltage-decay (OCVD) measurements were performed as a function of amount of added TBP. Both experiments give insight into the potential-dependent rate of reverse ET from TiO_2 to the oxidized form of a shuttle—a process whose rate (at a given potential) must be minimized in order to attain high PCEs in operating dye

cells. For simplicity, however, only the oxidized form of copper(II) (*i.e.*, $Cu(PDTO)^{2+}$ before the addition of TBP) was included in solution.

Figure 2.11a shows the voltammetric effects at TiO_2 of successive TBP additions to *ca.* 50 mM Cu^{2+} (introduced as $Cu(PDTO)^{2+}$), starting with 0 equivalents of TBP and culminating in 10 equivalents.

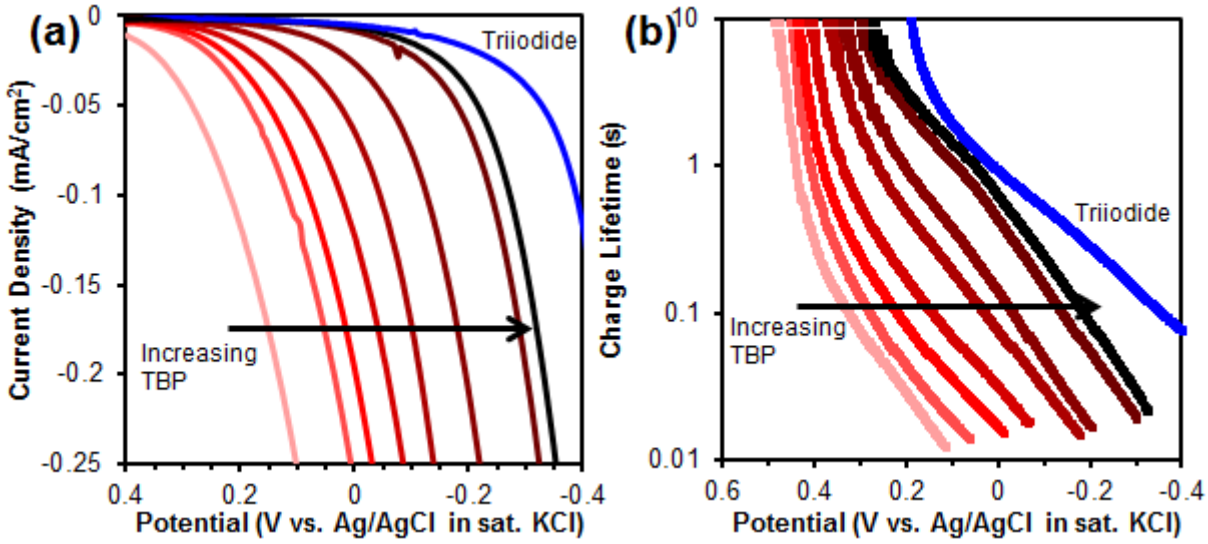

Figure 2.11. Dark Current and OCVD of Initially $Cu(PDTO)^{2+}$ with Increasing [TBP].
a) dark currents, and b) open-circuit voltage decays of (initially) $Cu(PDTO)^{2+}$ in the presence of varying concentrations of TBP. The amount of TBP varies from 0 equivalents (pink, left) and includes from left to right 1-5, 8 and 10 equivalents. 10 equivalents (black line) is equal to the standard operating concentration of TBP in DSCs (0.5 M). For comparison, triiodide data (also with 10 equivalents of TBP) are included (blue line).

The latter corresponds to a total TBP concentration of *ca.* 0.5 M, of which roughly half is present in solution and half in the form of $Cu(TBP)_{4+x}(ACN)_y^{2+}$. The observed dark current is due to reduction of Cu(II) to Cu(I). Notably, the current-voltage curves are shifted to progressively more negative potentials. The magnitudes of the shifts depend slightly on the current density, J, chosen for comparison. At J = -0.1 mA/cm^2 the corresponding dark current shifts in the negative direction by ~450 mV, implying a massive decrease in the rate of reverse

ET (TiO_2-to-shuttle) at a given absolute potential. For comparison, triiodide is reduced at potentials only about 110 mV negative of those observed for Cu(II) in the presence of ten equivalents of TBP.

The results of a related experiment are shown in Figure 2.11b: survival times for injected electrons versus open-circuit potentials. With added TBP, survival times at a given potential systematically increase. Injected electrons escape by electron transfer to the oxidized form of the redox shuttle. Thus, these experiments, like those in Figure 2.11a, point to progressively slower back ET (at a given electrode potential). Equivalently, the OCVD experiments show that for a given survival time, the addition of TBP enables progressively more negative working electrode (TiO_2) potentials to be sustained. For a survival time of 0.1 s, TBP addition shifts the electrode potential by about -500 mV and to within about 150 mV of that observed with triiodide, a shuttle component known for its exceptionally slow rates of electron interception (at a given electrode potential).

A corollary to the TBP-induced shifts in electrode potential would be similar shifts in DSC open-circuit voltages (V_{oc} values), a point examined experimentally in the section that follows. Relevant for V_{oc} values, however, is the potential of the working electrode versus the counter electrode, rather than versus a fixed reference electrode as in Figure 2.11. At open circuit, the counter electrode is poised at the Nernstian potential of the redox shuttle, *i.e.*, the equilibrium potential under the conditions and at the chemical concentrations employed in the DSC. As TBP preferentially coordinates copper(II), we can expect the potential of the couple initially present as $Cu(PDTO)^{2+/+}$ to shift in the negative direction as TBP is added. Figure 2.12 shows that this is

indeed the case. An increase of the total concentration of TBP from 0 to *ca*. 500 mM shifts the potential of the Cu(II/I) couple in the negative direction by ~190mV.

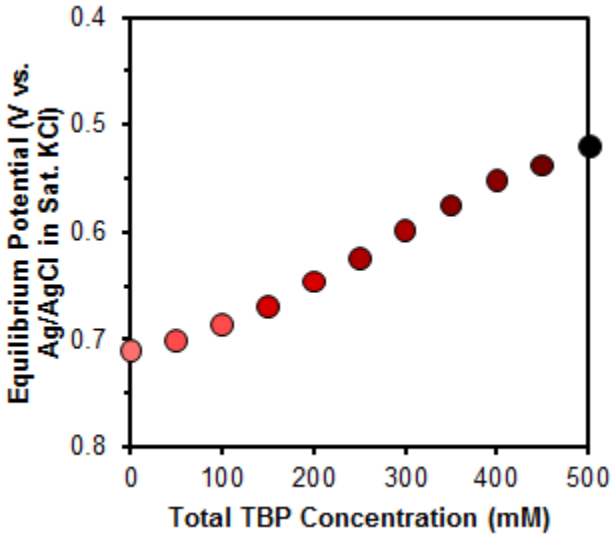

Figure 2.12. Change in Equilibrium Potential of Cu (II)/(I) with PDTO Versus [TBP].
The change in equilibrium potential of Cu(II/I)-PDTO-TBP redox species as a function of total (ligated and free) concentration of TBP.

Returning to Figure 2.11, the TBP addition—typically at 500 mM—is known to suppress dark currents and increase electron survival times even in cells featuring redox shuttles that do not chemically interact with TBP.[14, 24] The basis for the effect is not fully understood, but is believed to reflect both minor shifts in the conduction band edge of TiO_2 and TBP-adsorption-based blocking of the approach of the oxidized shuttle to the electrode.[52, 75, 83] In any case, measurements analogous to those in Figure 2.11a and Figure 2.11b were carried out using either I_3^- or $Co(bpy)_3^{3+}$, rather than Cu^{2+}, as the redox-active entity. Figure 2.13 and Figure 2.14 show that addition of TBP shifts dark current-voltage curves for both I_3^- and $Co(bpy)_3^{3+}$ in the negative direction by about 250 mV, while increasing electron survival times in OCVD experiments by about five-fold (at potentials where survival times versus Cu(II) as the electron interceptor are

increased by more than 100-fold). Thus, surface-adsorption related effects may well account for a significant fraction, though not the full amount, of the large overall effect observed with Cu(II) in response to TBP addition. Notably, with either I_3^- or $Co(bpy)_3^{3+}$ the effects of TBP addition upon both dark current-voltage curves and electron-survival times reach their maximum with about 150 mM TBP.

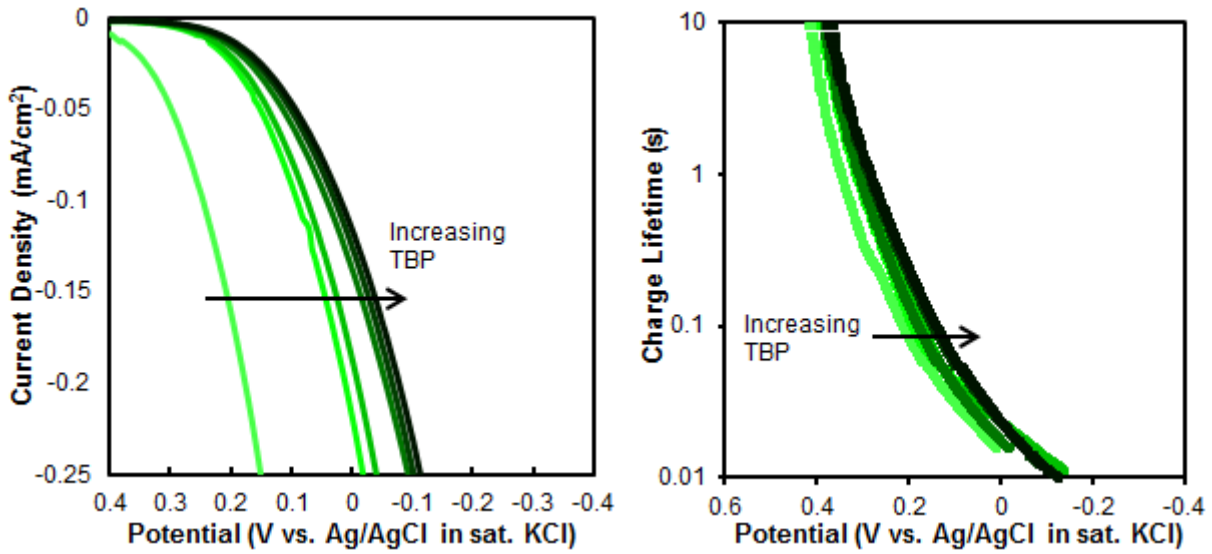

Figure 2.13. Dark Current and OCVD of $Co(bpy)_3^{3+}$ with Increasing [TBP].
Dark current/voltage curves (left) and open circuit photovoltage decay (OCVD) plots (right) for 0.5 N $Co(bpy)_3^{3+}$ in acetonitrile in the presence of increasing amounts of TBP. Similar to the trend observed with triiodide, the initial addition of 1 mole equivalent TBP has the largest effect on dark current onset. Subsequent additions to reach 2, 3, 5, 8, and 10 equivalents of TBP have a significantly smaller effect on dark current onset, likely due to TBP association with TiO_2. OCVD plots for $Co(bpy)_3^{3+}$ also show a similar trend as observed with I_3^-. Together with the data in Figure S1 for I_3^-, these results strongly support association of TBP with the copper(II) center as opposed to TBP only associating with TiO_2.

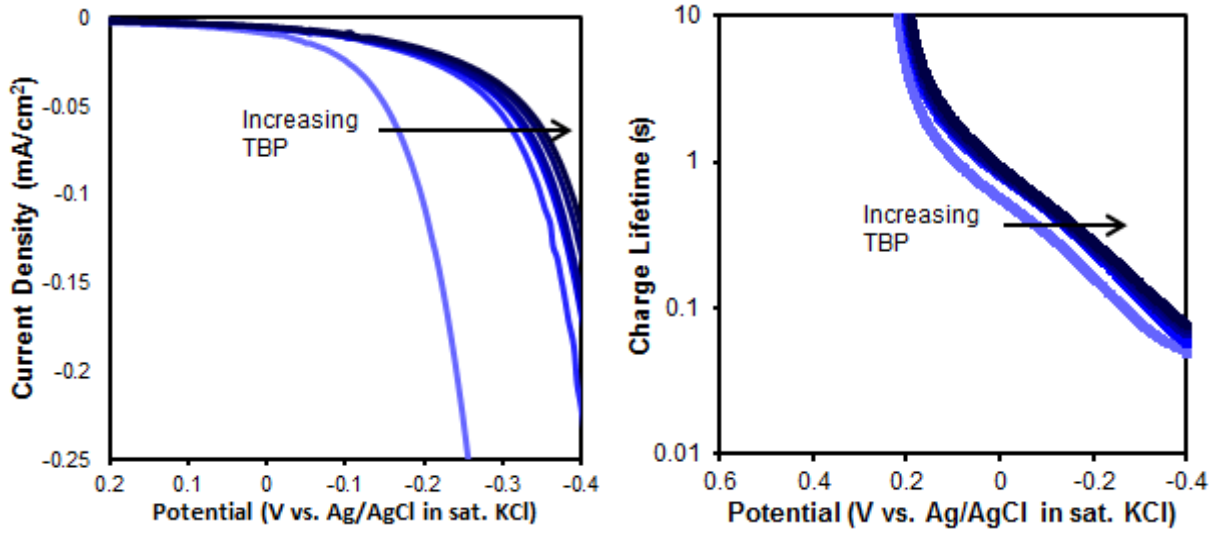

Figure 2.14. Dark Current and OCVD of I_3^- with Increasing [TBP].
Dark current/voltage curves (left) and open circuit photovoltage decay (OCVD) plots (right) for 0.5 N I_3^- in acetonitrile in the presence of increasing amounts of TBP. For the dark current curves, a large, initial increase in onset potential of approximately 200 mV is observed upon the addition of 1 mole equivalent of TBP. Further additions of TBP (2, 3, 5, 8, and 10 mole equivalents are shown, with 10 mole equivalents being roughly equal to the standard DSC operating concentration of TBP) have a minimal effect (~50 mV) on dark current onset potential. This effect is likely entirely due to surface association of TBP. OCVD plots give similar results, with the initial addition of TBP causing a small increase in charge lifetime and subsequent additions having a much smaller effect. Again, this effect is likely due to surface association of TBP with TiO_2. These effects contrast strongly with those observed with the copper shuttle, supporting the idea of interaction directly between the copper shuttle and TBP.

In contrast, starting with $Cu(PDTO)^{2+}$, the beneficial effects of TBP addition continue to increase even when the total amount of TBP added increases from 8 equivalents to 10 equivalents; see Figure 2.11. The differences presumably reflect, at least in part, the capture of 4 to 6 of the 10 equivalents to form $Cu(TBP)_{4+x}(ACN)_y^{2+}$.

2.3.5. Photoelectrochemical Behavior

With the dark behavior of the mixed copper shuttle system characterized, we moved on to photo-electrochemical measurements. Shown in Figure 2.15 are J-V plots for cells containing no, 0.1 M, 0.2 M, and 0.5 M total added TBP. It should be noted that the 0.5 M TBP device utilizes a high-area, inverse-opal Pt electrode[84] that will be described in full in Chapter 3.

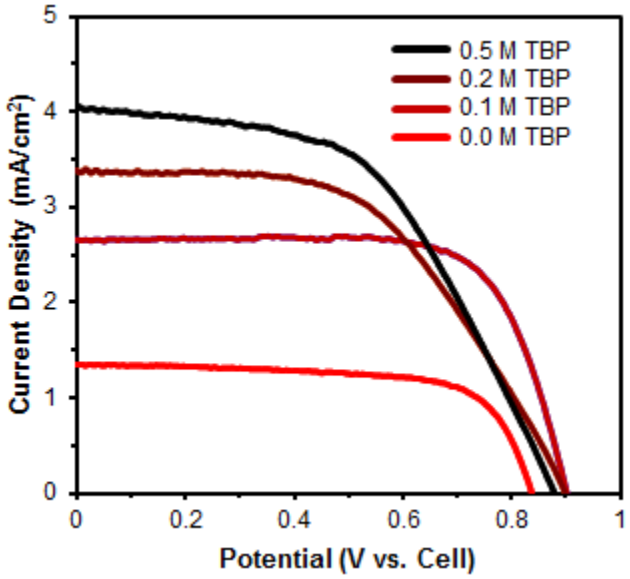

Figure 2.15. J-V Curves of the Cu(II/I) Shuttle with Various Concentrations of TBP Added. Photocurrent-voltage (J-V) curves of the Cu(II/I) couple redox shuttle in presence of increasingly large TBP (free and coordinated) concentrations. Addition of 0.5 M TBP increases the generated photocurrent by ~ 3X.

It can be seen that TBP additions increase J_{sc} values by as much as 300% (albeit, from a small initial value) and V_{oc} values by 50-75 mV. The fill-factor, however, is diminished by TBP addition. We tentatively ascribe the FF difference to residual charge-transfer resistance effects at the high-area counter electrode under conditions where regeneration of $Cu(PDTO)^{+}$ entails complete replacement of the copper center's coordination sphere.

The gains in V_{oc} upon addition of TBP and conversion of the initial form of the redox shuttle, $Cu(PDTO)^{2+/+}$, to its dual-species form, $Cu(TBP)_{4+x}(ACN)_y^{2+}/Cu(PDTO)^{+}$, are smaller than we had anticipated based on the results in Figure 2.11a for dark-current suppression. Evidently the suppression effects, which should manifest themselves as a higher (*i.e.*, more negative) potential for the dye-coated photo-anode at open circuit are appreciably offset by shifts in open-circuit potential of the counter electrode. As discussed above, the value for the latter is fixed by the

equilibrium potential of the of the redox shuttle, which indeed does shift in compensatory fashion, *i.e.*, to more negative values, when TBP is introduced.

The most striking TBP-related effect upon DSC performance clearly is the 200 to 300 percent increase in J_{sc}, with the largest enhancement emerging at the highest added TBP concentration. As discussed above, especially in connection with Figure 2.9, the composition of the reduced form of the redox shuttle—the form responsible for restoring the oxidized dye to its photoactive form—is unchanged by TBP addition. To first order, therefore, we expect the kinetics of electron transfer from Cu(I) to the oxidized dye to be unchanged by TBP addition and the yield for dye regeneration likewise to be unchanged.

The most obvious alternative explanation for the observed photocurrent enhancements are TBP-induced decreases in the rate of electron interception of injected electrons by Cu(II). In contrast to Cu(I), its coordination is completely changed (from $Cu(PDTO)^{2+}$ to $Cu(TBP)_{4+x}(ACN)_y^{2+}$) by introduction of excess TBP. Assuming that the rate of diffusion-like transport of injected electrons through the TiO_2 electrode and to the underlying current collector is largely unaffected by TBP addition, slower electron interception will translate to longer charge-collection lengths and larger photocurrents. The results of OCVD experiments (Figure 2.11b) show that rates of electron interception indeed are substantially slowed by TBP addition.

The extent of increase in J_{sc} with increasing charge-collection distance depends on how the charge collection lengths compare with optical depths, *i.e.*, the distance light must penetrate to be efficiently harvested (absorbed) by dye molecules. Light penetration distances, in turn, will vary with dye extinction and, therefore, photon wavelength. Incident photon-to-electron conversion

efficiency (IPCE) plots for cells containing either no TBP or 0.5 M (total) added TBP can be found in Figure 2.16.

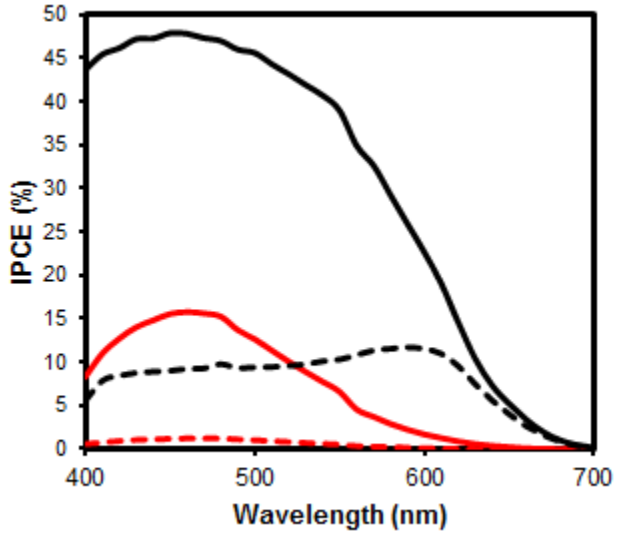

Figure 2.16. Front Side and Back Side IPCE Plots for Cu Shuttle w/ and w/o TBP.
Front-side (solid lines) and back-side (dashed lines) incident photon-to-electron conversion efficiency (IPCE) for devices with no added 4-*tert*-butylpyridine (TBP, red traces) and 0.5 M added TBP (black traces). At an illumination wavelength of 500 nm the photoelectrode features an absorbance of *ca.* 3 (see Figure S9 below). The photocurrent due to back-side illumination at this wavelength is only about 20% of the value obtained with front-side illumination. Thus, the first 80% of absorbed photons appear to be generated to distant from the current collector to contribute to J_{sc}. Assuming uniform loading of dye on the photoelectrode, 80% of the incident photons at 500 nm will be absorbed within the first 1.9 microns of the electrode. For back-side illumination, therefore, electrons generated at any distance beyond 1.9 microns are likely to be collected by the conductive glass material sited at the opposite side of the ~8-micron-thick TiO_2 electrode.

Charge collection lengths can typically be determined from the ratio of conversion efficiencies obtained when a device is illuminated through the charge collecting photoanode side (front-side) and the dark electrode side (back-side).[85] However, if the nanoparticulate TiO_2 film thickness exceeds, at most wavelengths, the distance for penetration of photons (90% light-extinction depth), as is the case here (see Figure 2.17), charge-collection lengths become difficult to quantify.

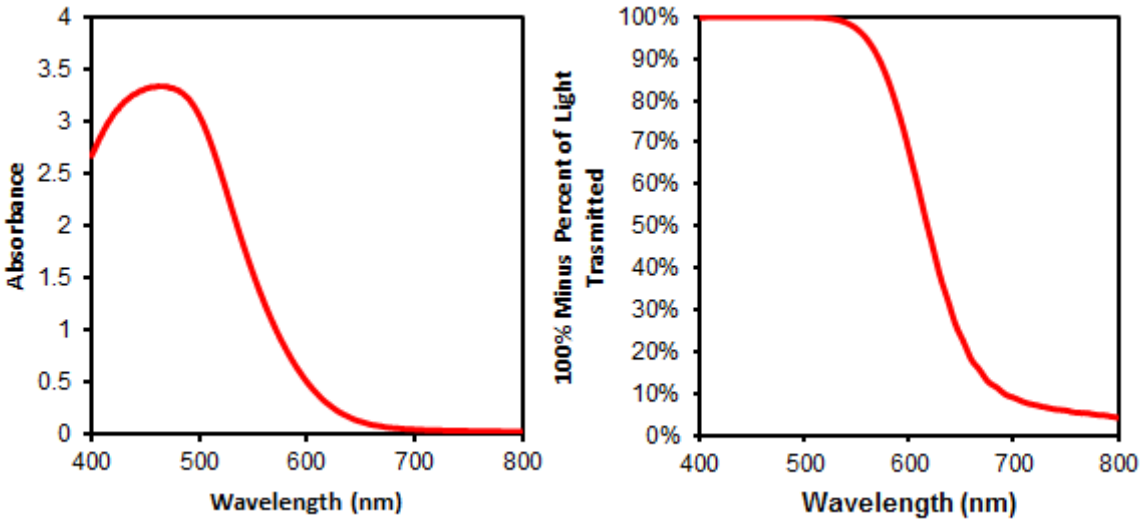

Figure 2.17. Light Harvesting Characteristics of Carbz-PAHTDTT Dye on ~ 8 Micrometer Thick TiO_2 Films.
Light harvesting characteristics of Carbz-PAHTDTT dye on ~ 8 micrometer thick TiO_2 films plotted as absorbance vs. wavelength (left) and as a percentage of light absorbed (right).

Nevertheless, based on front-side/back-side photocurrent comparisons with 8 micron thick photoelectrodes and a total TBP concentration of 0.5 M, the estimated charge-collection length is ~6 microns (see Figure 2.16 and Figure 2.17). If the absence of TBP, the collection length, as estimated by comparative front-side and back-side photocurrent output, is undefined due to ~0% conversion efficiency for back-side illumination over most of the spectrum. While the analysis is not quantitatively rigorous, it is clear that the charge-collection length in TBP-rich devices is significantly greater than in TBP-free devices, and that the difference is an important factor in obtaining larger J_{sc} values for the TBP-rich devices. Unfortunately, the maximum observed J_{sc} in the presence of TBP is still only about half of what one anticipate based solely on net light-harvesting (*i.e.* after accounting for modest reflective losses). While the small mismatch of electrode charge-collection length versus electrode thickness can account for a fraction of the disparity, the majority must have another cause or causes. We speculate that the primary cause is

inefficient (*i.e.* ~50% efficient) dye regeneration by $Cu(PDTO)^{+}$. If so, then follow-up studies with a slightly easier to reduce derivative of the oxidized dye ought to yield substantially faster regeneration kinetics, and therefore, a higher short-circuit current density.[17, 34, 35] From simple Marcus theory considerations, for example, a *ca.* 40 mV shift in dye redox potential should translate into a doubling of the dye regeneration rate.

The proximity of redox potentials for the Carbz-PAHTDTT dye and $Cu(PDTO)^{2+/+}$, coupled with the large increase in current evident upon addition of TBP, make it tempting to remove the PDTO ligand entirely from the redox couple. This, however, results in significantly worse performance in DSC devices. Figure 2.18 shows the JV curve for a PDTO free device, achieving a J_{sc} (0.78 mA/cm^2) and V_{oc} (0.59 V) significantly smaller than both the TBP free device and the $Cu(TBP)_{4+x}(ACN)_y^{2+}/Cu(PDTO)^{+}$ device.

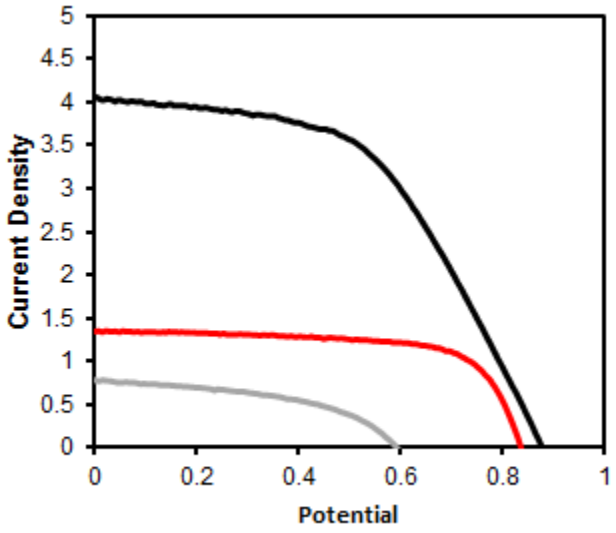

Figure 2.18. J-V Curves for TBP free, PDTO free, and Combination TBP/PDTO Devices. J-V curve of $Cu(TBP)_{4+x}(ACN)_y^{2+/+}$ (gray line) utilized as a redox shuttle in a DSC. PDTO is not present in solution in this device. For comparison, the J-V curves obtained from the $Cu(PDTO)^{2+/+}$ shuttle (red line) and the mixed system $Cu(TBP)_{4+x}(ACN)_y^{2+}/Cu(PDTO)^{+}$ shuttle (black line) are also shown.

This poor performance clearly demonstrates the necessity of the mixed Cu(II/I) system for adequate DSC operation; both the $Cu(TBP)_{4+x}(ACN)_y^{2+}$ and the $Cu(PDTO)^+$ species contribute to the improved performance.

2.3.6. Investigation of Cu(II/I) Redox Reaction

In the presence of excess TBP and one equivalent of PDTO, the reduction of Cu(II) clearly must be coupled in some fashion to replacement of TBP ligands by PDTO. As suggested by the simplified square scheme in Figure 2.19, the reduction could, in principle, proceed by electron transfer followed by chemical changes (an EC mechanism), chemical changes followed by electron transfer (a CE mechanism), a synchronous pathway entailing simultaneous reduction and ligand substitution (denoted by a diagonal dashed line in the square scheme), or some other pathway. A case could be made for any one of these pathways providing energetically or dynamically unfavorable intermediate steps that could serve to drastically slow electron transfer when the electron source is a semiconducting electrode within a dye cell.

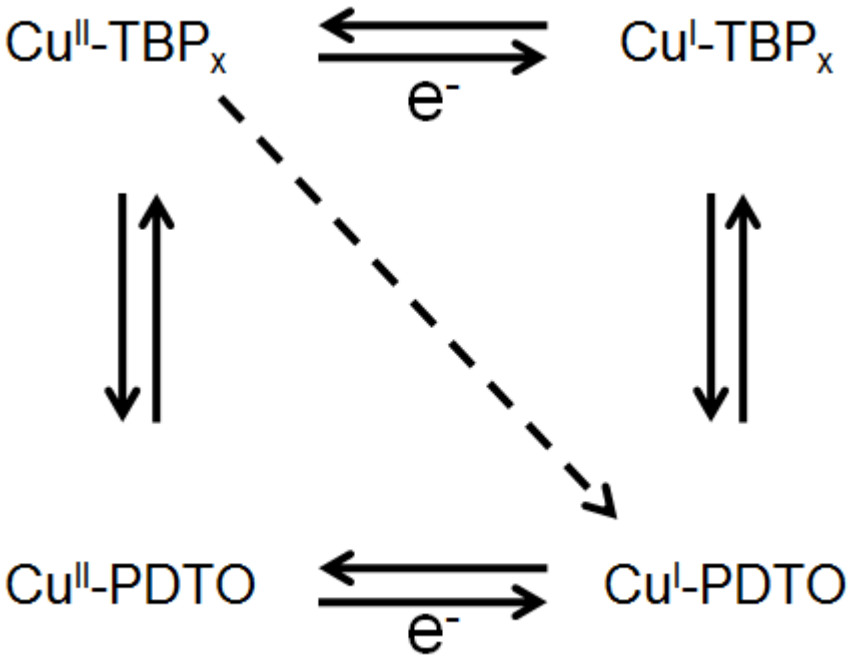

Figure 2.19. Simple Square Scheme for Relevant ET Processes of Cu Shuttle.
Simple square scheme for the reduction of $Cu(TBP)_{4+x}(ACN)_y^{2+}$ (denoted Cu^{II}-TBP) to $Cu(PDTO)^+$.

We reasoned that insight might be gained by examining the cyclic voltammetry of (initially) $Cu(PDTO)^{2+}$ at a fully conductive electrode in a three-electrode cell, without and with varying amounts of TBP. Representative voltammograms are shown in Figure 2.20.

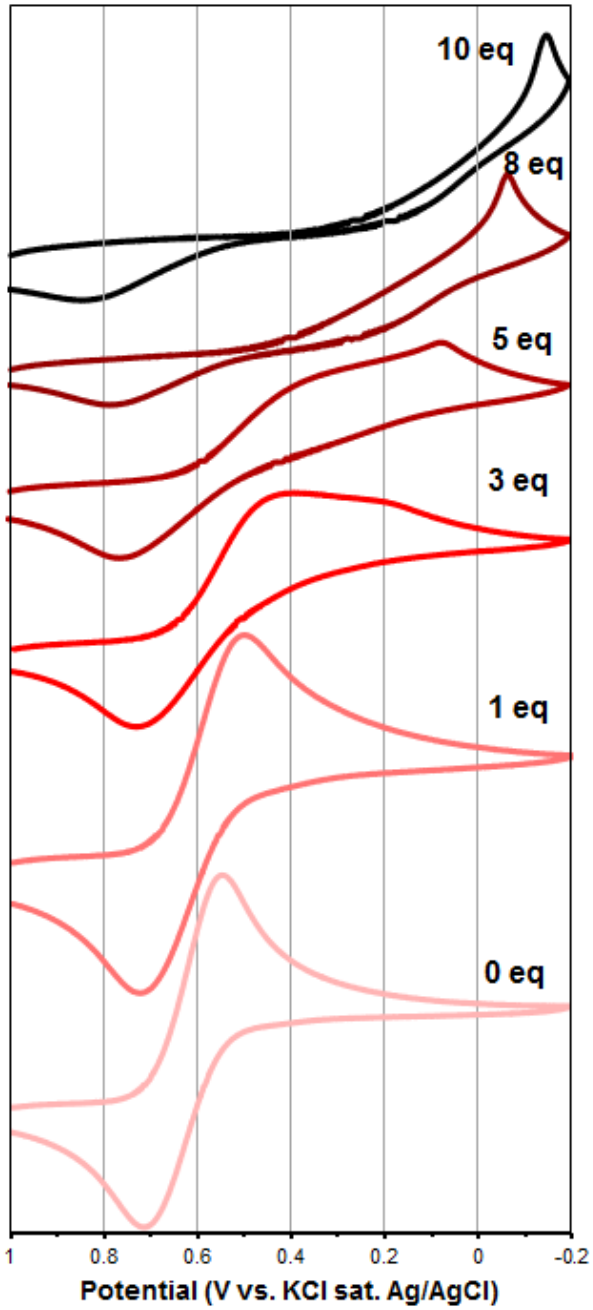

Figure 2.20. CVs of $Cu(PDTO)^{2+}$ with Increasingly Larger Amounts of TBP
Cyclic voltammograms of ~20 mM $Cu(PDTO)^{2+}$ in ACN in the presence of increasingly large amounts of TBP. Tetrabutylammonium hexaflurophosphate (0.2 M) was the supporting electrolyte, the WE was a Pt disk, and the CE was Pt mesh. The ratio of TBP:Cu is denoted above and to the right of each CV, starting with 0 equivalents before moving through 1, 3, 5, and 8 equivalents of TBP on the way to 10 equivalents total. The reduction wave for copper(II) to copper(I) shifts over 0.7 V negative at maximum TBP concentrations while the oxidative copper(I) to copper(II) wave remains relatively unchanged, shifting approximately 0.1 V positive.

In the absence of TBP, $Cu(PDTO)^{2+}$ yields a chemically reversible and electrochemically quasi-reversible (peak separation of ~0.15 V) voltammogram centered around 0.63 V. The greater than 57 mV peak separation implies a moderate rate of electron exchange between the redox couple and the electrode and is not unexpected given the likely change in coordination number and geometry upon reduction and the reversal of these steps upon re-oxidation. We assume that in the absence of TBP the additional ligand(s) for the Cu(II) form of the PDTO complex are weakly bound solvent (acetonitrile) molecules. The addition of one mole equivalent of TBP engenders a modest increase in voltammetric peak separation, with the increase reflecting mainly a negative shift in the peak associated with reduction of Cu(II). More interesting are the voltammograms with three or five equivalents of TBP; in the reductive direction these show what appear to be two overlapping reduction peaks, both shifted dramatically negative. Given the one-electron nature of the redox process, the voltammetry is strongly suggestive of the presence of Cu(II) in more than one type of coordination environment—a not unreasonable notion given the ability of Cu(II) to ligate four, five, or possibly even six TBP ligands at high TBP concentration and given the ability of some fraction of the available Cu(II) centers to ligate a sulfur of PDTO when three equivalents of TBP are present; see Figure 2.8. Further additions of TBP result in apparent consolidation of the multiple reduction waves and a separation of reduction and oxidation peaks by as much as 950 mV. Remarkably, the increased peak separation is due almost entirely to shifts in the potential of the reduction wave.

The absence of sizable shifts in the peak for oxidation of Cu(I) back to Cu(II) suggests that at all TBP concentrations the species undergoing re-oxidation is the same as in the absence of TBP,

i.e., $Cu(PDTO)^{+}$. In other words, coordination-sphere replacement appears to take place only after oxidation. In the presence of excess TBP, the envisioned sequence, in its simplest form, is:

$$Cu(PDTO)^{+} \rightarrow Cu(PDTO)^{2+} + e^{-}$$

and,

$$Cu(PDTO)^{2+} + (4 + x)TBP + y(ACN) \rightarrow Cu(TBP)_{4+x}(ACN)_y^{2+} + PDTO$$

The absence of sizable shifts in the peak for oxidation also implies that the rate of ET from the Cu(I) complex to the electrode is largely unaffected by the presence of TBP, a readily understandable observation if the identity of the electron donor in all cases is $Cu(PDTO)^{+}$, rather than a TBP-containing complex. If $Cu(PDTO)^{+}$ is indeed the electron donor in all solution compositions examined, a reasonable corollary is that the effectiveness of the Cu(I) form of the shuttle as a dye regenerator in an operational DSC will likewise be little affected by TBP addition, *i.e.*, only the rate of the undesirable back ET process (TiO_2 to Cu(II)) will be influenced. It is precisely this kind of asymmetry that we seek to introduce in operational dye cells.

Returning to Figure 2.20, in the reduction direction, in the presence of 10 equivalents of TBP, the voltammetric peak is pushed to *ca*. -0.12 V vs. Ag/AgCl. The formal potential (E_f) for the Cu(II/I) couple, while shifted slightly negative from its value in the absence of TBP is, nevertheless, far positive of the reductive peak: E_f = ~0.44 V. Thus, the reduction peak appears at an absolute overpotential of more than 500 mV, attesting to a very slow rate of conversion of $Cu(TBP)_{4+x}(ACN)_y^{2+}$ to $Cu(PDTO)^{+}$—behavior reminiscent of reduction of the oxidized form of the shuttle by electrons from TiO_2. While far from definitive, the results are suggestive of

reduction of $Cu(TBP)_{4+x}(ACN)_y^{2+}$ by a pathway that entails release of some number of TBP ligands prior to electron addition, a CE-like mechanism. Uphill ligand dissociation would be compensated mechanistically by a more positive (more favorable) redox potential for the electron-transfer step in isolation.

Despite the attractiveness of the explanation, an alternative is worth considering. In the absence of PDTO, but in the presence of 0.5 M TBP (total) in ACN as solvent, the copper based redox reaction is:

$$Cu(TBP)_{4+x}(ACN)_y^{2+} + e^- \rightarrow Cu(TBP)_4^+ + xTBP + yACN$$

where x is likely 2 or 1 and y is likely 0 or 1. The experimentally measured equilibrium potential is 220 mV, a value considerably more negative than that for the mixed $Cu(TBP)_{4+x}(ACN)_y^{2+}/Cu(PDTO)^+$ couple and within a few hundred millivolts of the reductive peak in Figure 2.20 for (initially) $Cu(PDTO)^{2+}$ in the presence of ten equivalents of TBP. Cyclic voltammetry measurements like those in Figure 2.20 (black curve; 10 equiv. added TBP), but without PDTO yield a plot with a ~450 mV peak separation and reduction wave peaking at ~-50 mV. The location of the peak potential of the reduction wave for the black trace in Figure 2.20 and the equilibrium potential for the Cu(II/I) couple in the absence of PDTO, but presence of 10 equiv. of added TBP is suggestive of an EC-like mechanism:

$$Cu(TBP)_{4+x}(ACN)_y^{2+} + e^- \rightarrow Cu(TBP)_4^+ + xTBP + yACN$$

followed by:

$$Cu(TBP)_4^+ + PDTO \rightarrow Cu(PDTO)^+ + 4TBP$$

We recognize that the "E" step as written still entails coupled chemical steps (the release of a total of 1 or 2 TBP and/or ACN ligands), but for simplicity we do not dissect the proposed reaction pathway further.

To summarize, the voltammograms provide useful information about the reduction and re-oxidation processes involved, but do not conclusively support either limiting CE or EC mechanisms. In principle, further insight could be gained by resorting to digital simulations. However, the number of chemical steps coupled to the transfer of the electron is large—at least 5 and perhaps as many as eight—suggesting that unique fits to the observed voltammograms may be difficult to attain. Additionally, the peak shape for Cu(II) reduction at high TBP concentrations is sharper than generally seen for single-electron reductions, implying that the voltammetry may be further complicated by reactant adsorption. In view of the complexity, it seems appropriate to replace the square-scheme in Figure 2.19 with the multi-square scheme shown in Figure 2.21.

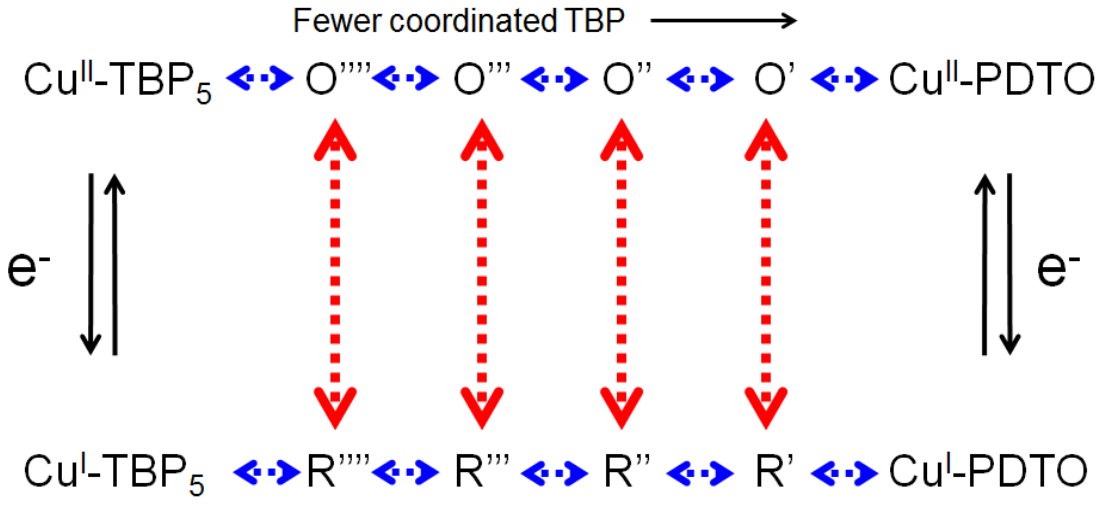

Figure 2.21. Extended Square Scheme for $Cu^{II/I}$ Redox Reaction
Extended square scheme depicting the multiple possible pathways for $Cu(TBP)_{4+x}(ACN)_y^{2+}$ reduction to $Cu(PDTO)^+$.

Thus, the extended scheme allows for the possibility of electron transfer not only before or after C steps, but also midway through a series of chemical steps.

2.4. Conclusions

A dual species redox shuttle system has been characterized and its utility in DSCs has been illustrated. While multiple redox shuttle systems have benefited from specific tuning of a single redox couple, this approach allows for tunability of both halves of a redox couple. This has clear advantages in DSC devices as each half of the redox shuttle couple has a dramatically different role in device function. While we found this specific combination of PDTO and TBP to be beneficial, both the PDTO and TBP offer many opportunities for directed modification of the shuttle environment via incorporation of different functional groups or pyridine species. As an aside, numerous sulfur, nitrogen, or mixed sulfur and nitrogen macro or pseudo-macrocycles are known to coordinate to Cu centers.[51] Some of these ligands may exhibit similar behavior in the presence of TBP, especially those of the mixed S-N variety. The PDTO macrocycle used in this work was chosen for its redox potential and ease of attainment. Modifications to the PDTO backbone may allow for a change in redox potential without eliminating the favorable interaction of the Cu(II) center with TBP, but this was not pursued. Exploratory work on changing the substituent in the 4- position of the pyridine ring showed a strong correlation between electron donating strength and dark current offset/electron lifetime for the $Cu(PDTO)^{2+}$ derived system. Additional work also revealed an expected steric effect via substituents in the 2 and/or 6 positions of the pyridine ring. Neither modification is explored further in this work, though utilization of stronger or weaker nitrogen donor molecules as additives would in theory allow for

the fine-tuning of this interaction. Returning to the system at hand, the modifications alluded to above could allow for precise tuning of redox potentials and electron transfer rates. Additionally, this tunability makes this approach applicable across nearly all dyes and architectures, as each half of the redox couple can be modified to have the necessary properties for strong device performance.

Chapter 3. High Surface Area Architectures for Improved Charge Transfer Kinetics at the Dark Electrode in Dye-Sensitized Solar Cells*

Reproduced in part with permission from Hoffeditz, W. L.; Katz, M. J.; Deria, P.; Martinson, A. B. F.; Pellin, M. J.; Farha, O. K.; Hupp, J. T. High-Surface-Area Architectures for Improved Charge Transfer Kinetics at the Dark Electrode in Dye-Sensitized Solar Cells. *ACS Appl. Mater. Interfaces* **2014,** *6*, 8646-8650 (DOI: 10.1021/am501455b).

3.1. Introduction and Background Information

One of the greatest opportunities for DSC efficiency improvement has long been increasing open-circuit voltages (V_{oc}). As previously described, the most common optimized devices have in part accomplished this by use of cobalt-based redox shuttles.[16, 48, 63, 64] Other copper,[65, 66] iron,[17, 30] or nickel[67] based outer-sphere redox couples, as well as organic molecule shuttles[68] and solid state hole conductors[86] have also found modest success in improving V_{oc}. These innovations all aim at increasing the overall PCE of DSCs, but focus almost entirely on the photoelectrode. However, improvements at the dark electrode can also lead to improved PCE. Thus, this chapter describes the fabrication and characterization of the inverse opal dark electrode used for high TBP concentration devices in Chapter 2 of this dissertation. The mechanism by which increasing the surface area of the platinum dark electrode nearly doubles the efficiency of the $Cu(TBP)_{4+x}(ACN)_y^{2+}/Cu(PDTO)^+$ redox shuttle system described in Chapter 2 is elaborated on, and a comparison between the new IO Pt dark electrodes and more traditional Pt dark electrodes is made; see Figure 3.1.

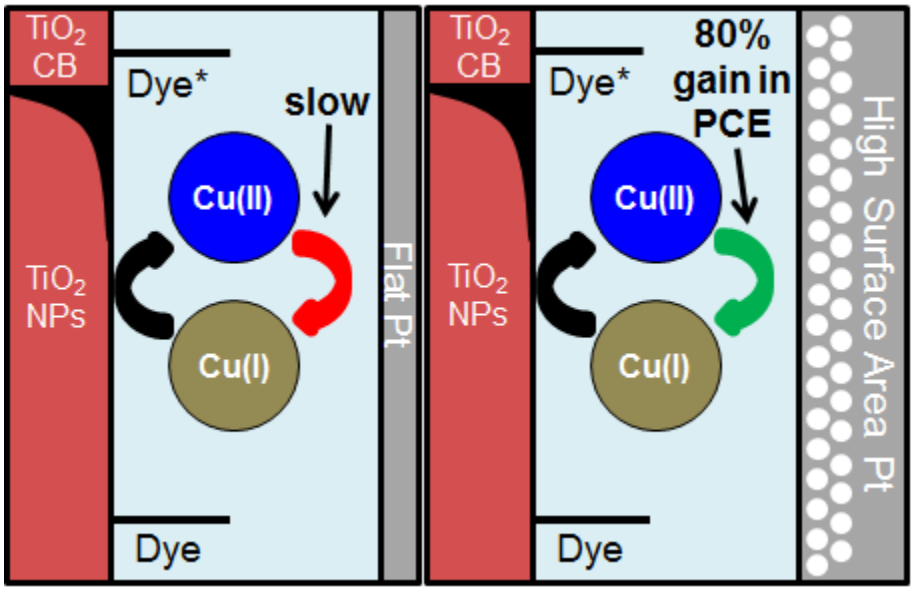

Figure 3.1. Simplified Representation of Devices Interrogated in This Study.
Schematic representation of the device architectures used in the following study. The relative PCE performance of the high area dark electrode device is increased ~80%.

The benefits of improving performance at the dark electrode are most clearly seen in the improvement of the oft-neglected fill-factor variable and its subsequent effect on η. Power conversion efficiency is calculated as in Equation 3.1,

$$\eta = \frac{J_{sc}\ x\ V_{oc}\ x\ FF}{P_{in}} \qquad (3.1)$$

where J_{sc}, V_{oc} and P_{in} represent short circuit current, open circuit voltage and incident power, respectively. FF represents the fill factor, which is related to the maximum power point of a device. A poor fill factor is typically the result of undesirable resistances within the device. This term is often taken for granted in DSCs since its value is reasonably close to optimal for I_3^-/I^-, which was by far the most commonly used redox shuttle for nearly 20 years. However, many more recent alternative shuttles have suffered in performance because of poor FF, making this term all the more important. As an example, previous work has shown that Co(2,2'-

bipyridine)$_3^{3+/2+}$, the most successful alternative shuttle to I_3^-/I^- and current DSC efficiency record holder, displays more favorable electrochemistry (faster charge-transfer kinetics) on electrodes other than platinum, i.e. gold, carbon, or polymer electrodes, among others[48]; when traditional platinum electrodes are used, the fill factor, and thus the efficiency, suffers.[26]

While a specific shuttle may benefit greatly from a novel counter electrode, the new counter electrode may not be advantageous with all redox shuttles and in some cases may actually lead to a decrease in performance.[87, 88] For example, when an inverse opal (IO) architecture was utilized with carbon-based dark electrodes, performance with the I_3^-/I^- shuttle was worse than with traditional platinum dark electrodes.[25] Ideally, an improved dark electrode could be applied to and work well for nearly all possible redox shuttle systems. Instead of devising a dark electrode that can yield larger rate constants than traditional Pt dark electrodes for a given electron transfer process, we instead choose to increase the surface area of a Pt dark electrode. While increasing the surface area of an electrode does not increase the inherent *rate* of electron transfer, it will increase the *rate constant*; a 10-fold increase in electrode surface area would be equivalent to a 10-fold increase in heterogeneous electrochemical *rate constant*. To this end, we use a copper-based redox shuttle to illustrate that large charge-transfer resistances for its reaction at the dark electrode lead to a large decrease in overall cell efficiency. We then rectify this problem by shifting to a high-area platinum dark electrode fabricated on an IO architecture using atomic layer deposition (ALD).

3.2. Experimental Methods and Instrumentation

3.2.1. Reagents and Materials

Unless otherwise noted, all chemicals were purchased from Sigma-Aldrich and used as received. Fluorine-doped tin oxide (FTO) glass was purchased from Hartford Glass (Hartford City, IN). Polystyrene microspheres (average diameter 350 nm) were purchased from Alfa-Aesar. TiO_2 nanoparticles were purchased from Dyesol. The platinum ALD precursor (trimethyl)methylcyclopentadienylplatinum(IV) was purchased from Strem. All solvents and chemicals were used as received, with the exception of reagents used in the synthesis of Carbz-PAHDTT, where care was taken to ensure purity and dryness.

3.2.2. Synthesis

The 1,8-bis-(2'-pyridyl)-3,6-dithiaoctane (PDTO, Figure 3.2) ligand was synthesized by the method of Goodwin and Lions[78] and recrystallized from hot hexanes. $[Cu(PDTO)](CF_3SO_3)_2$ was formed by mixing in ~1:1 ratio by mol copper(II) triflate with PDTO in acetonitrile and rotovapping to dryness. $[Cu(PDTO)](CF_3SO_3)$ was generated in situ by addition of dendritic copper powder to a 1:1 mixture of $[Cu(PDTO)](CF_3SO_3)_2$:PDTO in acetonitrile. For devices utilizing the mixed species form of the copper shuttle, addition of 0.5 4-*tert*-butylpyridine (TBP) led to the formation of $Cu(TBP)_{4+x}(ACN)_y^{2+}$ (see Chapter 2). $[Co(2,2'\text{-bipyridine})_3](PF_6)_2$ ($Co(bpy)_3^{2+}$) was synthesized by mixing $Co(NO_3)_2$ with 2,2'-bipryidine in a 1:3.1 ratio in methanol followed by the addition of an excess of NH_4PF_6. A portion of the resulting $Co(bpy)_3^{2+}$ was oxidized to $Co(bpy)_3^{3+}$ by the addition of $NOBF_4$ and precipitated by addition of water. The

Carbz-PAHTDTT dye (Figure 3.2) was synthesized according to literature procedure by Pavas Deria, Ph.D.[17]

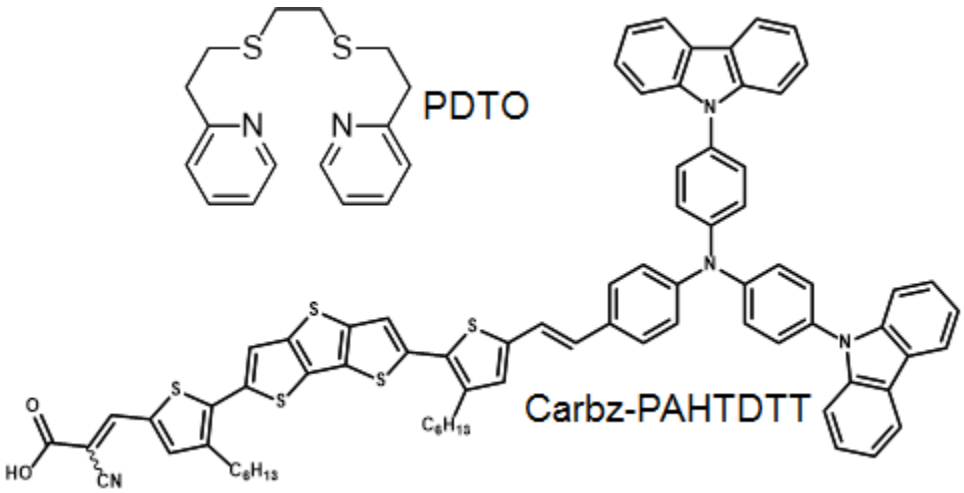

Figure 3.2. Carbz-PAHTDTT Dye and PDTO Ligand Structures.
Structure of 3-(5-{6-[5-(2-{4-[Bis-(4-carbazol-9-yl-phenyl)-amino]-phenyl}-vinyl)-3-hexyl-thien-2-yl]-dithieno[3,2-b;2',3'-d] thiophen -2-yl}-4-hexyl-thien-2-yl)-2-cyano-acrylic acid, referred to in the text as Carbz-PAHTDTT, and 1,8-bis(2'-pyridyl)-3,6-dithiaoctane, referred to as PDTO.

3.2.3. Platinized Inverse Opal Dark Electrode Fabrication

Inverse opals (IO) were fabricated based on the method of Hatton, et. al.[89] A tetraethyl orthosilicate (TEOS) stock solution was prepared from 1.5 mL ethanol, 1 mL deionized water, 1 mL TEOS, and 8.1 microliters of concentrated HCl. This stock solution was stirred for no less than 15 minutes. The IO stock solution consisted of 1 mL of 350 nanometer diameter polystyrene spheres, 20 mL of deionized water, and 0.15 mL of the TEOS stock solution described above. The IO stock solution was sonicated for 30 minutes. Polystyrene/silica opal structures were formed on 2 cm X 2 cm FTO glass via slow evaporation (24 hours at 65 °C) of the IO stock solution, with the FTO glass being oriented vertically in the IO solution. Note that the FTO glass had a machine drilled hole to allow for future vacuum loading of electrolyte solution. The final IO SiO_2 was obtained after heat treatment of the opal films, which utilized a 4 hour ramp to 500

°C, a 2 hour soak, and a 4 hour ramp down to room temperature. This method resulted in uniform films approximately 5.4 micrometers (~15 fcc layers) thick.

These SiO_2 inverse opals were platinized via ALD. The ALD used was a Savannah 200 reactor manufactured by Ultratech/Cambridge NanoTech. The Pt precursor was held at 75 ^{o}C, and 500 alternating cycles of Pt (1 s pulse, 5 s expo, 8 s nitrogen purge) and O_2 (2 s pulse, 9 s nitrogen purge) resulted in ~12 nm of Pt growth on the IO framework. The electrochemically accessible surface area was determined via CV measurements in 2 M H_2SO_4 and was found to be ~50 X the geometric surface area (see results and discussion Section 3.3.1).

3.2.4. Fabrication of Standard Platinum Dark Electrode

DSC "standard" Pt dark electrodes, referred to as TD Pt with TD standing for thermal decomposition, were formed by thermal decomposition of a platinic acid. Specifically, 15 microliters of 5 mM H_2PtCl_6 in isopropanol was drop cast onto 2 cm X 2 cm FTO glass with a machined hole for future electrolyte loading. The FTO was tilted as necessary to ensure complete coverage by the H_2PtCl_6 solution. Heating at 500 °C for 30 minutes resulted in the thermal decomposition of H_2PtCl_6, forming the TD Pt dark electrodes used for this study.

3.2.5. Electrochemical Impedance Spectroscopy of Dark Electrodes

Electrochemical impedance measurements were taken on a Solartron 1286 electrochemical interface coupled to a SI 1260 impedance/gain-phase analyzer using the two-dark-electrode setup depicted in Figure 3.3 with shuttle concentrations identical to those used in constructed photocells.

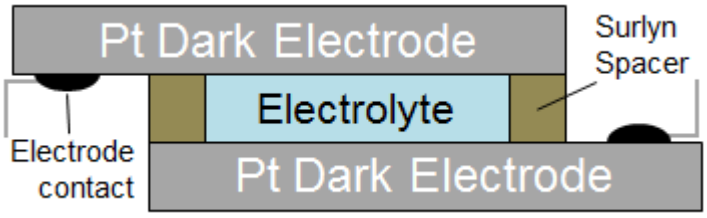

Figure 3.3. Schematic Representation of 2-Electrode Setup for EIS of Dark Electrodes
Schematic representation of the 2-electrode setup used for EIS measurements, featuring two Pt electrodes sandwiched together with a Surlyn spacer and vacuum back filled with the desired redox electrolyte solution.

The two electrode device was fabricated by sandwiching two IO Pt or TD Pt dark electrodes together using Surlyn as both a spacer and to define the active area. Redox electrolyte solutions of I_3^-/I^-, $Co(bpy)_3^{3+/2+}$, and $Cu(TBP)_{4+x}(ACN)_y^{2+}/Cu(PDTO)^+$ where loaded via vacuum back filling. I_3^-/I^- solutions contained 0.6 M 1,2-dimethyl-3-propylimidazolium iodide, 0.05 M I_2, and 0.5 M TBP. $Co(bpy)_3^{3+/2+}$ solutions consisted of 0.2 M $[Co(bpy)_3](PF_6)_2$, 0.02 M $[Co(bpy)_3](PF_6)_3$, and 0.5 M TBP. $Cu(TBP)_{4+x}(ACN)_y^{2+}/Cu(PDTO)^+$ solutions were 0.5 M $[Cu(PDTO)](CF_3SO_3)$, 0.05 M $[Cu(TBP)_{4+x}(ACN)_y](CF_3SO_3)_2$, with 0.5 M TBP being added to solution to form the Cu-TBP species.

3.2.6. DSC Fabrication and Measurement

Dye-cell photoanodes (nanoparticulate TiO_2 on FTO, 6 microns thick; no scattering layer) were prepared by standard methods and dye loaded overnight in Carbz-PAHTDTT dye (0.2 mM) in 3:2 chloroform:ethanol solution containing 20 mM chenodeoxycholic acid (to inhibit aggregation of the adsorbed form of the dye). Photoanodes were sandwiched and heat-sealed (using a Surlyn spacer) with either IO Pt or TD Pt counter electrodes and vacuum back-loaded with the desired electrolyte solution. Photoanodes for three-electrode experiments were prepared in the same manner without sandwiching. Photo-electrochemical measurements were performed

using a Jobin-Yvon Fluorolog-3 fluorimeter with a xenon-arc lamp and AM-1.5 filter as the light source and a Solartron Analytical 1 MS/s potentiostat in a Modulab box. Three-electrode measurements were performed with a platinum mesh counter electrode and KCl saturated Ag/AgCl reference electrode in 1 mL of copper shuttle-containing solution using dye-loaded TiO_2 as the working electrode.

3.3. Results and Discussion

3.3.1. Characterization of Inverse Opals

The fabricated IO films were characterized primarily via SEM. Top-down and-cross sectional SEM images of a typical IO film are shown in Figure 3.4.

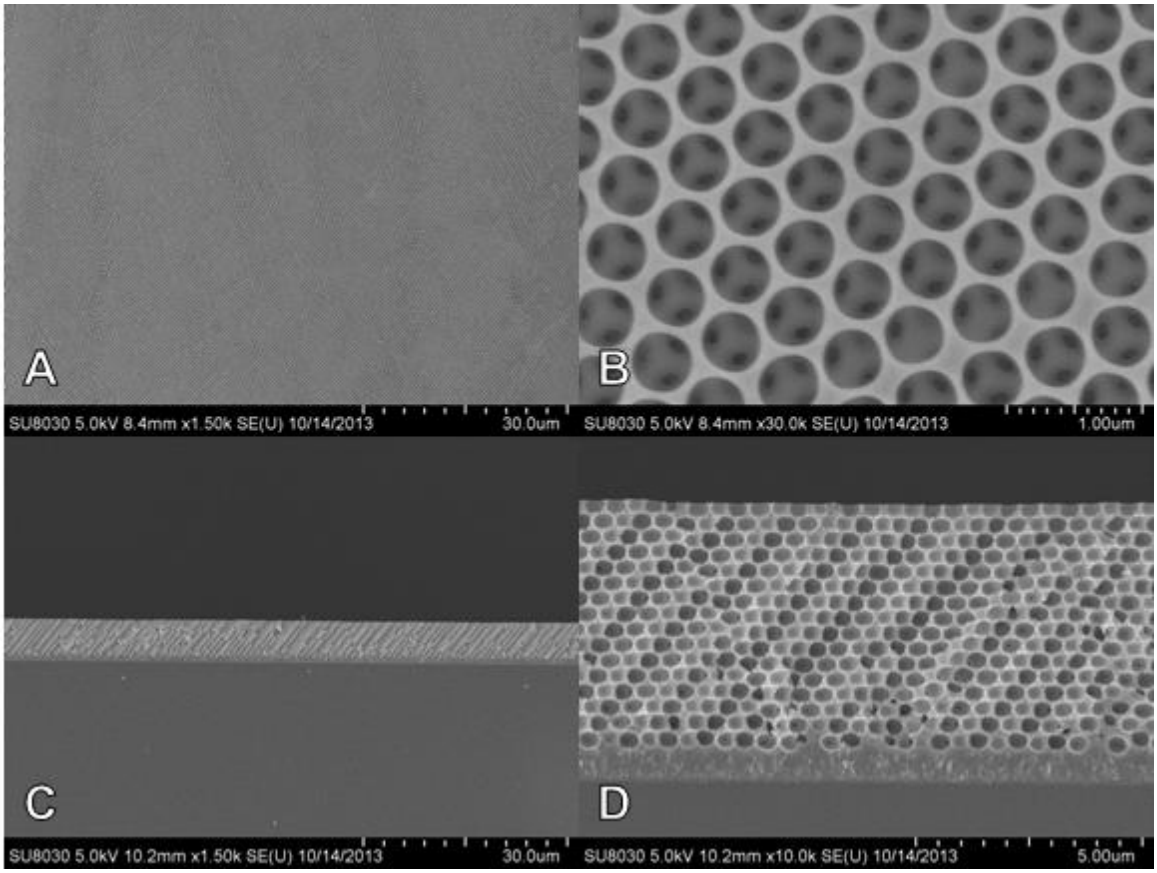

Figure 3.4. SEM Images of Typical IO Film.
Top-down (A & B) and cross-sectional (C & D) SEM images of an IO film fabricated as described in the experimental section. The film is crack free over long distances (A) and is approximately 5.4 micrometers thick (C) with ~15 stacked fcc layers of spherical voids (D).

The IO films show good uniformity and are crack free over long distances. Use of 350 nm diameter polystyrene spheres results in 350 nm diameter spherical voids. The average film thickness of 5.4 micrometers suggests ~15 stacked layers of voids, supported by the image in Figure 3.4 D. After platinization of the IO using ALD, cyclic voltammetry was used to interrogate the electrochemically active surface area. The CVs were recorded in 2 M H_2SO_4 and the resulting current from H^+ desorption was used to determine the active surface area.[90] The voltammograms are shown in Figure 3.5.

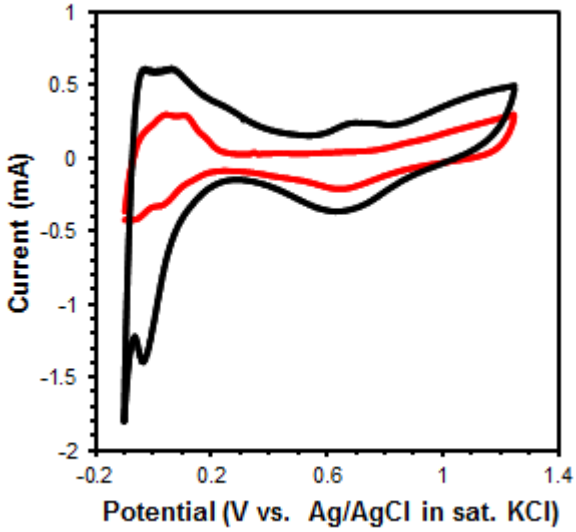

Figure 3.5. CVs of TD Pt and IO Pt Dark Electrodes for Surface Area Determination
CV of TD Pt (red) and IO Pt (black) as the working electrode in 2 M H_2SO_4. The scan rate was 200 mV/s for the TD Pt and 10 mV/s for the IO Pt.

The voltammograms were integrated between -0.05 V and 0.25 V for the anodic current only. By subtracting capacitive background current from the integrated current and dividing by the scan rate, the charge of the surface can be calculated. Dividing the surface charge value of both electrodes by their geometric surface area and comparing these numbers gives the accessible surface area enhancement of the IO Pt compared to TD Pt. Here, that enhancement was ~ 50 X for IO Pt compared to TD Pt, in close agreement with values previously reported for this IO fabrication.[91]

3.3.2. Charge Resistance at the Dark Electrode by EIS

Electrochemical impedance spectroscopy was used to determine magnitudes of charge resistance at TD Pt electrodes, first with the common I_3^-/I^- and $Co(bpy)_3^{3+/2+}$ redox shuttles and

then with the new copper-based shuttle, using the experimental setup shown in Figure 3.3. The resulting Nyquist plots for no applied bias are shown in Figure 3.6 (red, green and brown lines).

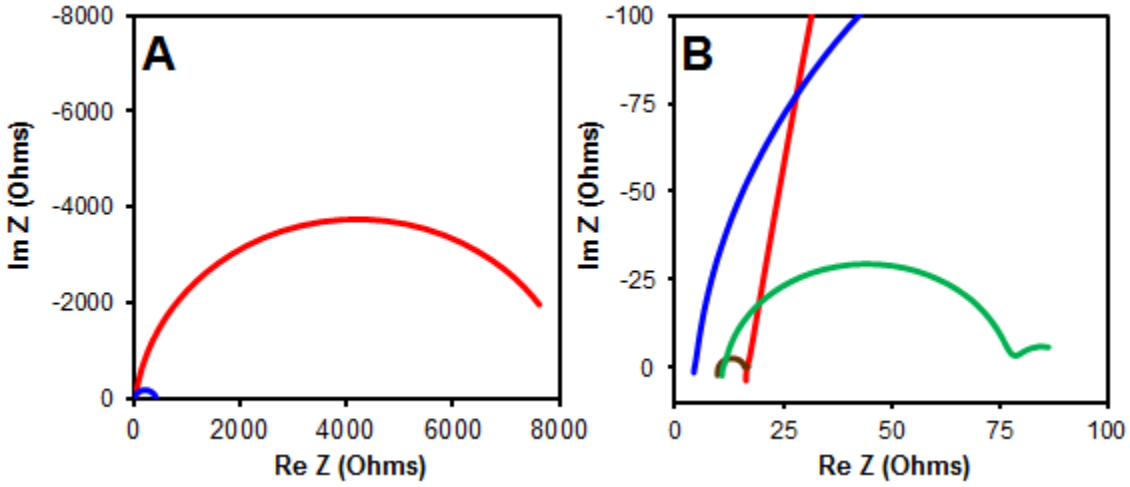

Figure 3.6. Nyquist Plots of Dark Electrodes with Different Redox Couples.
A) Nyquist plots at no applied bias for $Cu(TBP)_{4+x}(ACN)_y^{2+}/Cu(PDTO)^+$ (red), $Co(bpy)_3^{3+/2+}$ (green), and I_3^-/I^- (brown) using TD Pt electrodes and for $Cu(TBP)_{4+x}(ACN)_y^{2+}/Cu(PDTO)^+$ replacing on TD Pt electrode with an IO Pt electrode (blue). B) Enlarged depiction of the Nyquist plots in (A) to show detail for $Co(bpy)_3^{3+/2+}$ and I_3^-/I^-.

For all three redox shuttles, the Nyquist plot contained one primary arc. This arc is attributed to the charge transfer resistance (R_{CT}) at the electrode. (Recall that R_{CT} scales inversely with the rate of interfacial (electrochemical) electron transfer). A second arc for I_3^-/I^- and $Co(bpy)_3^{3+/2+}$ is observed at high resistance; this is due to the solution diffusion, which is fit to a Warburg element.[92] In the case of $Cu(TBP)_{4+x}(ACN)_y^{2+}/Cu(PDTO)^+$ with TD Pt, the diffusion element cannot be easily identified due to the exceptionally large charge-transfer resistance. Using an asymmetric setup of Figure 3.3 (i.e., one IO Pt electrode as the "working electrode" and one TD Pt electrode) with $Cu(TBP)_{4+x}(ACN)_y^{2+}/Cu(PDTO)^+$ results in the blue Nyquist plot in Figure 3.6. These plots were fit to the equivalent circuit in Figure 3.7.

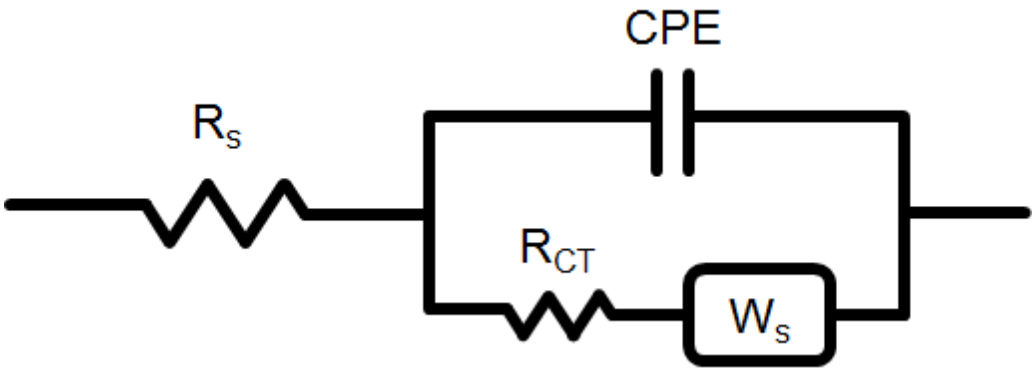

Figure 3.7. Equivalent Circuit for Fitting Nyquist Plots from Dark Electrode EIS.
The equivalent circuit use for fitting has 4 elements: R_s represents the series resistance inherent in the solution and FTO; CPE is a constant phase element, which gives the surface capacitance corrected for the non-ideality of the surface as a capacitor; R_{CT} is the resistance to charge transfer from the surface to the electrolyte; W_s is a short circuit Warburg element, which accounts for diffusion limitations.

Fits of the Nyquist plots in Figure 3.6 to the circuit in Figure 3.7 demonstrated errors of less than 10% and showed the charge transfer resistance of the $Cu(TBP)_{4+x}(ACN)_y^{2+}/Cu(PDTO)^+$ system (4400 ohms) with TD Pt to be ~1000x higher than that of I_3^-/I^- (1.5 ohms) and ~100x higher than that of $Co(bpy)_3^{3+/2+}$ (65 ohms). The charge transfer resistance at the dark electrode is inversely proportional to the rate of charge transfer; therefore, as the R_{CT} for $Cu(TBP)_{4+x}(ACN)_y^{2+}/Cu(PDTO)^+$ is ~1000x larger than I_3^-/I^-, we can estimate the rate of charge transfer to also be ~1000x slower (~70x slower than $Co(bpy)_3^{3+/2+}$). DSCs utilizing $Co(bpy)_3^{3+/2+}$ shuttle and TD Pt counter electrodes have shown diminished fill factor at full illumination,[26] suggesting that the $Cu(TBP)_{4+x}(ACN)_y^{2+}/Cu(PDTO)^+$ shuttle in an identical system will suffer from the same problem much more seriously.

Clearly, because of the high charge transfer resistance of the $Cu(TBP)_{4+x}(ACN)_y^{2+}/Cu(PDTO)^+$ on TD Pt, a different approach was required. Thus, high area IO Pt counter electrodes were employed. Utilization of an IO Pt dark electrode in one half of the

setup shown in Figure 3.3 resulted in a charge transfer resistance of 400 ohms, 10x less than that of systems using all TD Pt electrodes. IO Pt offers increased counter electrode activity (via increased surface area) without the added complications of general material applicability as discussed above. Also, because of the large apertures in this IO framework, diffusional constraints that often hamper high area architectures will not be present.[47] As described in Section 3.3.1, cyclic voltammograms (CV) of the IO Pt frameworks compared to CVs of flat ALD Pt electrodes in 2 molar H_2SO_4 (Figure 3.5) reveals a surface area increase of ~50. The deposited thickness of Pt is approximately 12 nm (by *in situ* quartz crystal microbalance), meaning that only ~5 mg of Pt is required to fully coat a 2 cm x 2 cm IO with this surface area enhancement.

3.3.3. Current-Voltage Characteristics of DSCs with Different Dark Electrodes

DSCs were fabricated using both TD Pt and IO Pt as counter electrodes with $Cu(TBP)_{4+x}(ACN)_y^{2+}/Cu(PDTO)^+$ as the redox shuttle. Photo-electrochemical measurements were performed, and the resulting current-voltage curves are shown in Figure 3.8.

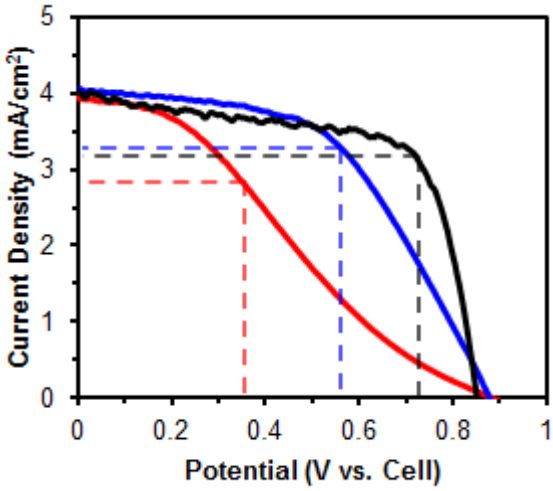

Figure 3.8. J-V Curves for DSCs Using Different Dark Electrodes
J-V curves for DSCs featuring the $Cu(TBP)_{4+x}(ACN)_y^{2+}/Cu(PDTO)^+$ redox shuttle and TD Pt dark electrode (red), IO Pt dark electrode (blue), and a Pt mesh dark electrode as part of a 3-electrode (as opposed to 2-electrode) setup (black). The dashed lines represent the maximum power points of the individual JV curves. Note that the black J-V curve was recorded under higher light intensity (see text).

The J_{sc} and V_{oc} of these devices are essentially identical when accounting for normal variations between devices. This is expected for V_{oc} as the dark electrode resistance will not be a factor when current is zero, meaning no correction for resistance is necessary. In principle, lowering the charge resistance at the dark electrode can also influence J_{sc}.[93] However, as charge transfer at the dark electrode is not the primary current limiter in this system when the photovoltage is zero, no improvement in J_{sc} is seen when switching to the IO Pt dark electrode. The current does improve at potentials between zero and V_{oc} since when both current and voltage have non-zero values, the resistance at the dark electrode becomes a factor. This affects the FF of the device and results in the curve shape seen for the TD Pt dark electrode in Figure 3.8 (red). Since IO Pt dark electrodes lower the resistance of the dark electrode via increased surface area, there is clear improvement in fill factor. This increase in fill factor (FF = 0.28 for TD Pt, 0.52 for IO Pt) leads to an 80% increase in power conversion efficiency from 1% to 1.8%. This dramatic

improvement is attributed to the IO Pt possessing ~50 times higher surface area than TD Pt, resulting in IO Pt performing as if it is a 50x faster catalyst for turning over the $Cu(TBP)_{4+x}(ACN)_y^{2+}/Cu(PDTO)^+$ redox shuttle.

A three-electrode measurement (black curve) was performed to determine the hypothetical best case scenario in terms of improving the fill factor of the system. In the presence of a reference electrode, the counter electrode can be held at any potential necessary to ensure the working electrode is at the desired potential.[94] Therefore, any current flow limitations due to the performance of the dark electrode in a two-electrode system (such as a DSC) will be absent, providing a comparison point for the improvement seen with IO Pt vs. TD Pt dark electrodes in two-electrode systems. It should be noted that the three-electrode measurement was performed under higher light intensity to obtain comparable short-circuit currents as a large diffusion resistance due to the distances in the experimental set up had to be overcome. The potential scale was also adjusted from Ag/AgCl to that of the redox shuttle used in two-electrode measurements by adjusting to the Nernstian potential of the electrolyte solution vs. Ag/AgCl. The three-electrode results show that room remains for improvement in the fill factor based on improved dark electrode performance. The simplest way to achieve this would be through further increase in the surface area of the dark electrode.

3.4. Conclusions

By using a redox shuttle having larger charge-transfer resistances at TD Pt electrodes (dark electrodes) than common shuttles such as I_3^-/I^- and $Co(bpy)_3^{3+/2+}$, the consequences of kinetically limited shuttle behavior upon DSC fill factors and overall energy conversion efficiencies can be

readily observed. A new approach to addressing this problem (i.e. slow dark-electrode kinetics and concomitant fill-factor degradation) was examined. To decrease charge-transfer resistances (increase charge-transfer rates) at the dark electrode, high area IO platinum electrodes were fabricated utilizing ALD of platinum. When used in conjunction with $Cu(TBP)_{4+x}(ACN)_y^{2+}/Cu(PDTO)^+$ as the shuttle in otherwise conventional DSCs, the IO Pt electrodes nearly doubled the fill factor and, therefore, nearly doubled the efficiency as well. Since our design principle focuses on increasing the electron-transfer rate, rather than the rate constant, the need to discover dark electrode catalysts for "problematic" shuttles is diminished. However, because this approach is rate constant independent, it may still be applied to other catalytic materials with improved rate constants for electron-transfer but lower than ideal fill-factors with "problematic" shuttles. Thus, applying our approach to a specific catalyst-shuttle system can lead to improved efficiency across many varying systems.

Chapter 4. Engendering Long-term Air and Light Stability of a TiO_2-supported Porphyrinic Dye via Atomic Layer Deposition*

*This chapter reproduced in part from Hoffeditz, W. L., Son, H.-J., Pellin, M. J., Farha, O. K., and Hupp, J. T. "Engendering Long-term Air and Light Stability of a TiO_2-supported Porphyrinic Dye via Atomic Layer Deposition", *ACS Appl. Mater. Interfaces*, **2016**, *8* (50), 34863 (DOI: 10.1021/acsami.6b10844).

4.1. Introduction and Background Information

The introduction to this dissertation mentions how DSC-type architectures have found use in photocatalytic applications in addition to simple PV applications. In this chapter, a method of protecting a porphyrin dye from oxygen degradation is discussed. While this chapter breaks from the theme of understanding and controlling deleterious electron back-transfer, it none the less demonstrates an important utility of the ALD post-treatment technique. Additionally, an intriguing in-reactor ALD quartz crystal microbalance (QCM) experiment presented here in suggests a useful method for determining dye orientation on a surface or number of ALD post-treatment cycles resulting in a completely buried dye. For these reasons, among others, this chapter is included in this dissertation.

Organic chromophores adsorbed on semiconductor surfaces have found a large degree of success as sensitizers in photoelectrochemical – both photocatalytic and photovoltaic – applications.[15, 95-98] Many of the most efficient DSCs use a porphyrin-based dye in place of more traditional ruthenium dyes,[48] and organic dyes have been shown capable of photosensitizing the catalytic reduction of water in DSC-like architectures.[99, 100] Especially relevant to their success is the modularity offered by organic dyes; numerous structures and functional groups can be combined to instill particular energetic and light harvesting properties.[17, 18, 48, 101] One particular focus of structural modifications is improving dye stability. For example, porphyrins are known to photosensitize the formation of singlet oxygen,[102] which can destructively react with the conjugated dye leading to loss of light absorption. Additionally, other organic molecules with delocalized π-electron systems are vulnerable to photo-oxidative degradation from exposure to ambient air and light.[103] These inherent instabilities have been avoided in some cases through

careful environmental isolation and in others through judicious selection of functional groups, such as replacing phenyl groups with cyano groups or changing the structural backbone of the organic dye.[99, 104] However, in some instances these structural modifications may be synthetically challenging or incompatible with adsorbing the dye to a semiconductor surface, thereby limiting their utility.

An alternative to chemically modifying the light-absorbing molecules is to protect/stabilize them after electrode-attachment—for example, via ALD of an inert, tightly enshrouding, and largely chemically impermeable coating. As mentioned before, ALD is a self-limiting materials synthesis technique that can conformally coat high-area and high-aspect-ratio surfaces with numerous metals, oxides, or sulfides with close to angstrom-scale precision. Briefly, a reactive metal-ligand complex, referred to as a metal precursor, is delivered in the vapor phase to a hydroxylated surface under inert gas flow. The metal precursor reacts only with surface hydroxo (or aqua) groups, forming a metal-ion layer that can then be further reacted with an oxygen source, typically water vapor, to regenerate the reactive hydroxo layer. Repetitive alternating exposures result in layer-by-layer growth of a metal-oxide film. When a metal oxide is deposited around a surface adsorbed dye using ALD (*i.e.* post-treatment), it can improve the stability of the dye by preventing dye desorption.[58-60, 105, 106] For example, ALD post-treatment of a simple organic dye with TiO_2 using titanium (IV) isopropoxide (TTIP) and water dramatically slowed dye desorption into a pH 10.7 ethanol solution.[59] Additionally, ALD of Al_2O_3 using trimethylaluminum (TMA) and water around a phosphonate anchored ruthenium dye slowed the rate of dye desorption 30-fold.[106] Both studies take advantage of the use of ALD to deposit a metal oxide material in interstitial spaces between dyes to block solution components, in

particular, hydroxide ions, from reaching the semiconductor surface and displacing dye anchoring groups. In yet other cases, the role of ALD or ALD-like post-treatment has been to: a) diminish organic-dye aggregation,[60] b) inhibit back electron-transfer by preventing shuttle molecules from contacting photoelectrodes,[58] or c) to block protonation of dye anchoring groups and thereby prevent desorption.[107]

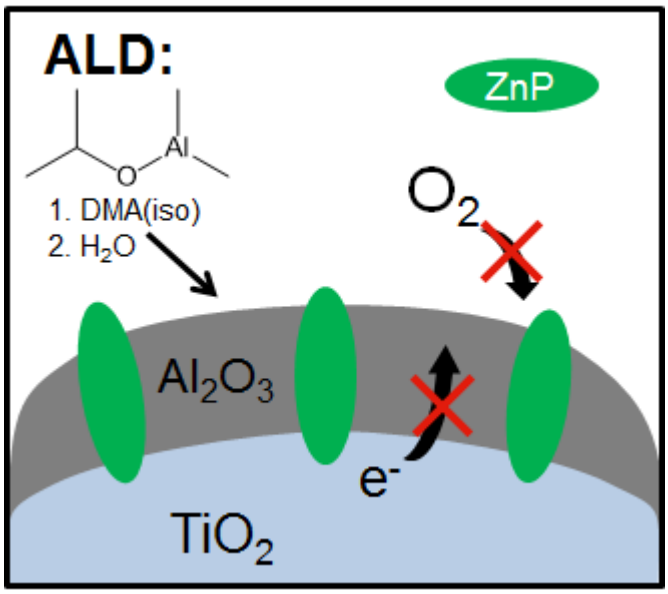

Figure 4.1. Cartoon Representation of the Effect of ALD Post-treatment.
ALD post-treatment deposits an Al_2O_3 layer only on the TiO_2, enshrouding the ZnP dye and protecting it from O_2 while also limiting electron back-transfer to a cobalt-based shuttle in solution when post-treated films are used as photoelectrodes in a DSC.

Here we apply ALD post-treatment to surface adsorbed porphyrin dye molecules to inhibit chemical and photochemical degradation. Perhaps surprisingly, we observed that porphyrinic photoelectrodes can slowly bleach even under dark conditions, if air is present. We conclude that triplet dioxygen (*i.e.* ground-state O_2) is responsible. To prevent degradation we have enshrouded dyes with alumina. To avoid damage to the dye during the enshrouding step, we have used dimethylaluminum isopropoxide (DMA(iso)) (see Figure 4.1), rather than the more

commonly used trimethylaluminum, as the chemical precursor for ALD alumina. We find that growth of Al_2O_3 around a representative zinc porphyrin dye (ZnP) leaves its light-harvesting properties untouched, but boosts its stability with respect to air, light, and/or solution exposure.

4.2. Experimental Methods and Instrumentation

4.2.1. Reagents, Solvents, and Materials

Cobalt(II) nitrate hexahydrate, 2,2'-bipyridine, ammonium hexafluorophosphate, lithium perchlorate, titanium tetraisopropoxide, trimethylaluminum, ethanol (200 proof), and acetonitrile were purchased from Sigma-Aldrich and used as received. DMA(iso) was purchased from Strem. Tetrahydrofuran (inhibited) was purchased from Fischer. TiO_2 nanoparticles (18NR-T transparent titania paste) were purchased from Dyesol. FTO glass (8 ohm resistance) was purchased from Hartford Glass (Hartford City, IN). QCM crystals were purchased from Inficon.

4.2.2. Synthesis of ZnP Dye and $Co(bpy)_3^{3+/2+}$

Porphyrin dye (ZnP) was synthesized from [5,15-bis-ethynyl-10,20-bis[2,6-di(methoxy)phenyl]porphinato]zinc (1),[108] 4-iodo-*N*,*N*-diphenylbenzenamine (2),[109] and 2-cyano-3-(4-iodophenyl)acrylic acid (3),[110] which were synthesized according to literature procedures.

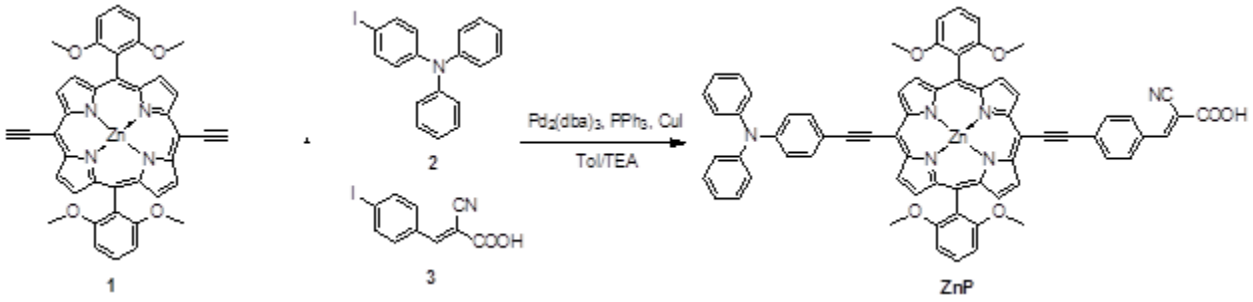

Scheme 4.1. Synthesis of the Zinc porphyrin molecule (ZnP).
ZnP as prepared by Prof. Ho-Jin Son (currently at Korea University).

ZnP was further verified by NMR and mass spectroscopy. ^{1}H NMR (300 MHz, DMF-d_7) δ 9.70 (dd, J = 13.64, 4.56 Hz, 4H), 8.77 (dd, J = 8.61, 4.43 Hz, 4H), 8.41–8.29 (m, 2H), 8.25–8.20 (m, 2H), 8.12–7.99 (m, 2H), 7.90–7.80 (m, 2H), 7.50–7.43 (m, 4H), 7.30–7.18 (m, 12H), 6.98 (s, 1H), 3.69–3.51 (m, 12H). MS (MALDI-TOF) m/z = 1106.21 ([M], 85%). Trisbipyridine cobalt(III/II) hexafluorophosphate was synthesized as described in Chapter 2 of this dissertation in Section 2.2.3.

4.2.3. Fabrication and Dye Loading of TiO_2 Nanoparticulate Films

Nanoparticulate TiO_2 films were deposited on 1.5 cm x 2 cm cut FTO coated glass that had been sonicated successively in water/detergent, acetone, and isopropanol before being dried by N_2 flow. The TiO_2 nanoparticles were diluted 1:1.5 by mass with absolute ethanol. Spin coating (Laurell WS-650Mz-23NPPB) this solution on the FTO at 4000 RPM for 30 seconds, followed by sintering at 450 °C (3 hour ramp up, 30 min hold), resulted in nanoparticulate films of ~1 µM thickness as measured by profilometry (Veeco Dektak 150). A razor blade was used to cut TiO_2 nanoparticle films to the desired size. The same procedure was followed in experiments where a TiO_2 blocking layer was utilized, except the initial FTO was coated with a dense TiO_2 layer via

ALD (see section 2.2.10) before spin coating. The ZnP dye was dissolved in THF (0.05 mM). The TiO_2 films were immersed in this solution overnight. Following dye loading, the dyed films were soaked in a solution of clean THF for ~15 minutes to eliminate any physisorbed ZnP. The films were then rinsed with THF followed by ACN before drying under N_2 flow.

4.2.4. Atomic Layer Deposition and in-Reactor QCM

The aluminum ALD precursors were trimethylaluminum (TMA) and dimethylaluminum isopropoxide (DMAiso). ALD was performed with an Ultratech/Cambridge Nanotech Savannah 100 reactor with DMA(iso) and water as the aluminum and oxygen source, respectively. The reaction chamber was heated at 110 °C for all ALD experiments, including the TMA exposures where no ALD growth took place. The DMA(iso) precursor reservoir was heated at 80 °C. Alternating pulses of DMA(iso) and water (0.05 s pulse, 10 s expo, 30 s nitrogen purge) resulted in Al_2O_3 growth. The growth rate observed on a silicon witness chip, as measured by ellipsometry (J.A. Woollam M2000 model), was ~1 Å per cycle. TiO_2 blocking layers were fabricated as described in Section 2.2.10. In-reactor quartz crystal microbalance (QCM) measurements were performed on an Ultratech/Cambridge Nanotech Savannah 200 reactor equipped with a wall mounted QCM apparatus.[111]

4.2.5. UV-Vis Spectroscopy and ZnP Film Degradation

UV-Vis absorption measurements were performed on dye-loaded, TiO_2 nanoparticle films using a Cary-5000 NIR/Vis/UV spectrophotometer. A mask was employed and each film was measured in triplicate to mitigate inconsistencies that may arise from different placement of the film in relation to the light source/detector of the instrument. ZnP films were aged either under

an inert argon atmosphere or in ambient lab atmosphere. Films were either aged in the dark, via either wrapping in aluminum foil or storing in light-free cabinet, or in the light, in which case they were left on a benchtop or uncovered in the Ar box. Accelerated solution degradation utilized sealed microwave vials in which the film was immerse in methanol. This methanol solution was purged with N_2 or O_2 for 20 minutes before illumination. Illumination was performed with a white light LED.

4.2.6. SEM/EDS

SEM/EDS was performed by Aaron Peters using the Hitachi SU8030 in the EPIC facility of NUANCE.

4.2.7. Photoelectrochemical Measurements

Photoelectrochemical measurements were performed on a Solartron Analytical Modulab box with a 1 MS/s potentiostat module. Measurements were performed with the traditional 2-electrode "sandwich" devices. The redox electrolyte was 0.2 M *tris*-(2,2'-bipyridine)cobalt(II) hexafluorophosphate ($Co(bpy)_3^{2+}$) and 0.02 M *tris*-(2,2'-bipyridine)cobalt(III) hexafluorophosphate ($Co(bpy)_3^{3+}$) in acetonitrile with 0.1 M lithium perchlorate. The counter electrode was Pt from the thermal decomposition of H_2PtCl_6. The light source was a xenon-arc lamp, the output of which was passed through an AM (air mass) 1.5 filter with as light intensity of ~1 sun.

4.3. Results and Discussion

4.3.1. Dye Stability to TMA and DMA(iso)

To first establish the stability of the ZnP toward the two aluminum precursors, the TiO_2-bound dye was exposed to repeated pulsing in the ALD reaction chamber with either vapor-phase DMA(iso) or vapor-phase TMA. The effects of these treatments on the light absorption by the dye are illustrated in Figure 4.2.

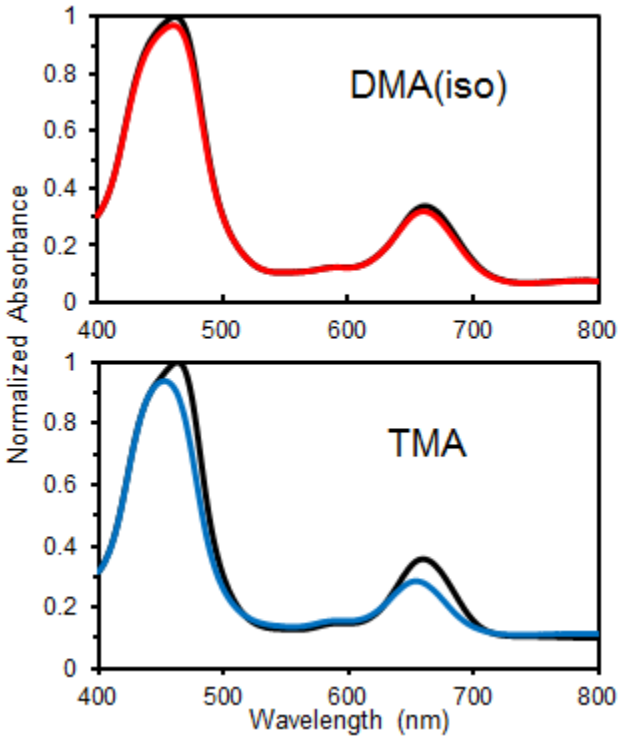

Figure 4.2. UV-Vis of ZnP on TiO_2 Before and After Exposure to DMA(iso) and TMA. The normalized absorbance of ZnP on a TiO_2 film before (black) and after exposure to 30 pulses of DMA(iso) (top, red) and TMA (bottom, blue). The absorbance of each spectrum is normalized to the maximum absorbance of the separate pre-exposure ZnP films.

TMA significantly degrades the dye's absorbance, whereas DMA(iso) does not. Note that because steam is not introduced into the ALD reaction chamber at any point, no Al_2O_3 film is

being grown in Figure 4.2. Thus, we attribute any change in absorbance to the interaction of the dye with the vapor phase TMA or DMA(iso) and not a change in the local environment of the dye.[58, 59] Why exposure to TMA results in a degradative change in absorbance for ZnP is unclear but still under investigation. As it stands, this observation is an empirical one only. Regardless, the observed degradation of ZnP on exposure to TMA lead us to use only DMA(iso) for subsequent alumina-enshrouding of electrode-adsorbed dye molecules.

4.3.2. Quartz Crystal Microbalance Measurements of ALD Growth around ZnP

Conventional ALD processes involve nucleation and growth of a film on a continuous substrate that is terminated with hydroxyls. In the system examined here, surface-adsorbed ZnP non-uniformly blocks access of the ALD precursor to the underlying, potentially reactive, surface hydroxyl groups. Thus, reactive groups sited directly beneath a dye should be largely inaccessible, while those between dyes may react. Under these conditions, an island growth motif is anticipated, rather than conventional film growth.[112, 113] Island growth should persist exclusively in the z-direction (*i.e.* normal to the underlying metal-oxide support) until the thickness of the islands matches the height of the surrounding dye molecules. Beyond this point, islands will begin to bury the dye molecules, while also merging with each other; see Figure 4.3.

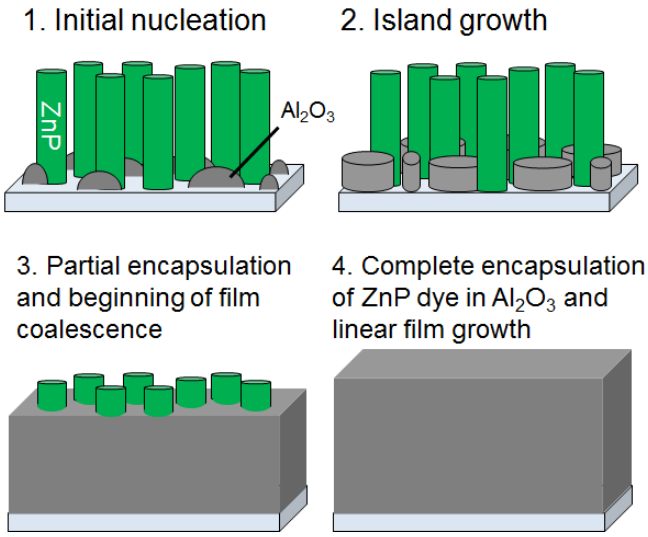

Figure 4.3. Schematic Representation of Island Growth and Nucleation
The DMA(iso) precursor can only deposit on available hydroxyl or water sites on the surface, resulting in the dye acting as a quasi-surface mask. After this initial nucleation, the Al_2O_3 layer grows in islands, eventually coalescing into a film and then complete encapsulating the ZnP.

Further film growth should then follow that expected for a continuous substrate. Note that because a larger fraction of the surface becomes available for film growth in the continuous-surface regime versus in the island or perforated-surface regime, a significant increase in film gravimetric growth rate should accompany the transition to the continuous-surface regime.

To test this notion, deposition of Al_2O_3 around adsorbed ZnP dye molecules was tracked using in-reactor QCM.[111] By adsorbing the dye to an Al_2O_3 coated QCM crystal, we can observe a mass gain as Al_2O_3 is deposited around the dye. As shown in Figure 4.4, *in the absence of dye* alumina growth from DMA(iso) vapor (A half-cycle) and steam (B half-cycle) is nearly ideal. Film growth is immediate and nearly linear with the number of AB cycles.

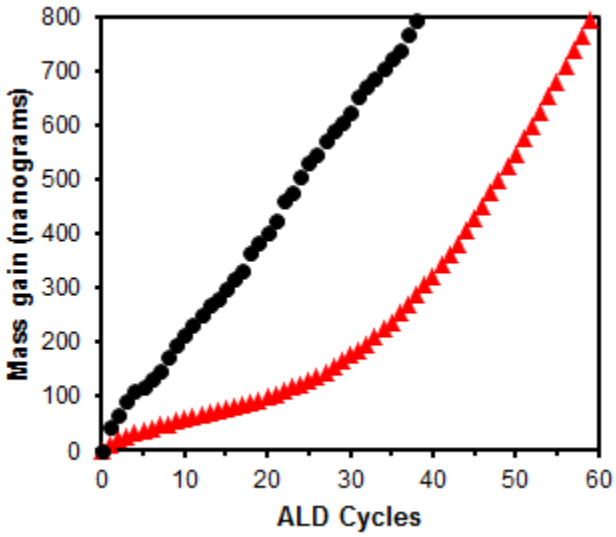

Figure 4.4. QCM Traces for Al_2O_3 Deposition with and without Adsorbed ZnP.
QCM trace of Al_2O_3 grown from DMA(iso) and water on an Al_2O_3 coated QCM crystal (black circles) and an Al_2O_3 coated QCM crystal dye loaded with ZnP dye (red triangles).

The mass gain measured by QCM can be converted to a film growth rate via the surface area of the QCM crystal and the density of the grown material. In this case, the density of alumina is assumed to be 3.95 g/cm^3, resulting in a growth rate of ~0.5 Å per AB cycle. Note that this value is significantly smaller than the 1.0 Å per cycle rate generally measured on flat silicon wafers when growth is tracked by ellipsometry for deposition on highly porous TiO_2 nanoparticle electrodes. The growth rate difference observed between the QCM deposition (~0.5 Å) shown in Figure 4.4 and the 1 Å per cycle rate measured by ellipsometry for the typical ALD process used to coat highly porous electrodes is a direct result of the different exposure times used in the depositions; the QCM trace in Figure 4.4 for no dye present does not have any exposure time. Subsequent QCM experiments with long exposure times on undyed surfaces resulted in the ~1 Å growth rate observed by ellipsometry on flat Si. Post-treatment QCM experiments performed around a bodipy-based dye (which is not discussed here but commented on to demonstrate the

utility of this technique) using long exposure times still resulted in the same island growth/film coalescence QCM growth profile, with film coalescence occurring at the predicted ALD cycle number based on the dye structure and our observations with ZnP. Regardless, the observed pattern of growth is typical of that for films that achieve uniform surface coverage. This mass gain profile can be compared to the mass gain profile of a non-dye loaded crystal to examine the ALD growth morphology. In this way, the effect of the dye on the ALD process can be interrogated in real time.

As illustrated by the red triangles in Figure 4.4, the growth profile for alumina *in the presence of surface-adsorbed ZnP dye* is distinctly different. The initial rate of growth, as indicated by the mass gain, is only about one-third as fast as in the dye's absence. Qualitatively, as the dye molecules block access of the film precursors to some fraction of the underlying support (*i.e.* alumina-coated gold on quartz), the actual rate of growth of the Al_2O_3 film normal to the surface around the dye should be similar but appears different due to QCM measuring mass gain/unit area only. Beyond about 20 AB growth cycles, however, the rate of mass increase (*i.e.* alumina film growth) begins to increase and eventually demonstrates the linear growth observed for alumina on the dye-free surface.

The observed biphasic-like growth profile is suggestive of island growth from isolated nucleation sites followed by film coalescence.[112, 113] In this picture (Figure 4.3), the dye acts as a surface mask, limiting the sites at which DMA(iso) can react. Al_2O_3 then grows vertically (only) from these isolated sites. The dye-perforated Al_2O_3 film eventually grows beyond the dye, and coalesces into a continuous coating similar to that obtained from the outset on a dye-free surface. At this point, the Al_2O_3 growth rate on the dye-loaded platform should closely match the growth

rate on the platform that lacks dye. Experimentally, as evidenced by the red QCM trace in Figure 4.4, island coalescence appears to start somewhere beyond the 20th AB cycle and is complete by the 40th AB cycle. Thus, after 30 AB cycles, coalescence should be well under way, the alumina layer thickness should be about the same as the distance the dye molecules extend from the electrode surface, but the dyes should not be completely covered over yet by the inert metal-oxide film. Since our objective is to protect the dye, but leave it capable still of communicating with solution species in a photo-electrochemical cell or photocatalytic system, we settled on 30 AB growth cycles for all subsequent experiments.

4.3.3. SEM/EDS of ALD Post-Treated ZnP Films

The in-reactor QCM data provide valuable information about Al_2O_3 growth around the dye on a flat surface, but do not prove that similar growth occurs with high-area, TiO_2-nanoparticle-based films. Scanning electron microscopy (SEM) and energy-dispersive X-ray spectroscopy (EDS) were employed to investigate this second question. An important procedural distinction between ALD performed on QCM crystals versus nanoparticle films turns out to be the use of longer vapor exposure times for the latter. Deposition in "exposure mode" involves increasing the time the reactive vapor (DMA(iso) or water) is held in the reaction chamber before the chamber is intentionally evacuated. Using the ALD tool in this manner ensures sufficient time for the precursor to diffuse through and deposit on high surface area structures.[114] Figure 4.5 shows EDS and SEM data for a TiO_2 nanoparticle film deposited on FTO-coated glass, where the film was first loaded with ZnP (by adsorption from solution) and then subjected to 30 AB growth cycles (~3 nm) of Al_2O_3. The data show that Al is indeed distributed throughout the nanoparticulate TiO_2 network.

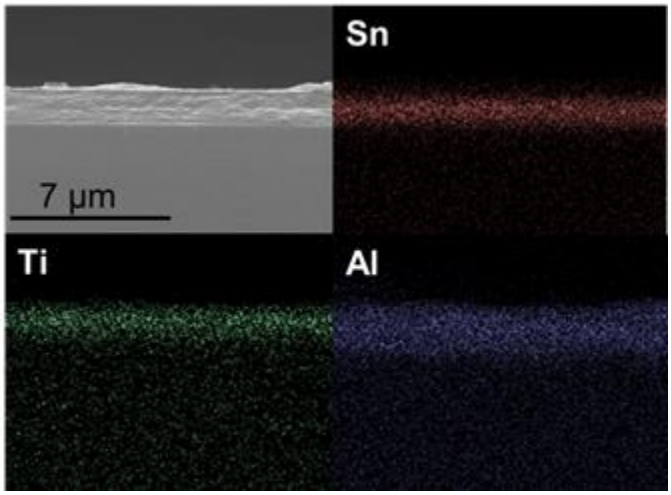

Figure 4.5. SEM/EDS of ZnP on TiO_2 Nanoparticles with Al_2O_3 ALD Post-treatment. Scanning electron microscopy and Energy-dispersive X-ray spectroscopy (SEM/EDS) images of a ZnP dye loaded TiO_2 nanoparticulate film post-treated with alumina grown with the DMA(iso) precursor.

That the apparent thickness of aluminum on the film is greater than that of Ti is attributed to the deposition of Al_2O_3 on the roughened surface of FTO. Ti, contrarily, will only be found in the nanoparticulate network (no dense TiO_2 blocking layer is present with these films), which will not conformally coat the rough FTO surface in the same way ALD can.

4.3.4. Dye Survival with and without Post-treatment under Various Conditions

Figure 4.6 presents the results of visible-region absorption experiments designed to gauge the extent to which air and/or room light bleach ZnP, as well as the extent to which ALD enshrouding with alumina (30 AB cycles) imparts resistance to degradation. Optical monitoring was done at the maximum absorbance of the Soret band for dye-adsorbed TiO_2. Under an Ar atmosphere (Figure 4.6 A, B), regardless of whether the film is stored in ambient light or in the dark, no degradation in optical absorbance is observed; nor is this stability influenced by alumina encapsulation. In air, however, ZnP on untreated nanoparticulate TiO_2 bleaches significantly with time, even when protected from exposure to light. Indeed, 50% of the absorbance is lost

within about twenty days. When alumina enshrouded, however, the dye is only marginally bleached, *e.g.* only a few percent over a period of thirty days; see Figure 4.6-C. We infer that oxidative degradation of ZnP (by ground-state oxygen) is occurring in the absence of alumina, but that in the presence of ALD alumina O_2 is physically excluded from contact with dye molecules, or at least with portions that are otherwise susceptible to degradation.

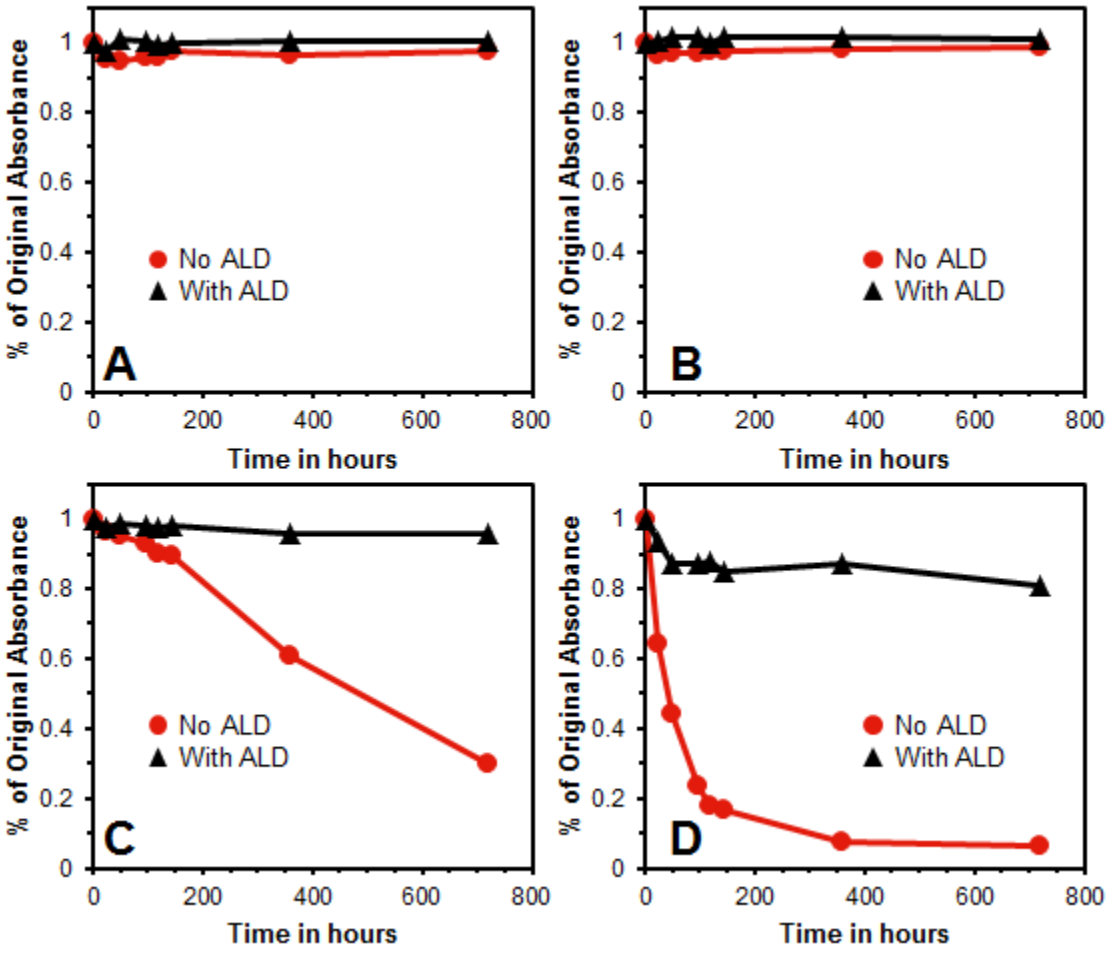

Figure 4.6. Change in ZnP Soret-band Absorbance with and without ALD Post-treatment with Different Aging Conditions
Percent of original absorbance of the ZnP dye Soret band, with (black triangles) and without (red circles) ALD Al_2O_3, stored (A) in an Ar atmosphere in the dark; (B) in Ar atmosphere, in the light; (C) in air, in the dark; and (D) in air, in ambient light.

Figure 4.6-D presents results for a similar set of aging experiments in air, but now also with exposure to ambient light. In the absence of ALD alumina, the dye is ~50% bleached in 48 hours. The accelerated degradation is likely due to attack of ZnP by singlet molecular oxygen, which is generated from ground-state O_2 by photosensitization with ZnP.[102] In sharp contrast, the alumina-enshrouded dye is largely immune to bleaching, apart from a *ca.* 12% bleach in the first 48 hours. The initial degradation evident in Figure 4.6-D may speak to some non-uniformity in the adsorption of ZnP – for example, slight aggregation – and, therefore, ineffective enshrouding with ALD alumina. Nevertheless, ALD Al_2O_3 dramatically improves the stability of ZnP in ambient light and air, allowing the dye to retain ~80% of its initial Soret band absorbance over a period of ~1 month.

Of particular interest for photocatalytic applications, a similar trend is observed when dye loaded films are illuminated in O_2-rich methanol as shown in Figure 4.7.

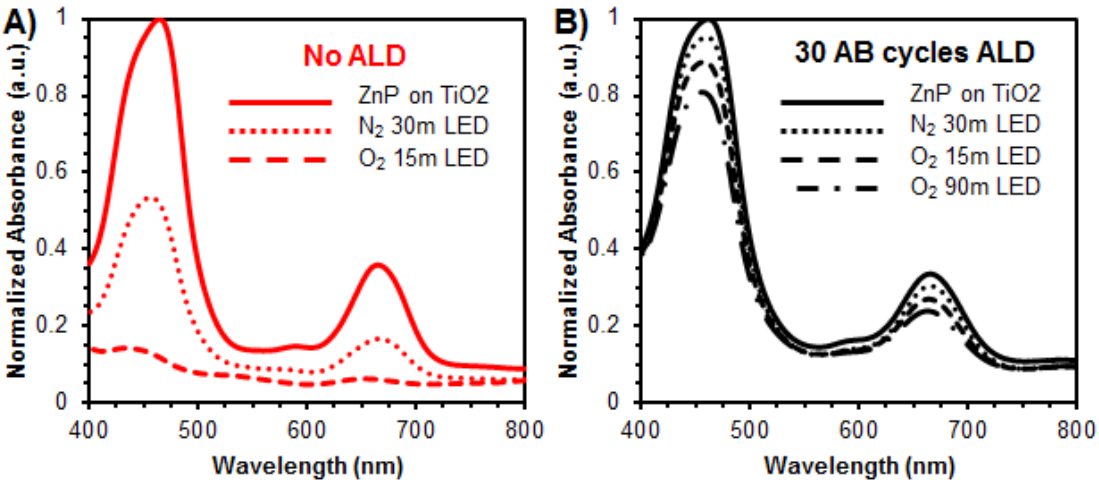

Figure 4.7. UV-Vis of ZnP on TiO_2 with and without ALD Post-treatment Illuminated in O_2-rich Methanol.
Normalized absorbance of a set of ZnP on TiO_2 films without (A) and with (B) 30 AB cycles of ALD post-treatment Al_2O_3 from DMA(iso) and water. The films were illuminated with a white LED. The methanol solution was purged with the stated gas for 20 minutes before each measurement. The times given in the legend refer to the amount of time under illumination after purging with gas.

The degradation of untreated ZnP under intense illumination in an ostensibly N_2 environment suggests light alone can degrade the ZnP to a degree, but the slight shift in location of the absorbance maxima after illumination in the presence of O_2 denotes oxygen also plays a roll. However, no such shifts are observed, whether under an N_2 or O_2 environment, when ALD post-treatment is employed. Some decrease in overall absorbance is observed, but to a much smaller degree than when post-treatment is absent and over a significantly longer period of time under these conditions, which are significantly harsher than those employed in Figure 4.6. This promising results points to the utility of this technique for improving dye stability under constant illumination conditions in the presence of increased concentrations of oxygen, such as those that might be found for an operating dye-sensitized water splitting cell.

In addition to increased air and light stability, ALD of Al_2O_3 around the ZnP dye imparts stability against desorption into mildly basic solutions. Figure 4.8 shows the absorbance of ZnP dye loaded TiO_2 films with and without ALD Al_2O_3 before and after 24 hours of submersion in the dark in pH ~10 solution (measured by pH meter).

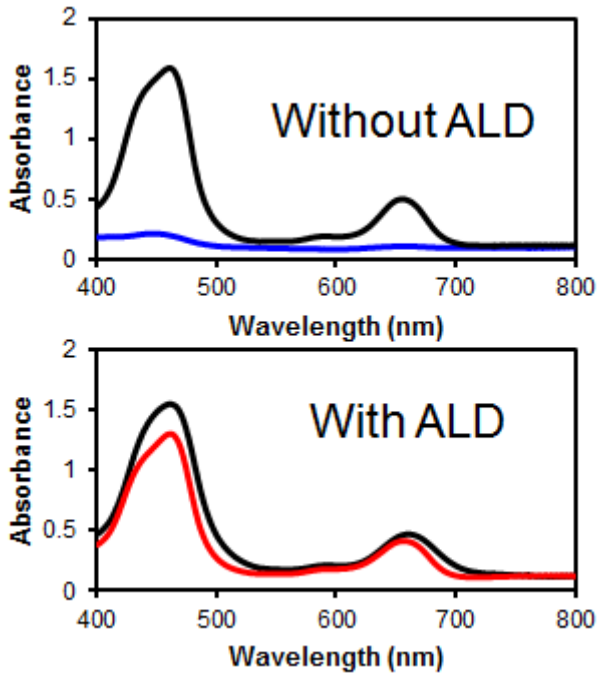

Figure 4.8. UV-Vis of ZnP on TiO_2 with and without ALD Post-treatment After Exposure to Mild Alkaline Solution.
Absorbance of ZnP dye loaded TiO_2 films before (black) and after (blue/red) 24 hours of soaking in tetrahydrofuran at pH ~10 (by pH meter). With 30 AB cycles of Al_2O_3 post-treatment, nearly 85% of the original absorbance is retained.

With no ALD protection, the dye is nearly completely desorbed, whereas the ALD protected dye retains ~85% of its original absorbance – consistent with the idea that a small population of aggregated or otherwise poorly bound dye is initially present. As previously discussed for other dyes, the resistance to desorption in nonaqueous base is presumably due to protection of the alumina-buried dye anchoring group (phenyl-carboxylate) from substitution and displacement at

the TiO_2 surface by hydroxide ion.[106, 115] It should be noted that, while the result would seem to point toward applications for water oxidation reactions typically done in aqueous alkaline conditions, Al_2O_3 is not long-term stable to base. Therefore, after ~50 hours the Al_2O_3 film cementing the dye in place has been degraded and dye desorption still occurs. However, this does not preclude the use of Al_2O_3 post treatment for water splitting in mild alkaline or non-alkaline medium.

4.3.5. Photovoltaic Behavior of ALD Post-treated Devices

The retention of light harvesting capabilities over time is an important characteristic of ALD-treated ZnP films but, for applications such as DSCs or photocatalysis, the dye must also be in electronic contact with both the TiO_2 film and an electrolyte solution. To verify preservation of electron injection and dye regeneration capabilities, DSC devices were constructed using post-treated ZnP loaded TiO_2 films (30 AB cycles ALD Al_2O_3) with the $Co(bpy)_3^{3+/2+}$ redox shuttle. The resulting current density-voltage (J-V) plots are shown in Figure 4.9.

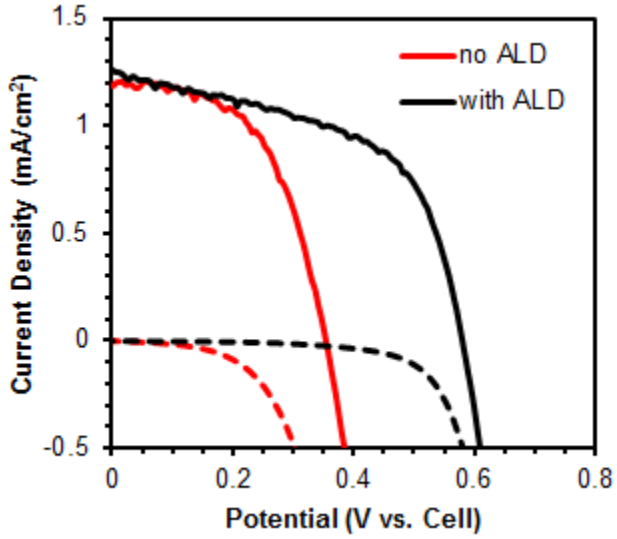

Figure 4.9. J-V Curves for ZnP on TiO_2 with $Co(bpy)_3^{3+/2+}$ Shuttle and ALD Post-treatment. J-V curves for ZnP dye on TiO_2 nanoparticles with $Co(bpy)_3^{3+/2+}$ electrolyte under illumination (solid lines) and in the dark (dashed lines) with (black) and without (red) 30 AB cycles of Al_2O_3 ALD post-treatment from DMA(iso) and water.

Both non ALD post-treated and ALD post-treated films demonstrate approximately 1.2 mA/cm^2 current density, verifying the ability of the ALD post-treated dye to both charge inject and be regenerated by the redox shuttle. Furthermore, the Al_2O_3 post treatment process results in dramatic improvement in the device voltage, increasing the open circuit voltage (V_{oc}) of the device by ~0.2 V. It should be noted here that the devices in Figure 4.9 perform significantly worse than other DSCs utilizing the $Co(bpy)_3^{3+/2+}$ shuttle with porphyrin dyes. However, the observed device performance is not unreasonable given the thin TiO_2 electrodes used and the lack of a light scattering layer. The large increase in V_{oc} is likely due to a) the suppression of deleterious back electron transfer due to more complete isolation of the redox shuttle from the underlying electrode[58, 105, 116] and/or b) passivation of surface states that may otherwise facilitate back electron transfer.[29, 117] Open circuit voltage decay measurements in Figure 4.10, which are a measurement of the average survival time of an electron in the TiO_2 conduction band, and the

dark J-V curves in Figure 4.9 both support either mechanism(s) of slowed electron interception, a result anticipated based on the insulating nature of Al_2O_3.

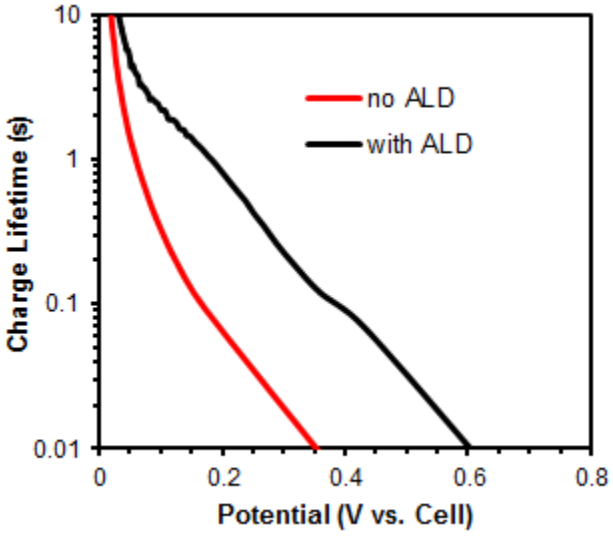

Figure 4.10. OCVD of ZnP on TiO_2 with $Co(bpy)_3^{3+/2+}$ shuttle and ALD Post-treatment. Open circuit voltage decay (OCVD) plot for DSC devices without (red) and with (black) Al_2O_3 ALD post-treatment.

Deposition of thin (~3 Å) layers of Al_2O_3 on non-dyed TiO_2 has been shown to slow electron interception while having little effect on the location of the TiO_2 conduction band for both flat TiO_2 and nanoparticulate TiO_2 films.[52, 53] Despite utilizing a 10X thicker Al_2O_3 layer, we expect the same negligible effect on TiO_2 conduction band for our system, especially considering that post-dye adsorption ALD deposits Al_2O_3 only where dye is not already present. Regardless, the existence of ~1.2 mA/cm^2 photocurrent for post-treated devices confirms electronic contact between the dye and both the underlying semiconductor and the redox species in solution and approximately equal charge injection efficiency to ALD-PT free systems.

4.4. Conclusions

When stored in air, dry ZnP-based photoelectrodes are significantly damaged (bleached) in a matter of days by triplet O_2, even under dark conditions, and in a matter of hours by singlet O_2 when also exposed to ambient lab light, where singlet O_2 formation appears to be sensitized by photo-excitation of ZnP. Protection from singlet O_2 is especially useful in dye-sensitized oxygen evolution, where large quantities of O_2 will be present near the electrode surface. These observations point to the potential benefit of enshrouding, but not burying, the electrode-adsorbed dye molecules with a protective and inert layer of alumina only several angstroms thick. We find that DMA(iso) is a particularly effective molecular precursor for ALD growth of the desired alumina coatings. The precursor is effective for dyes (photo-sensitizers) adsorbed on both flat and high-area photoelectrodes (for example, nanoparticulate films of TiO_2). In contrast to the oft-used alumina precursor TMA, DMA(iso) allows for Al_2O_3 growth without significant degradation of the dye. The milder deposition conditions characteristic of DMA(iso) may permit protective alumina enshrouding of a wide variety of highly engineered dyes without endangering their intended functionality.

"In-reactor" QCM monitoring of alumina deposition on ZnP-coated TiO_2 electrodes reveals a pattern consistent with island growth followed by merging of islands. Merging is possible once islands are tall enough to overcoat adsorbed dyes – roughly 3 nm for ZnP. Stopping just short of island merger leaves the dyes well protected from O_2 under both dark and light conditions. To the extent that island-like metal-oxide growth behavior is observed with other dye/electrode combinations, QCM monitoring should be effective for determining the optimal number of growth cycles, *i.e.* a sufficient number to isolate most of an adsorbed dye from chemical

interaction with oxygen, but not so large as to isolate the dye from chemical contact with an electrolyte solution. Notably, the QCM approach does not require independent knowledge of the metal-oxide growth rate or the thickness of an adsorbed dye monolayer.

Returning to ZnP/TiO_2, we find that ALD-alumina enshrouding boosts the J-V performance, specifically the V_{oc}, when the assembly is used as a photoelectrode in a liquid-junction solar cell containing $Co(bpy)_3^{3+/2+}$ as the redox shuttle. As Al_2O_3 itself is not conductive, ALD-based post-treatment of electrodes likely selectively slows the rate of undesired back transfer of a dye-injected charge from a sensitized photoelectrode to a molecular shuttle, a molecular catalyst, or a solid-state charge carrier, thereby improving the efficiency of corresponding photoelectrochemical and hybrid solar cells. ALD post-treatment also increases the longevity of the dye in the particularly harsh conditions, *i.e.*, constant directed LED illumination and high local concentrations of oxygen, that may be present in photocatalytic water splitting.

Finally, we suggest that enshrouding may prove useful with other redox shuttles. In particular, it may eliminate association between triiodide and highly polarizable dyes – a phenomenon that results in larger dark currents and smaller photovoltages than otherwise expected. Enshrouding may also prove effective for stabilizing alkyne- and alkene-containing dyes against chemical degradation (attack by photo-generated bromine atoms) when bromide/tribromide is used as a redox shuttle.[118] With the right choice of dye, cells containing the bromide/tribromide shuttle can deliver significantly higher photovoltages than can most other shuttles;[43, 118, 119] but, the aforementioned bromination chemistry has limited its evaluation. While investigations with iodide/triodide and bromide/tribromide would be intriguing, we have yet to follow-up experimentally with either.

Chapter 5. Electron Superexchange through Surface-adsorbed Dyes as a Pathway for Electron Interception in Dye-sensitized Solar Cells

5.1. Introduction and Background Information

As was discussed in the introduction to this dissertation, electron interception is one of the most detrimental processes to DSC performance, and slowing this process, be it through modifications to the shuttle, the photoelectrode, or the dye, has been the subject of much of the innovation in DSCs.[119-123] Modifications to the photoelectrode (*i.e.*, the dye-loaded TiO_2 nanoparticulate electrode), specifically coating the TiO_2 with a more insulating material, are an intriguing strategy to slow interception from the TiO_2 CB. Typically metal oxides, these insulating overlayers are interesting in that they create a *direct* barrier to electron transfer, as opposed to relying on some intrinsic molecular property.[29, 54, 124] If this coating process is performed before dye-adsorption, electron interception is indeed dramatically reduced, but so is charge injection; the insulating overlayers create a barrier in both directions, and the insulating material can slow charge injection from surface adsorbed dyes to the point where current losses due to inefficient injection become cannot be overcome.[30, 125]

To circumnavigate the injection problem present with insulating metal oxide overlayers on TiO_2, the insulating layer can instead be added via a post-treatment method, *i.e.*, added *after* dye adsorption. Thus, the dye remains in direct contact with the TiO_2 semiconductor, allowing for continued efficient charge injection, while electron interception from exposed TiO_2 is limited by the deposition of the insulating metal oxide. While post-treatment precludes certain deposition techniques, ALD, with its numerous possible deposition materials, precisely controllable film thickness, and ability to uniformly coat high aspect ratio surfaces, is ideally suited for the post-treatment technique.[7, 58, 60] Chapter 4 of this dissertation described this atomic layer deposition post-treatment (ALD-PT) method in detail as it was applied to a porphyrin-based dye to protect

said dye from degradation. In this chapter, the same ALD-PT technique utilizing Al_2O_3 deposition is applied to the same ZnP porphyrin dye, but the system is instead used to study electron interception dynamics in DSCs.

As mentioned above, ALD-PT offers the potential to slow electron interception (and thus increase obtainable open circuit voltages) without inhibiting charge injection. In fact, when ALD-PT was applied to a simple organic dye on TiO_2 using SiO_2 as the insulating material, V_{oc} was indeed increased (as was photocurrent).[58] However, despite SiO_2 being a highly insulating material, the obtained increase in V_{oc} was modest at best, amounting to less than 75 mV even under optimized conditions. Moreover, the reported V_{oc} of 0.69 V with I_3^-/I^- was well below the theoretical V_{oc} possible with said shuttle.[58] Highly insulating materials such as SiO_2 in the thickness reported would be expected to almost completely eliminate electron interception from TiO_2.[29] While it is tempting to blame I_2-dye adducts for the less than ideal voltage,[126] recall both that the dye is encapsulated with SiO_2 (which limits the accessibility of any iodide species to the dye) and that, if dye excited state quenching by I_2 type species was the primary culprit, we would expect similar limitations with ruthenium dye N719, the PCE record holder for iodide-based shuttles. Thus, it was hypothesized that the dye was somehow facilitating electron interception by the redox shuttle, potentially through a superexchange-like mechanism.

Charge hopping, charge tunneling, and superexchange are well studied phenomena in donor-bridge-acceptor type organic molecules.[127-130] Aside from the inclusion of a “bridge”, these molecules often have significant common traits with the organic dyes used in DSCs and DSC-like devices, and it is therefore likely that one of the above ET processes is a pathway for interception in these DSC systems. Unfortunately, the various competitive charge transfer

processes in typical DSCs convolute any contribution to charge interception from these superexchange-like processes, making them difficult to interrogate. In this chapter, the ALD-PT technique described in Chapter 4 is used to deposit insulating Al_2O_3 around a porphyrin dye on TiO_2 nanoparticles, isolating the TiO_2 from the surrounding redox electrolyte in such a way that the dye serves as the "path of least resistance" for electron interception. Thus, by comparing the rates of deleterious dark electron transfer processes to a cobalt-based molecular redox shuttle from TiO_2 coated by Al_2O_3 (both with surface adsorbed dye and without), the dye contribution to electron interception can be interrogated. We consequently find that the dye-loaded ALD-PT films demonstrate very small ALD-PT thickness dependence (*i.e.*, electron transfer distance dependence) compared to dye-free ALD-PT films. We tentatively ascribe this difference to dye-mediated electron superexchange from the TiO_2 to a cobalt shuttle molecule in solution.

5.2. Experimental Methods and Instrumentation

Because both Chapter 4 and this chapter work with the same TiO_2—dye—ALD-PT system, many of the experimental details for this chapter are identical to those found in Chapter 4. They are presented here again, with the necessary minor modifications, for both simplicity and clarity. Additionally, it should be noted that much of the basic characterization, such as stability toward the ALD precursor DMA(iso) and SEM/EDS verifying Al_2O_3 coating of the mesoporous network, are outline in Sections 4.3.1 and 4.3.3, respectively, and thus are not discussed further here.

5.2.1. Reagents, Solvents, and Materials

Cobalt(II) nitrate hexahydrate, 2,2'-bipyridine, 4,4'-di-*tert*-butyl-2,2'-bipyridine, ammonium hexafluorophosphate, lithium perchlorate, titanium tetraisopropoxide, ethanol (200 proof), and acetonitrile were purchased from Sigma-Aldrich and used as received. DMA(iso) was purchased from Strem. Tetrahydrofuran (inhibited) was purchased from Fischer. TiO_2 nanoparticles (18NR-T transparent titania paste) were purchased from Dyesol. FTO glass (8 ohm resistance) was purchased from Hartford Glass (Hartford City, IN).

5.2.2. Synthesis of ZnP Dye and $Co(bpy)_3^{3+/2+}$, and $Co(di\text{-}t\text{-}butylbpy)_3^{3+/2+}$

Porphyrin dye (ZnP) was synthesized from [5,15-bis-ethynyl-10,20-bis[2,6-di(methoxy)phenyl]porphinato]zinc (1),[108] 4-iodo-*N*,*N*-diphenylbenzenamine (2),[109] and 2-cyano-3-(4-iodophenyl)acrylic acid (3),[110] which were synthesized according to literature procedures.

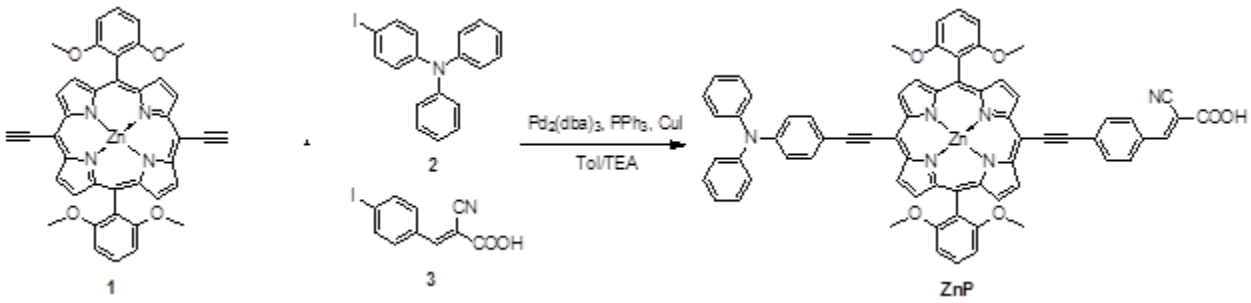

Scheme 5.1. Synthesis of the Zinc porphyrin molecule (ZnP).
ZnP as prepared by Prof. Ho-Jin Son (currently at Korea University).

ZnP was further verified by NMR and mass spectroscopy. ^{1}H NMR (300 MHz, DMF-d_7) δ 9.70 (dd, J = 13.64, 4.56 Hz, 4H), 8.77 (dd, J = 8.61, 4.43 Hz, 4H), 8.41–8.29 (m, 2H), 8.25–

8.20 (m, 2H), 8.12–7.99 (m, 2H), 7.90–7.80 (m, 2H), 7.50–7.43 (m, 4H), 7.30–7.18 (m, 12H), 6.98 (s, 1H), 3.69–3.51 (m, 12H). MS (MALDI-TOF) *m*/*z* = 1106.21 ([M], 85%). Trisbipyridine cobalt(III/II) hexafluorophosphate was synthesized as described in Chapter 2 of this dissertation in Section 2.2.3. The tris-4,4'-di-*tert*-butyl-2,2'-bipyridine cobalt(III/II) was synthesized in an identical way, substituting 4,4'-di-*tert*-butyl-2,2'-bipyridine for the 2,2'-bipyridine.

5.2.3. Fabrication and Dye Loading of TiO_2 Nanoparticulate Films

Nanoparticulate TiO_2 films were deposited on 1.5 cm x 2 cm cut FTO coated glass that had been sonicated successively in water/detergent, acetone, and isopropanol before being dried by N_2 flow. A dense TiO_2 blocking layer was deposited from titanium tetraisopropoxide and water via ALD (see Section 2.2.10). The commercial TiO_2 nanoparticles were diluted 1:1.5 by mass with absolute ethanol. Spin coating (Laurell WS-650Mz-23NPPB) this solution on the FTO at 4000 RPM for 30 seconds, followed by sintering at 450 °C (3 hour ramp up, 30 min hold), resulted in nanoparticulate films of ~1 μM thickness as measured by profilometry (Veeco Dektak 150). A razor blade was used to cut TiO_2 nanoparticle films to the desired size. The films were then submerged in a refluxing solution of $TiCl_4$ for 15 minutes, rinsed with water and ethanol in triplicate, and annealed following the same temperature ramp as above. The ZnP dye was dissolved in THF (0.05 mM), and the TiO_2 films were immersed in this solution overnight. Following dye loading, the dyed films were soaked in a solution of clean THF for ~15 minutes to eliminate any physisorbed ZnP. The films were then rinsed with THF followed by ACN before drying under N_2 flow.

5.2.4. Atomic Layer Deposition and Ozone Treatment

The aluminum ALD precursor was dimethylaluminum isopropoxide (DMAiso). ALD was performed with an Ultratech/Cambridge Nanotech Savannah 100 reactor with DMA(iso) and water as the aluminum and oxygen source, respectively. The reaction chamber was heated at 110 °C for all ALD experiments. The DMA(iso) precursor reservoir was heated at 80 °C. Alternating pulses of DMA(iso) and water (0.05 s pulse, 10 s expo, 30 s nitrogen purge) resulted in Al_2O_3 growth. After measurements with electrolyte solution, the films were allowed to "bake" in the ALD chamber at temperature under vacuum and N_2 flow for 15 minutes before subsequent depositions to eliminate an residual solvent. The growth rate of the ALD processes observed by a silicon witness chip was ~1 Å per cycle as measured by ellipsometry (J.A. Woollam M2000 model). TiO_2 blocking layers were fabricated as described in Section 2.2.10. Films were treated with ozone (when relevant) using a Ultratech/Cambridge Nanotech Savannah 100 reactor chamber (110 °C) and an integrated ozone generator. The ozone treatment process consisted of 10 repeated exposures of 60 s each to ozone. The ALD chamber pressure gauge typically recorded a pressure of ~200 Torr during these expos.

5.2.5. UV-Vis Spectroscopy

UV-Vis absorption measurements were performed on dye-loaded, TiO_2 nanoparticle films using a Cary-5000 NIR/Vis/UV spectrophotometer. A mask was employed and each film was measured in triplicate to mitigate inconsistencies that may arise from different placement of the film in relation to the light source/detector of the instrument.

5.2.6. Electrochemical Measurements

Electrochemical measurements were performed in the dark on a Solartron Analytical Modulab box with a 1 MS/s potentiostat module. To allow for multiple measurements and thicknesses of ALD-PT on the same TiO_2 film, measurements were performed with 2-electrode "clipped" devices, meaning redox shuttle solution was dropped onto the Pt CE (which had a Suryln-defined active area) and the TiO_2 electrode was clipped to the CE. The redox electrolyte was 0.2 M *tris*-(4,4'-di-*tert*-butyl-2,2'-bipyridine)cobalt(II) hexafluorophosphate ($Co(tbbpy)_3^{2+}$) and 0.02 M *tris*-(4,4'-di-*tert*-butyl-2,2'-bipyridine)cobalt(III) hexafluorophosphate ($Co(dtbbpy)_3^{3+}$) in acetonitrile with 0.1 M lithium perchlorate. The counter electrode was Pt from the thermal decomposition of H_2PtCl_6. After a measurement, the TiO_2 electrodes were rinsed with acetonitrile and dried under N_2 flow 3 consecutive times to remove any remaining cobalt shuttle.

Cyclic voltammetry (CV) measurements were performed in THF (0.2 M $TBAPF_6$ supporting electrolyte) with a Pt-wire counter electrode, a Pt-disk working electrode, and a Ag/AgCl in saturated KCl (aqueous) reference electrode. The solution was deoxygenated via N_2 bubbling for ~25 minutes before measurement. The scan rate was 500 mV per second.

5.3. Results and Discussion

5.3.1. ALD-PT of ZnP Films

The ALD-PT process used to post-treat ZnP films is described in detail in Chapter 4 of this dissertation and the full characterization of the ALD growth process and the resulting films is presented specifically in Sections 4.3.1, 4.3.2, and 4.3.3. The exact same ALD process was

performed on the dye-free films as was the ZnP-TiO_2 films (in fact, ALD on the dye-free and dyed films occurred simultaneously in the same ALD reactor). In the interest of brevity, these characterizations will not be re-discussed here.

5.3.2. Electrochemical Characterization of the Dye

All electrochemical measurements presented herein were performed in the dark, meaning no photo-excited dyes will be present. This results in dyes with fully occupied ground state molecular orbitals, meaning only the unoccupied orbitals that generally make up the dye excited state will be available to participate in any electron transfer processes. The potential location of the lowest energy unoccupied state (LUMO) can be ascertained by measuring the first reduction potential of the ZnP dye with cyclic voltammetry. Unfortunately, some instability in the non-surface adsorbed dye (plus a potential contaminant/degradation product in the dye) under reducing potentials made it difficult to assign a precise first reduction potential, Figure 5.1.

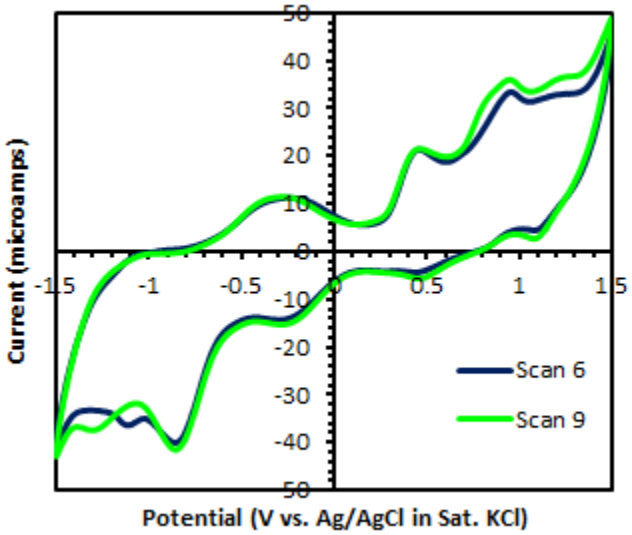

Figure 5.1. CV of ZnP Dye.
CV of ZnP dye in THF. The WE was Pt-disk, CE Pt-wire, and the reference was aqueous Ag/AgCl in saturated KCl. The potential was scanned from 1.5 V to -1.5 V at a rate of 500 mV/s. Each solution was deoxygenated via N_2 bubbling for 25 minutes, though some residual oxygen and/or water still remains. The primary peak of interest is the ZnP first reduction peak, but some instability is present in the ~-1 V region, making interpretation difficult.

It is tempting to assign the peak at ~ -0.75 V to this first reduction, but that would go directly against published literature on similar dyes where the only difference is the length of the alkyl chains in the alkoxy functional groups (see Scheme 4.1 for ZnP structure).[101, 131] Based on the aforementioned studies, the small, semi-reversible peaks near -1.1 V or -1.3 V in the 6th or 9th scan, respectively, are more likely the first reduction of ZnP. The large peaks near -0.75 V and 0.5 V are potentially the result of preadsorption of the dye to the electrode,[131] but may also be the result of some kind of degradation in the dye. Despite these unexpected peaks, the necessary peaks to match the CV with the literature for similar dyes can be found, assuaging any fears that the stock dye may be unusably degraded. While the CV measured is generally disappointing, the literature on extremely similar dyes still allows us to assign a tentative first reduction potential of *ca.* -1.3 V versus Ag/AgCl in saturated KCl for ZnP.[101] This assignment is further supported by

the fluorescence spectra shown in Figure 5.2, which are in good agreement with emission properties reported in the literature, namely emission features at approximately 660 nm and 705 nm for ZnP excited at 450 nm.[101, 131]

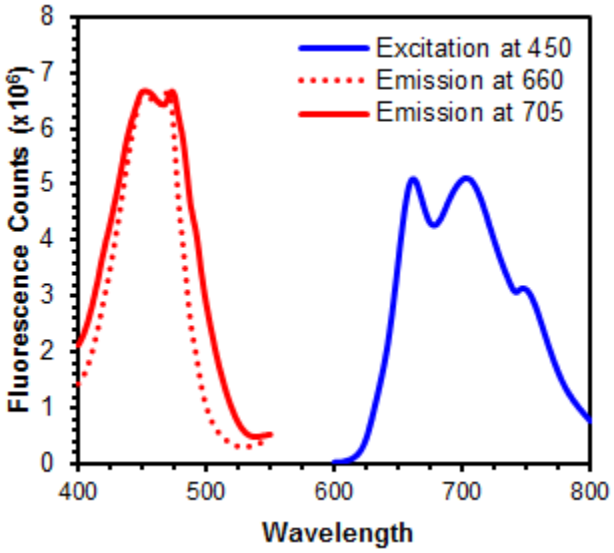

Figure 5.2. Fluorescence Spectra of ZnP dye in THF.
Fluorescence spectra of ZnP in THF with: 450 excitation, 600-800 emission scan (blue line); 400-550 excitation scan, 660 emission (red dotted line); and 400-550 excitation scan, 705 emission (red solid line). Note that emission at both 660 and 705 result in excitation scan peaks in the same location, with the integration of the 705 emission being larger. This suggests detector saturation as the cause of the split peaks in the excitation scan. It is undetermined whether the multiple peaks in the emission scan are due to saturation, electronic/vibrational structure, or a combination of the two.

5.3.3. Dark Current of ZnP-TiO_2 and TiO_2 Films with ALD-PT

The electrochemical data presented here utilize the $Co(dtbbpy)_3^{3+/2+}$ redox pair due to its larger size compared to $Co(bpy)_3^{3+/2+}$. The larger size of the shuttle minimizes the effects of ALD-PT film defects or the effects of pinholes in the underlying blocking layers on FTO because the shuttle is simply too large to fit into said pinholes. The dark current measurements presented herein return information on the rates of electron transfer out of the TiO_2 to the

oxidized form of the redox shuttle, in this case $Co(dtbbpy)_3^{3+}$. As mentioned previously, the term "dark current" is a grab-all expression for the potential dependent electron flow out of TiO_2 to the electrolyte and encompasses both electron interception and electron recombination. However, when actual dark current measurements take place, electron recombination to the dye is generally negligible due to the lack of illumination and therefore the lack of oxidized dye from charge injection. In this way, dark current measurements report primarily on potential dependent electron interception. The logarithmic dark current densities for dye-loaded TiO_2 (denoted ZnP-TiO_2) and bare TiO_2 with varying amounts of ALD-PT with Al_2O_3 are presented in Figure 5.3. Note that the absolute value of the current density was used as the typical sign convention of DSC measurements returns negative dark current density values. Thus, in Figure 5.3 more negative logarithmic current densities correspond to smaller measured dark current densities, with values less than 0 representing measured dark current densities smaller than 1 mA/cm^2.

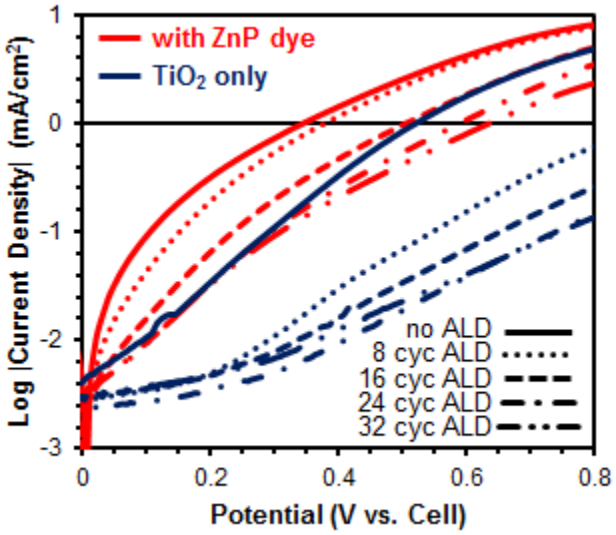

Figure 5.3. Logarithmic Dark Current Plots for ZnP-TiO_2 and TiO_2 with ALD-PT. Representative plot of the log of the absolute value of measured dark current density versus potential in a 2-electrode, clipped cell set up with increasing Al_2O_3 ALD-PT thickness. The ZnP-TiO_2 film is depicted in red while the TiO_2 film is in blue. No ALD: solid line; 8 AB ALD-PT cycles: dotted line; 16 cycles: dashed line; 24 cycles: dash-dot-dash line; 32 cycles: dash-dot-dot-dash line. Note that the growth rate of Al_2O_3 is approximately 1 Å/cycle. As a frame of reference, positive logarithmic values represent measured dark current densities greater than -1 mA/cm^2. The 2-electrode setup does not allow for an external reference, therefore 0 V is defined as the redox potential of the $Co(dtbbpy)_3^{3+/2+}$ couple.

Immediately apparent in Figure 5.3 is an order of magnitude or greater increase in dark current density when ZnP-TiO_2 is compared to bare TiO_2 across all amounts of ALD-PT. Particularly interesting is the relative effects the first 8 cycles (or ~8 Å) of Al_2O_3 ALD-PT; when the dye is present, there is almost no change, but measured dark current is up to 10 times smaller with the same amount of ALD and no dye. While negative effects on the ALD-PT film deposition quality in the presence of dye cannot be completely ruled out as an explanation for this difference, the leeway provided by the larger $Co(dtbbpy)_3^{3+/2+}$ shuttle and the QCM evidence presented in Section 4.3.2 both support that some sort of dye-facilitated interception process is in play. Additionally, note that the $TiCl_4$ treatment applied to these films before dye loading should minimize the contribution of surface state passivation to the observed improvement.[29, 132]

5.3.4. OCVD in ZnP-TiO_2 or TiO_2 Films with ALD-PT

Open-circuit voltage decay (OCVD) measurements report on the same process as dark current measurements, but, instead of the magnitude of electron flow, OCVD reports on the average lifetime of an electron in TiO_2 at a particular potential. Different from open-circuit *photovoltage* decays, OCVD instead uses a potentiostat (as opposed to photoinjected electrons from the dye) to populate the TiO_2 CB and is therefore possible to perform in the dark. In performing the measurement, a potential near the TiO_2 CB location is applied to the working electrode (in this case TiO_2 nanoparticle films) for a set amount of time before being instantly removed. The potential decay of the electrode over time (dV_{oc}/dt) at open circuit is measured and converted into an average electron lifetime τ_n via Equation 5.1:

$$\tau_n = \frac{k_B T}{q}\left(\frac{dV_{oc}}{dt}\right)^{-1} \qquad 5.1$$

where k_B is the Boltzmann constant, T is the temperature in Kelvin, and q is the elementary charge.[133] Plots of τ_n versus potential, with τ_n being plotted on a log scale, will result in a straight line if only one decay process is occurring. Multiple decay processes typically result in curved lines, though curved lines provide no additional concrete information beyond the simple presence of more than one decay process.[133] Since this all occurs in the dark and without even initial illumination, interception of a potentiostat-injected electron in TiO_2 by the redox shuttle is the primary pathway for potential decay (though in some cases decay through the potentiostat itself is also possible). OCVD traces for ZnP-TiO_2 and bare TiO_2 with increasing amounts of Al_2O_3 ALD-PT are shown in Figure 5.4.

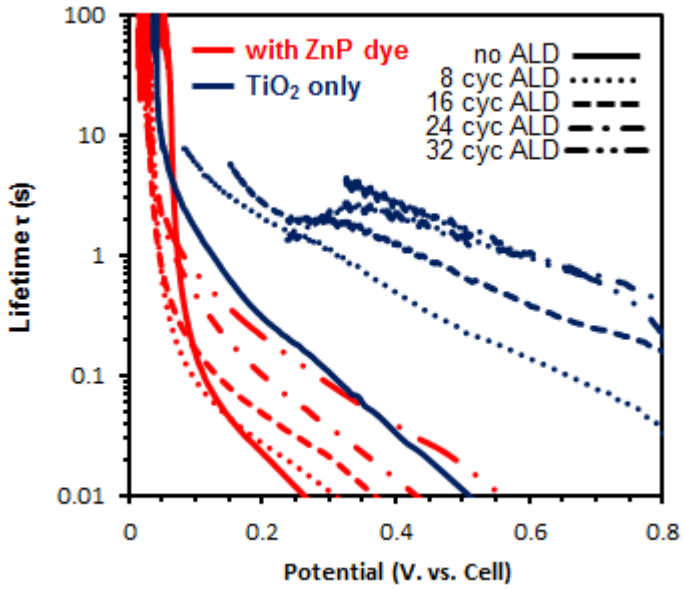

Figure 5.4. OCVD for ZnP-TiO_2 and Bare TiO_2 with ALD-PT.
Plots of electron lifetime τ in TiO_2 versus potential in a 2-electrode, clipped cell set up with increasing Al_2O_3 ALD-PT thickness. The ZnP-TiO_2 film is depicted in red while the TiO_2 film is in blue. No ALD: solid line; 8 AB ALD-PT cycles: dotted line; 16 cycles: dashed line; 24 cycles: dash-dot-dash line; 32 cycles: dash-dot-dot-dash line. Note that the growth rate of Al_2O_3 is approximately 1 Å/cycle. The 2-electrode setup does not allow for an external reference, therefore 0 V is defined as the redox potential of the $Co(dtbbpy)_3^{3+/2+}$ couple.

As was expected based on the dark current behavior shown in Figure 5.3, electron lifetimes are dramatically improved by the application of ALD-PT for bare TiO_2 films, but much more modest improvement is evident when ZnP dye is present. ZnP-TiO_2 shows a large curve, which might lead one to suspect multiple decay pathways. However, in the case of the 2-electrode setup used here, this is more likely due to an asymptotic-like approach of the electrode potential to 0 V resulting from the form of Equation 5.1; *i.e.*, as electron transfer slows/ceases because the electrode potential is approaching unperturbed-like conditions, the lifetime of the electron heads toward infinity. Thus, only portions of the OCVD plot *after* the curve are used in analysis. The near identical lifetimes for bare TiO_2 with 24 and 32 cycles of ALD-PT suggest that decay of potential through the potentiostat may be occurring, a result only expected with highly resistive

films. This is clearly not the case when ZnP dye is present, as consistent improvement in electron lifetime is seen from 8 ALD-PT cycles through 32 ALD-PT cycles. Taken together, both the dark current densities in Figure 5.3 and the OCVDs in Figure 5.4 strongly suggest electron interception facilitated in some way the surface adsorbed ZnP dye.

5.3.5. Dark Current, OCVD, and Rates of Electron Transfer

Both dark current densities and OCVD lifetimes can be converted to rates of electron transfer. Current is reported in (milli)amperes, and amperes are defined as an electron flow equivalent to 1 coulomb per second. Since a coulomb is approximately equivalent to the charge of 6.242×10^{18} electrons, the current densities reported in mA/cm^2 can be converted into electrons per second per cm^2 by multiplying the current density (in A) by 6.242×10^{18}. Since the cm^2 term is just an area normalization, the resulting electrons per second is the approximate rate of electron transfer out of TiO_2 at a given potential. For OCVD, we assume that only one process contributes to the decay; therefore, τ will be proportional to $1/k_{ET}$ and approximate rates can be obtained by taking the inverse of the lifetime, *i.e.*, $1/\tau$, at a particular device potential.

The primary electron transfer process associated with the rates discussed in the previous paragraph is the reduction of $Co(dtbbpy)_3^{3+}$ by an electron in TiO_2. When ALD-PT is applied, the metal oxide coating (provided the oxide possesses an E_{CB} higher than TiO_2) creates a barrier to electron transfer. If we approximate this blocking layer as a simple square barrier, the rate constant for electron transfer, k_{ET}, can be described with the distant dependent exponential in Equation 5.2.[29, 123, 128, 134]

$$k_{ET} = k_{ET}^{\circ} e^{-\beta d} \qquad (5.2)$$

Here, β is a tunneling parameter that describes the "steepness" of the decrease in rate as d, the thickness of the intervening medium, increases. Thus, if the ET rate is tunneling controlled, a plot of the natural log of $1/\tau$ versus barrier thickness in Å should result in a straight line with a slope of $-\beta$ in units of $Å^{-1}$.

5.3.6. Dye-mediated Electron Interception: Dark Current Densities

Beginning first with dark current densities, plots of the natural log of the rate of electrons flowing from TiO_2 to $Co(dtbbpy)_3^{3+}$ versus Al_2O_3 barrier thickness are shown in Figure 5.5.

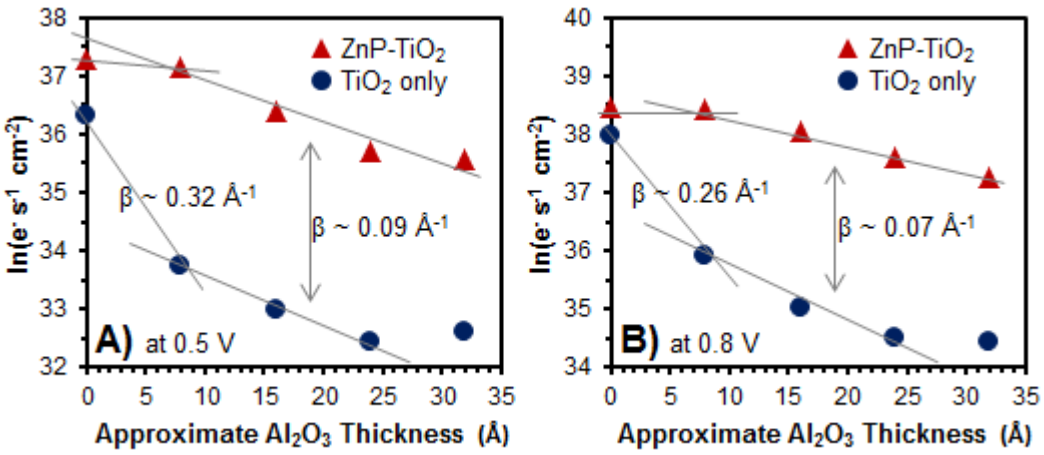

Figure 5.5. Rates of Electron Transfer vs. Barrier Thickness from Dark Current Densities. Plots of the natural log of rates of ET from TiO_2 to $Co(dtbbpy)_3^{3+}$ at A) 0.5 V versus cell and B) 0.8 V versus cell with (red triangles) and without (blue circles) ZnP dye and increasingly thick Al_2O_3 ALD-PT barrier layers. The gray lines are approximate slopes and were added to show the apparent dual-nature of the distance dependence. Actual β were calculated via Equation 5.2 from the slope between the points connected by a given line. The β for ZnP-TiO_2 and bare TiO_2 are similar for ALD thicknesses in the 8-24 Å range, suggesting the same mechanism of interception at these barrier thicknesses.

Note that, because current densities were used in determining the number of electrons flowing at a given potential and this number is not controlled for the number of donors/acceptors present, the reported "rate" is not a localized donor to localized acceptor rate but instead the summation

of electrons transferred between numerous (uncounted) donors and acceptors. Thus, the ~10^{14} s^{-1} limit to ET rate from Marcus Theory can be "exceeded". as the "rates" measured here are the aggregate of all ET processes happening in the system.[134] Returning to Figure 5.5 the natural log of the total electron flow versus Al_2O_3 barrier thickness is shown for two potentials, 0.5 V (A) and 0.8 V (B) versus the redox potential of $Co(dtbbpy)_3^{3+/2+}$ (*i.e.*, versus cell). Because the growth rate of DMA(iso) and water under the ALD-PT conditions here is *ca*. 1 Å/AB cycle, cycle number serves well as a thickness proxy. The relative rates of ET from TiO_2 show the expected trend between ZnP-TiO_2 and bare-TiO_2 based on dark current densities in Figure 5.3. Particularly interesting at both potentials is difference between non-PT films and films with 8 cycles (*i.e.*, an 8 Å barrier layer) ALD-PT. While bare TiO_2 immediately undergo a sharp decrease in rate, the rate of ET in ZnP-TiO_2 films remains mostly unchanged. After 8 cycles of PT, both bare TiO_2 films and ZnP-TiO_2 films demonstrate nearly identical slopes (albeit, with some potential dependence) for 8 cycles through 24 cycles ALD-PT (8 Å–24 Å barrier thickness). At this point, bare TiO_2 levels off, indicating little to no distance dependence in the rate of ET (similar to ZnP-TiO_2 between 0 and 8 cycles ALD-PT), while ZnP-TiO_2 continues along the same trend.

By fitting the relevant linear regions in Figure 5.5, β values can be extracted via Equation 5.2.Values for β of 0.32 $Å^{-1}$ and 0.26 $Å^{-1}$ for 0.5 V and 0.8 V, respectively, were obtained as the Al_2O_3 ALD-PT layer thickness increased from 0 to 8 Å on bare TiO_2 films. Over this same range, ZnP-TiO_2 sees almost no change in rate, resulting in a miniscule β. Both films at each potential yield β of 0.07 to 0.09 $Å^{-1}$ for the 8-24 Å thickness range. While these slopes are small

enough to suggest only very minor distance dependence, their similarity suggests that whatever distance dependence exists, it is affected in the same way by the continued deposition of Al_2O_3.

5.3.7. Dye-mediated Electron Interception: OCVD

The effect of ZnP on the rates of ET from TiO_2 to $Co(dtbbpy)_3^{3+/2+}$ with ALD-PT is presented in Figure 5.6, which depicts the rates of ET obtained from OCVD measurements.

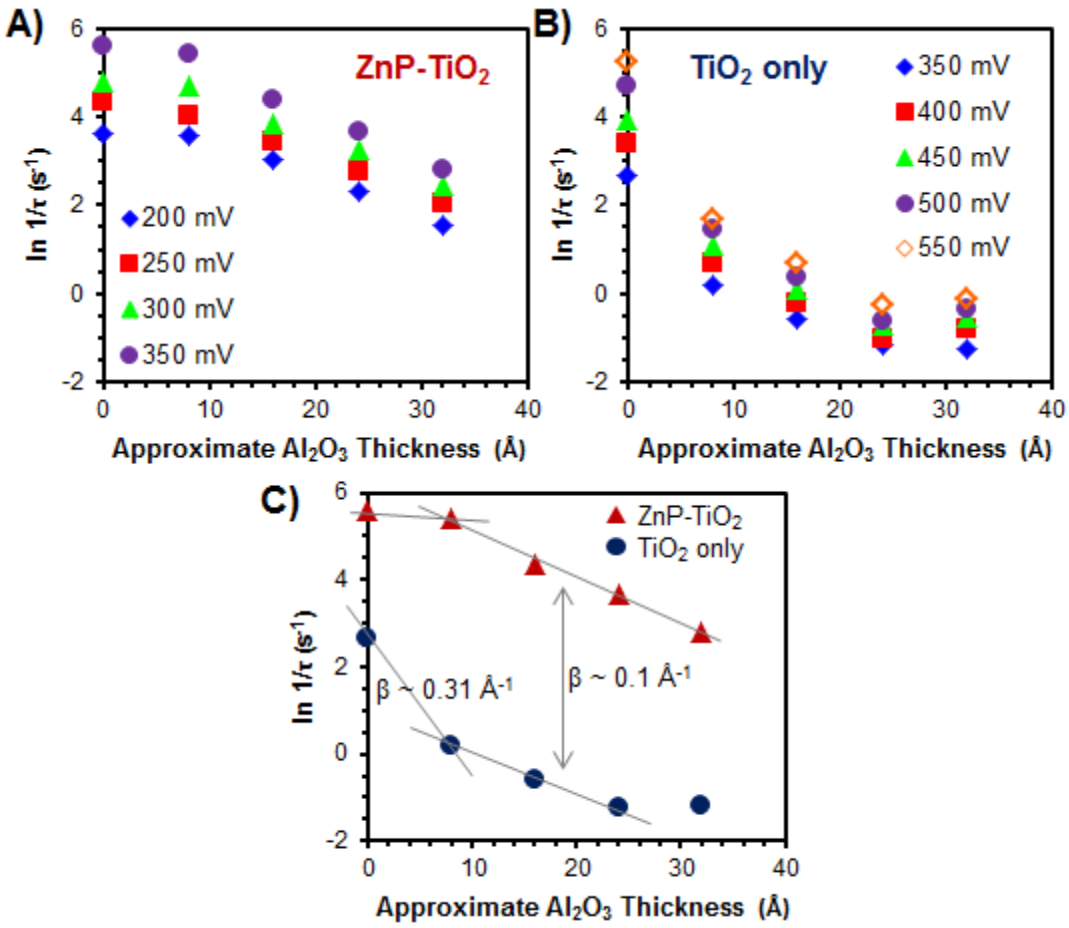

Figure 5.6. Rates of Electron Transfer vs. Barrier Thickness from OCVD Measurements
Plots of the natural log of $1/\tau$ versus ALD-PT Al_2O_3 barrier thickness for A) ZnP-TiO_2 and B) bare TiO_2. τ were obtained from the OCVD plots shown in Figure 5.4. The results of choosing different potentials at which to monitor τ are shown, with trend in behavior being equivalent across the applicable potentials. Note that the same colors/shapes do not represent the same potential in A as in B. C) Comparison of ZnP-TiO_2 (red triangles) and bare TiO_2 (blue circles) at 350 mV. Similar β to those seen in Figure 5.5 are observed.

Because the electron lifetime τ and thus the rate of ET are also potential dependent in OCVD, Figure 5.6 A and B depict the natural log of the rates obtained across several different potentials for ZnP-TiO_2 and bare TiO_2, respectively. Across all examined potentials, the rates of ET from OCVD (predictably) follow the same pattern as the dark current density rates discussed in the previous section. The nature of OCVD measurements and vastly different rates of ET between the films makes it difficult to find a common potential with which to compare the ZnP-TiO_2 and bare TiO_2 films at all thicknesses. In the case of the devices measured for Figure 5.6, only 0.35 V allowed for comparison across all films and barrier thickness without resorting to data extrapolation. For this reason, the natural log of the rates at this potential are shown in Figure 5.6 C with the accompanying β values. With β of 0.31 $Å^{-1}$ and for bare TiO_2 in the 0-8 cycle regime and 0.1 $Å^{-1}$ in the 8-24/32 cycle regime, the distance dependence of ET measure by OCVD agrees will with than obtained from the dark current densities in the previous section.

5.3.8. Distance Dependency of ET Rate for Bare TiO_2 with ALD-PT Films

An approximate schematic of the components in the ZnP-TiO_2-PT system and their relevant energetic potentials versus the redox potential of $Co(dtbbpy)_3^{3+/2+}$ are shown in Figure 5.7.

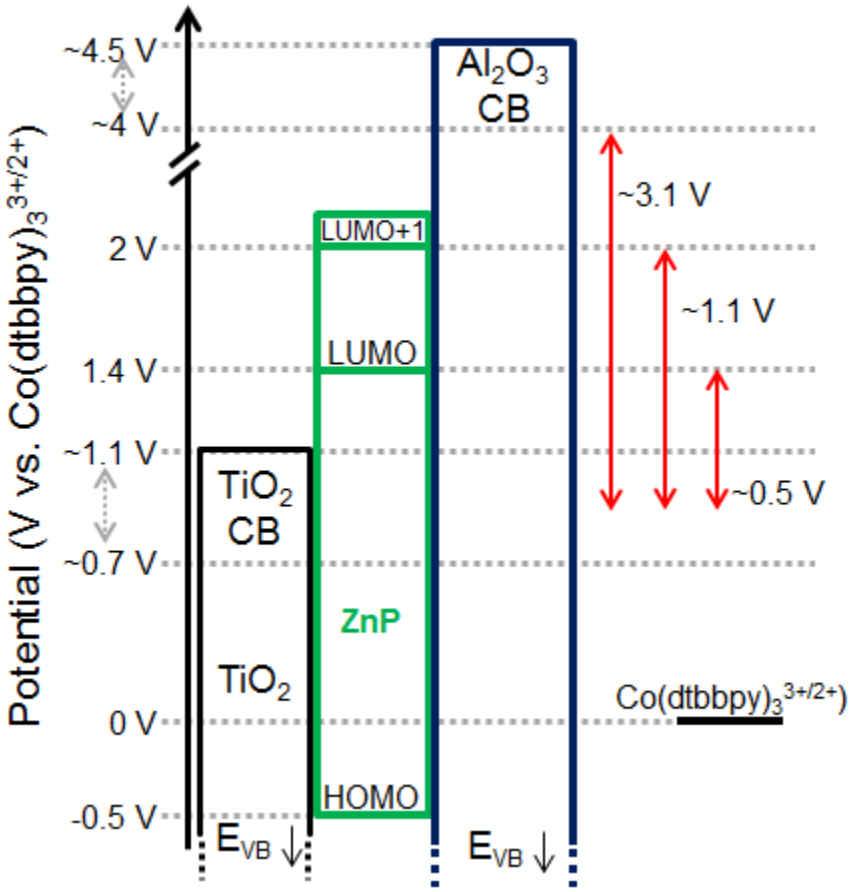

Figure 5.7. Energy Level Diagram for ZnP-TiO_2 with ALD-PT Al_2O_3 and $Co(dtbbpy)_3^{3+/2+}$. Schematic representation of the energy levels of TiO_2 CB, ZnP dye, and Al_2O_3 versus the redox potential of $Co(dtbbpy)_3^{3+/2+}$ (-0.23 V vs. Fc/Fc^+). The $Co(dtbbpy)_3^{3+/2+}$ redox potential is arbitrarily set to 0 V. The red arrows denote approximate potential differences, a good proxy for barrier heights d in Equation 5.2. Higher energy potentials have been arbitrarily assigned as positive to better match 2-electrode conventions in DSCs.

The height of the barrier presented by Al_2O_3 in Figure 5.7 is larger than 3 eV. As β is expected to scale with square root of the barrier height, large β are expected for Al_2O_3 on TiO_2. The ~0.3 $Å^{-1}$ β values obtained for the tunneling region (0-8 Å) in bare TiO_2 films in this work are significantly smaller than expected. Previous results for ALD coatings of Al_2O_3 on TiO_2 nanoparticles with TMA and water yielded β of ~1.1 $Å^{-1}$, a value significantly larger than that reported here.[29] Two potential reasons that may result in the deviation from expected results are poor barrier layer coverage on TiO_2 or inaccurate assumptions of barrier thickness. The

DMA(iso) precursor was explicitly used because it is a milder Al precursor that would not result in dye degradation. This same property may also result in poorer film growth on TiO_2. The same is true of film growth rate. Direct physical characterization of ALD-PT film thickness on TiO_2 NPs is difficult, thus thickness are obtained from deposition on flat Si in conjunction with observed growth rates via QCM. However, if these methods overestimate the actual growth of Al_2O_3, calculated β will be affected. For instance, if the growth rate in these experiments were actually half of what is reported, all β constants would immediately double. The same is true of previous experiments: if the ALD growth rate assumed across the initial 5 AB cycles of TMA and water deposition in Reference 29 is instead half of the real growth rate, the actual β will half that of what is reported. Another potential cause of the different distance dependence for bare TiO_2 and Al_2O_3 seen here is the possibility of trap states in Al_2O_3 resulting from poorer deposition from DMA(iso) compared to TMA. There is some evidence for trap states in amorphous Al_2O_3 resulting from oxygen defects (similar to TiO_2), and, if they exist in this system, these trap states could be participating in the ET processes.[135]

The much smaller distance dependence seen beyond 8 Å for bare TiO_2 with Al_2O_3 ALD-PT suggests a change in mechanism for ET.[136] Electron hopping through Al_2O_3 is unlikely (unless, as mentioned above, accessible trap states exist), so some other process is likely at play. The complicated ET process of DSCs could lead to any number of difficult to predict routes for interception/potential decay, from decay through the instrument to contact in undesired locations between the working electrode and counter electrode via the redox electrolyte. Regardless of how this different mechanism functions, the results in Sections 5.3.6 and 5.3.7 support that the mechanism of ET in this 8-32 Å regime is the same for both bare TiO_2 and ZnP-TiO_2 films.

5.3.9. Distance Dependency of ET for ZnP-TiO_2 films with ALD-PT and Calculated Molecular Orbital Locations

Regardless of technique, selected potential, or number of ALD-PT cycles, ET in ZnP-TiO_2 systems is always faster than in the comparable bare TiO_2 case. While this fact alone does not allow for conclusions to be made on *why* this is the case, it can be concluded that ZnP does have an effect on the rates of interception in DSCs with $Co(dtbbpy)_3^{3+/2+}$, even without the presence of ALD-PT layers. What is particularly interesting in the case of ZnP-TiO_2 is the near-negligible distance dependence observed for both dark current density and OCVD rates between the no barrier and 8 Å barrier cases. This may suggest that, even without barrier layers, electron interception in ZnP-TiO_2 utilizes dye orbitals in some way. To this end, density function theory (DFT) was used to calculate the localization (and relative energies) of the HOMO, LUMO, and LUMO+1/+2 orbitals in ZnP, Figure 5.8.

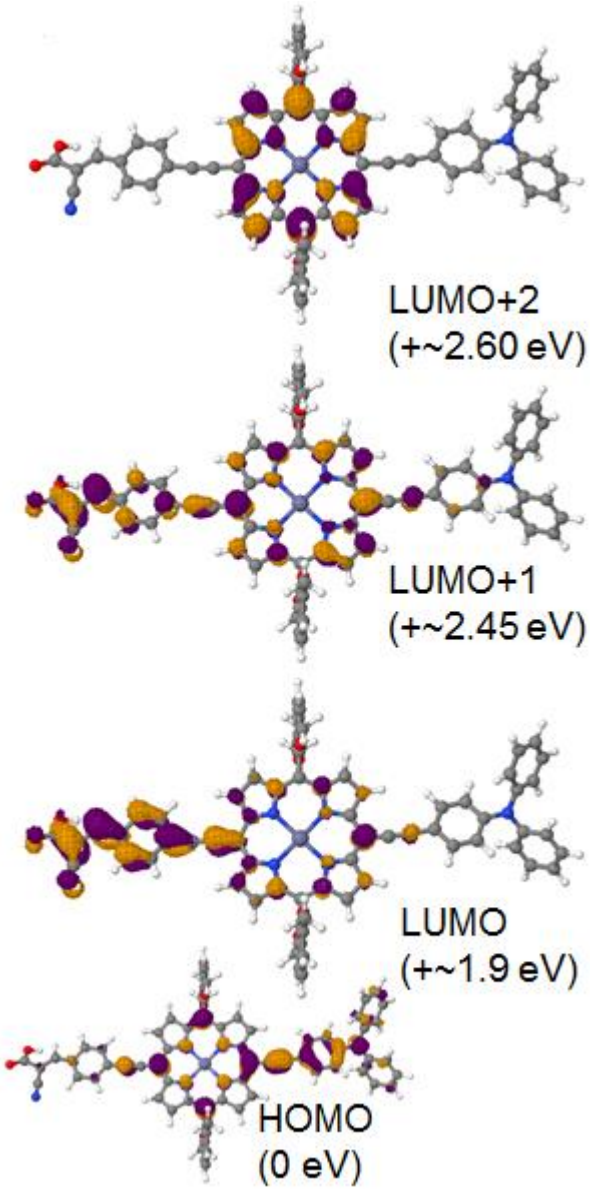

Figure 5.8. DFT Calculated LUMO Orbital Localization and Energies Relative to the HOMO Energy for ZnP Dye.
Arbitrarily setting the HOMO energy to 0 eV and higher energies as more positive, the calculated HOMO-LUMO gap is found to be ~1.9 eV, which corresponds well to the observed absorbance and fluorescence features of the ZnP dye. As would be expected for a DSC dye, the HOMO orbital originates in the triphenylamine moiety but delocalizes across the porphyrin while the LUMO and LUMO+1 orbitals localize primarily on the cyanoacrylic acid anchoring group. Calculations by Nicholas E. Jackson, Ph. D.

As is expected for a DSC-type organic dye, the HOMO, while delocalized across the porphyrin backbone to a certain extent, primarily resides on the triphenylamine moiety and the

LUMO primarily resides on the cyanoacrylic acid anchoring group. This arrangement allows for efficient charge injection from the LUMO while also keeping the HOMO orbitals accessible to the redox shuttle for regeneration while the device is operating under illumination. As the measurements presented here are conducted in the dark only, the HOMO orbitals are expected to be fully occupied, leaving only the LUMO orbitals available to facilitate electron back-transfer. The potentials of both the HOMO and LUMO orbitals of ZnP relative to $Co(dtbbpy)_3^{3+/2+}$, TiO_2, and Al_2O_3 are shown in Figure 5.7. Figure 5.9 shows ZnP with some relevant atom-to-atom distances annotated.

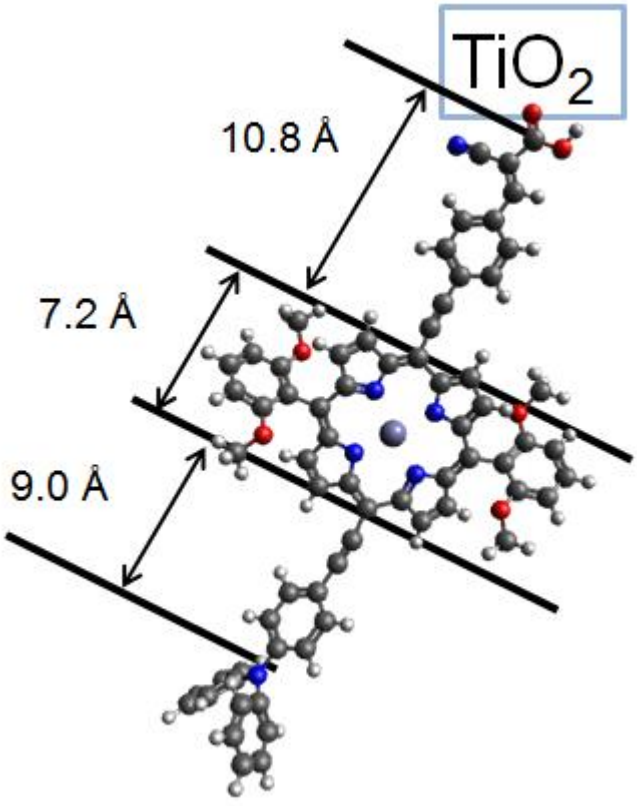

Figure 5.9. Structure of ZnP with Relevant Distances Annotated.
ZnP with distances relevant to the location of LUMO orbitals, ET to $Co(dtbbpy)_3^{3+}$, and enshroudment via ALD-PT.

From Figure 5.8, we see that the LUMO orbital, which is the lowest energy unoccupied orbital, is located primarily on and near the cyanoacrylic acid anchoring group, which is spatially located immediately adjacent to the TiO_2 surface and (likely) electronically coupled with TiO_2 CB orbitals. This makes these unoccupied orbitals strong candidates to facilitate ET, with the associated barrier height being the difference between the TiO_2 CB potential and the ZnP LUMO potential as seen in Figure 5.7. The distance between TiO_2 and the porphyrin cage that this moiety occupies is about 11 Å, meaning 8 Å of ALD-PT Al_2O_3 would not be sufficient to completely enshroud this section of the ZnP dye. However, 16 Å would likely cut off this section of the dye from the surrounding medium, forcing ET to the $Co(dtbbpy)_3^{3+}$ in solution to occur through a different mechanism, one which is dependent on the Al_2O_3 barrier thickness. This could explain the observation of no distance dependence for ET in ZnP-TiO_2 for 8 cycles of ALD-PT.

As seen in Figure 5.5 and Figure 5.6, the slope of the natural log of $1/\tau$ versus barrier thickness for barrier thicknesses of 8-24 Å is nearly identical for both ZnP-TiO_2 and bare TiO_2. As mentioned previously, this is suggestive of the distance dependence having the same origin in both systems. However, the raw rates of ET in ZnP-TiO_2 remain much larger than in bare TiO_2, so clearly the ET process is not exclusively happening through the Al_2O_3; if that were the case, the magnitude of the rates would be expected to be similar. One possible explanation for the difference in magnitude of the observed rates could be distance-independent ET facilitated by the dye. Related zinc porphyrin systems such as a series of *meso-meso* ethyne-bridged zinc porphyrin oligomers have been shown to demonstrate very little distance dependence in molecular wire, single molecule conductance experiments ($\beta \sim 0.04$ Å^{-1}).[137-139] Thus, even as the

intervening Al_2O_3 barrier layer becomes thicker, the ET pathway through the dye remains unchanged. Another explanation for the observed differences is incomplete coverage of TiO_2 with Al_2O_3, creating pinholes or bare areas for fast interception by $Co(dtbbpy)_3^{3+}$. To help elucidate which explanation may be more likely, the ZnP dye was removed from the ZnP-TiO_2 substrate via ozonolysis. Recall that both Chapter 4 and the experiments in this chapter have established that ZnP is accessible to the redox shuttle even with relatively thick (~30 Å) layers of Al_2O_3. Thus, treatment with ozone results in the complete degradation of ZnP and the loss of all light harvesting abilities. The effect of this treatment on rates of ET as measure by OCVD and dark current densities is presented in Figure 5.10.

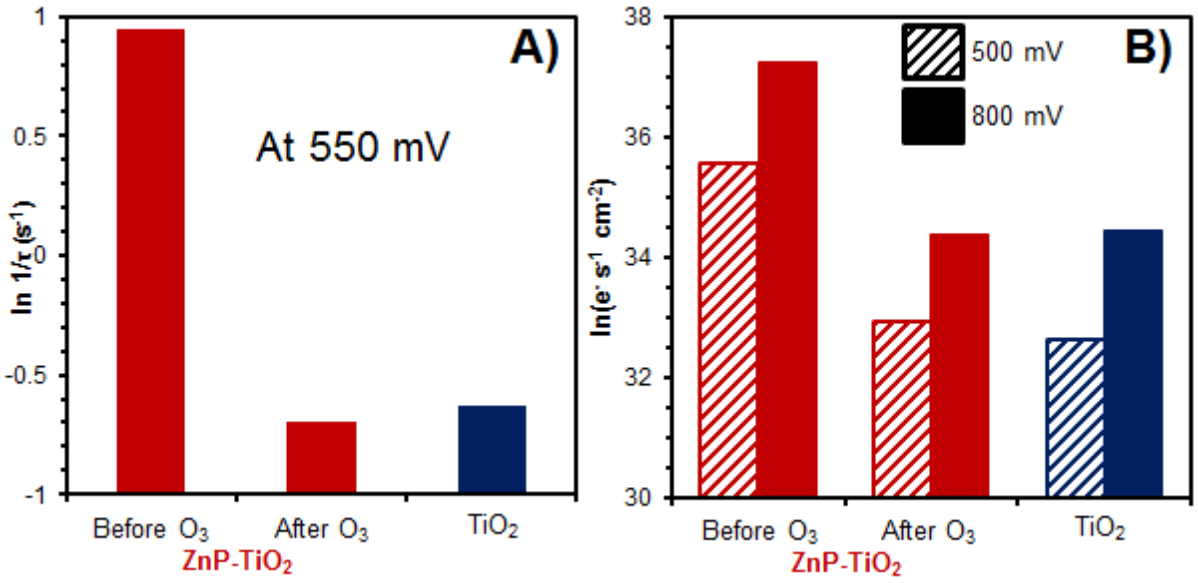

Figure 5.10. Effect of Ozone Treatment on ET Rates For ZnP-TiO_2.
Effect of treatment with O_3 at elevated temperature (110 °C) after 32 AB cycles Al_2O_3 ALD-PT on ET rates measure by A) OCVD and B) dark current for ZnP-TiO_2 (red). For comparison, the rates of ET on ALD-PT (32 AB cycles) bare TiO_2 are also shown (blue). Treatment with O_3 results in complete disappearance of light harvesting for ZnP-TiO_2 and rates of ET that are approximately equivalent to bare TiO_2.

After removal of the ZnP dye via ozone, the rates of ET between the formerly ZnP-TiO_2 films and the bare TiO_2 films are nearly equivalent. This supports ZnP dye as the major facilitator of electron back-transfer in the ALD-PT devices shown here.

5.4. Conclusions

Utilizing ALD-PT of Al_2O_3 around the zinc porphyrin-based ZnP dye, the contribution of the dye to electron interception in DSC-like systems was isolated and interrogated. Rates obtained from both dark current densities and OCVD measurements show very little distance dependence for Al_2O_3 blocking layers of ~8 Å around the ZnP dye. This corresponds with the calculated LUMO orbitals in ZnP being not completely isolated from electrolyte solution and possibly facilitating rapid electron back-transfer in this system. Bulky, shuttle blocking alkyl chains, which this specific dye notably lacks, might help to distance a shuttle from this vulnerable site, reducing the rate of interception. Additionally, ZnP was shown to demonstrate only mild barrier thickness dependence beyond 8 Å, and the dependence was similar to that observed with bare TiO_2 electrodes. It is hypothesized that this result, as well as the generally observed difference in rate between ZnP-TiO_2 and bare TiO_2, is due to the sum of a distance-independent ET process facilitated by ZnP and a different, unspecified process that involves the Al_2O_3 barrier layer. Removal of ZnP dye by ozonolysis and the subsequent decrease in ET rate support this hypothesis.

While the calculated β constants for bare TiO_2 coated with Al_2O_3 are smaller than anticipated, the results still show clear evidence for ZnP facilitation of electron interception. Thus, the possibility of this process should be taken into account when designing new DSC or

DSC-like architectures. With the recent decrease in popularity of dye-sensitized solar cells and the resulting shift in focus to dye-sensitized photoelectrochemical cells, controlling this processes is especially relevant; many solar fuel-generating catalytic reactions involve the buildup of multiple oxidizing or reducing equivalents at a single site, making these electrons and/or holes especially vulnerable to recombination processes, even more so when considering the generally slow rates of these catalytic reactions.

Additionally, the presented results offer a potential explanation for the unexpectedly small improvements often seen in V_{oc} for DSCs utilizing the ALD-PT technique. This technique is often employed around highly conjugated donor-acceptor dyes similar to the one studied here. As the dye must necessarily remain in electrical contact with the redox shuttle for the device to function, the potential for dye-facilitated electron interception exists in these systems as well. However, the absence of excited dyes/empty HOMO orbitals along with the incredible complexity of the various rates in operating DSCs complicates comparison of these results with those obtained in DSCs operating under illumination.

Chapter 6. Determining the Conduction Band Potential of Nb_2O_5 Fabricated by Atomic Layer Deposition via Electrochemical Impedance Spectroscopy and Mott-Schottky Analysis

6.1. Introduction and Background Information

The open circuit photovoltage (V_{oc}) is a key parameter in determining the power conversion efficiency of a photovoltaic device and therefore methods of increasing V_{oc} have been the focus of numerous studies.[119, 140-144] V_{oc} is defined by the potential difference between the front and back contacts of a photovoltaic device when the net current flow is 0 (*i.e.*, current is flowing as fast in the desired "forward" direction as in the deleterious "backward" direction). In DSCs, this potential difference is the difference between the quasi-Fermi level (E_{qf}) in the semiconductor (usually TiO_2) and the redox shuttle formal potential at the dark electrode; V_{oc} in p-i-n junction devices is limited by the potential difference between the valence band of the p-type semiconductor and the conduction band of the n-type semiconductor. Thus, regardless of device design, the theoretical maximum V_{oc} is material dependent, and one of the most straightforward approaches to increasing V_{oc} in all device architectures is substituting an n-type semiconductor material with a higher energy E_{CB}. However, this substitution can have undesired effects as well. Using DSCs as an example, if TiO_2 is replaced with a higher E_{CB} semiconductor, the increased driving force for electron interception by the redox shuttle increases the rate of interception, leading to a lower than expected E_{qf} and thus a smaller than predicted V_{oc} increase. Additionally, the higher E_{CB} can slow charge injection from the excited dye, reducing obtainable photocurrent. Changing the redox shuttle can cause analogous issues, again creating a larger driving force for electron interception that speeds this process in results in a lower E_{qf}. Chapters 2 and 3 of this dissertation discussed how increasing V_{oc}/slowing electron interception could be approached via changing the redox couple/dark electrode; this chapter focuses on possible changes to the photoelectrode, specifically either coating or completely replacing TiO_2 with ALD Nb_2O_5. While

the work presented forthwith has implications for all types of device architectures that utilize n-type semiconductors, specifically TiO_2, the discussion here will be presented in terms of DSCs for both continuity and simplicity.

As alluded to above, in DSCs the E_{qf} depends predominantly on the E_{CB} of the semiconductor and the rate of electron interception (*i.e.*, reduction of the oxidized half of the redox couple by an electron in the semiconductor). Thus, any modification to the TiO_2 (or other metal oxide semiconductor) that slows the rate of interception will lead to an increase in V_{oc}, provided all other rates, such as charge injection from the light absorber and dye regeneration by the redox shuttle, remain constant. Note that electron recombination, *i.e.*, reduction of oxidized dye by electrons in the semiconductor, may also contribute to E_{qf} but is typically dependent on the rate of dye regeneration by the electron shuttle and is therefore not discussed in this chapter. ALD is a commonly used technique for modifying the semiconductor electrode to slow interception processes as ALD allows for the conformal coating of high area and high aspect ratio electrodes with a variety of metal oxides, nitrides, or chalcogenides with angstrom level thickness control. For example, deposition of a thin coating of insulating metal oxide Al_2O_3 on the photoelectrode has been shown to dramatically slow interception.[30, 31] Other metal oxides deposited include TiO_2 (if the photoelectrode itself is not TiO_2),[29, 145] ZrO_2,[54, 146] Ga_2O_3,[54] and Nb_2O_5,[57, 147, 148] among others.[58] In each case, the deposited material possessed a higher E_{CB} than the underlying electrode material, creating an energetic barrier to electron transfer and generally slowing interception. With slowed interception, the E_{qf} moves to higher potentials, increasing the V_{oc}. However, thanks in part to the same higher E_{CB} that slows interception, many of these metal oxide overlayers dramatically slow charge injection from the sensitizer, decreasing the

obtainable photocurrent.[30, 31, 125] In some cases, application of an ALD overlayer *after* dye adsorption (*i.e.*, ALD post treatment) can provide similar benefits without stopping charge injection (as seen in Chapter 4 of this dissertation and elsewhere[58]). However, as Chapter 5 of this dissertation outlined, tunneling of the electron through the dye to the redox shuttle can limit the utility of this approach. Thus, an overlayer material with an E_{CB} location low enough in energy to allow dyes to charge inject yet high enough in energy to limit interception has the potential to improve V_{oc} without limiting photocurrent.

With an approximate E_{CB} of 80-100 mV higher in energy than TiO_2, Nb_2O_5 is a promising overlayer candidate or replacement semiconductor. In fact, many studies have used it precisely such.[55, 57, 149-152] Some of these studies have taken advantage of the unique capabilities of ALD to deposit Nb_2O_5, but have not independently determined the E_{CB} of Nb_2O_5 fabricated by ALD. Thus, impedance spectroscopy was performed on ALD films of heat treated and as deposited films of Nb_2O_5. Using Mott-Schottky analysis, the location of E_{CB} for ALD Nb_2O_5 was determined in 1 M aqueous hydroxide solution and compared to the determined E_{CB} for ALD TiO_2. It was ascertained that under all conditions, the E_{CB} of ALD Nb_2O_5 was higher in energy than that of TiO_2, but the magnitude of the difference depends on the heat treatment of Nb_2O_5 films.

6.2. Experimental Methods and Instrumentation

6.2.1. Reagents

All chemicals were used as received without any additional purification or modification. Tris(diethylamino)(*tert*-butylimido)niobium(V) was purchased from Strem Chemicals, Inc (98%,

Newburyport, MA). Titanium(IV) isopropoxide was purchased from Sigma Aldrich (99.999% trace metal basis, St. Louis, MO). All other chemicals, including sodium hydroxide, potassium hydroxide, sodium carbonate, and sodium bicarbonate were also purchased from Sigma Aldrich. House deionized water was used in all experiments. Fluorine-doped tin oxide (FTO) glass (8 Ohm resistance) was purchased from Hartford Glass (Hartford City, Indiana).

6.2.2. Thin Film Fabrication by Atomic Layer Deposition

Before ALD, FTO glass was cut into 2 cm by 2 cm squares and sonicated for 15 minutes in detergent in water, followed by acetone, and finally isopropanol. All ALD was performed on a Ultratech/CambridgeNanotech Savannah 100 ALD system. The carrier gas was house N_2 ran through an oxygen and water scrubber. The niobium metal precursor was tris(diethylamino)(*tert*-butylimido)niobium(V) and the titanium metal precursor was titanium(IV) isopropoxide (TTIP). House deionized water was the oxygen source. The ALD reaction chamber was held at 200 °C and exposed to the vacuum pump (baseline pressure ~ 0.7 torr); the nitrogen carrier gas flow rate was 15 sccm. The Nb precursor was held at 120 °C and the Ti precursor at 90 °C. To grow niobium(V) oxide films, the Nb was pulsed for 1 s and followed by a 25 s N_2 purge (A half-cycle). The water was pulsed for 0.02 s and followed by an identical 25 s N_2 purge (B half-cycle). 500 alternating AB cycles resulted in films 22 ± 1 nm thick by ellipsometry (J. A. Woollam M2000U, Keck II, NUANCE Center, Northwestern University), suggesting a growth rate of approximately 0.45 Å per cycle. Titanium(IV) oxide flat films were grown under identical reactor conditions, but with precursor exposures (which involve isolating the reaction chamber from vacuum) utilized for both the Ti and H_2O half-cycles. The A half-cycle consisted of a 0.1 s pulse titanium precursor, a 8 s exposure, and an 8 s N_2 purge; the B half-cycle replaced the Ti

pulse with a 0.02 s water pulse but was otherwise identical. 900 AB cycles resulted in a ~ 30 nm film by ellipsometry suggesting a growth rate around 0.33 Å per cycle. Films that were annealed were heated in air to 500 °C over a period of 3 hours and held there for 30 minutes before being allowed to cool to room temperature.

6.2.3. X-ray Photoelectron Spectroscopy

XPS of the niobium(V) oxide films were collected on a Thermo Scientific ESCALAB 250Xi X-ray photoelectron spectrometer. The Nb 3d signal was referenced to adventitious carbon at 284.8 eV. The pass energy was 50 eV and the dwell time was 200 milliseconds.

6.2.4. Electrochemical setup

For all experiments, a platinum wire counter electrode and an aqueous Ag/AgCl in saturated KCl reference electrode were used. Metal oxide coated FTO glass served as the working electrode. Electrochemical impedance spectroscopy (EIS) was performed on a Solartron 1286 electrochemical interface coupled to a Solartron 1260 impedance/gain-phase analyzer. Impedance was measured from -0.55 V vs. reference to -0.85 V vs. reference in increments of 25 mV. The electrode was preconditioned at each potential for 60 seconds, with the exception of -0.55 V, where the conditioning lasted 300 s. The measured frequency range was 500 Hz to 0.05 Hz and the amplitude of the potential modulation was 10 mV. For CV measurements, a Solartron Analytical Modulab box with a 1MS/s potentiostat module was employed. The measured potential range was 2 V to -2 V vs. reference and the sweep rate was 150 mV per s. Electrolyte solutions consisted of either 1 N NaOH or KOH in deionized water or 0.2 M Na_2CO_3/$NaHCO_3$ buffer solution.

6.3. Results and Discussion

6.3.1. XPS and Oxidation State of Niobium in Oxide Thin Films

The Nb metal precursor used for ALD deposition is a Nb(V) species and no reducing reagents are present, therefore it is anticipated that the deposited film will be Nb_2O_5. XPS confirmed this is indeed the case. Figure 6.1 shows the Nb 3d XPS spectra of as deposited and annealed Nb_2O_5 films. In both cases, peaks are observed at 209.7 eV and 206.9 eV, which correspond to Nb $3d_{3/2}$ and Nb $3d_{5/2}$, respectively, and confirm the presence of Nb^{5+}.[54] Therefore, it is concluded that Nb_2O_5 is the most likely phase of the deposited metal oxide.

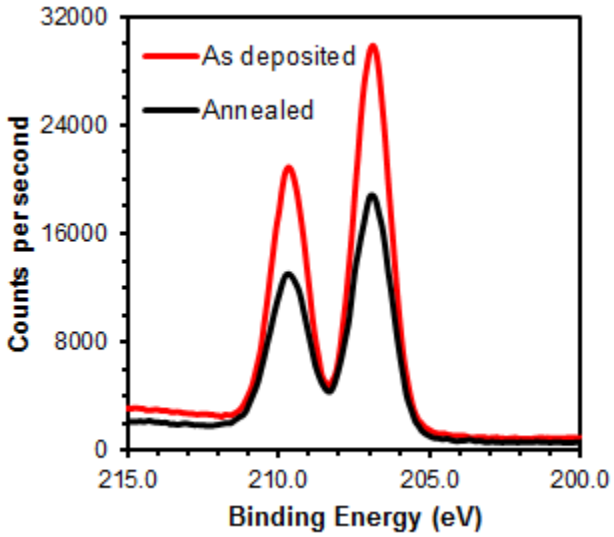

Figure 6.1. XPS Spectra of Nb 3d Region for Nb(V) Oxide Films.
XPS spectra in Nb 3d region of Nb(V) oxide films as deposited (red) and annealed at 500 °C (black). The peak locations of 209.7 eV (Nb $3d_{3/2}$) and 206.9 eV (Nb $3d_{5/2}$) are indicative of Nb^{5+}.

Previous studies of the deposition of Nb_2O_5 by ALD using tris(diethylamino)(*tert*-butylimido)niobium(V) have found that heat treatment at 500 °C is insufficient for crystalline growth during annealing.[153] Thus, the air "annealing" process likely fills oxygen vacancies from

the deposition process as opposed to engendering crystal growth. However, the oxygen vacancies will not be completely filled by air annealing, so the actual empirical formula of the Nb_2O_5 films studied will oxygen deficient (Nb_2O_{5-x}, where x is likely <0.1). Generally, it is these oxygen deficiencies that are responsible for Nb_2O_5 conductivity,[154, 155] but, for the purposes of this work, the material will still be referred to as Nb_2O_5.

6.3.2. Cyclic Voltammetry of Nb_2O_5 Thin Films

Cyclic voltammetry was performed as an initial characterization of the Nb_2O_5 thin films. For comparison, CV was also done on ALD thin films of TiO_2. Figure 6.2 shows CVs from 2 V to -2 V versus Ag/AgCl in saturated KCl at a sweep rate of 150 mV/s.

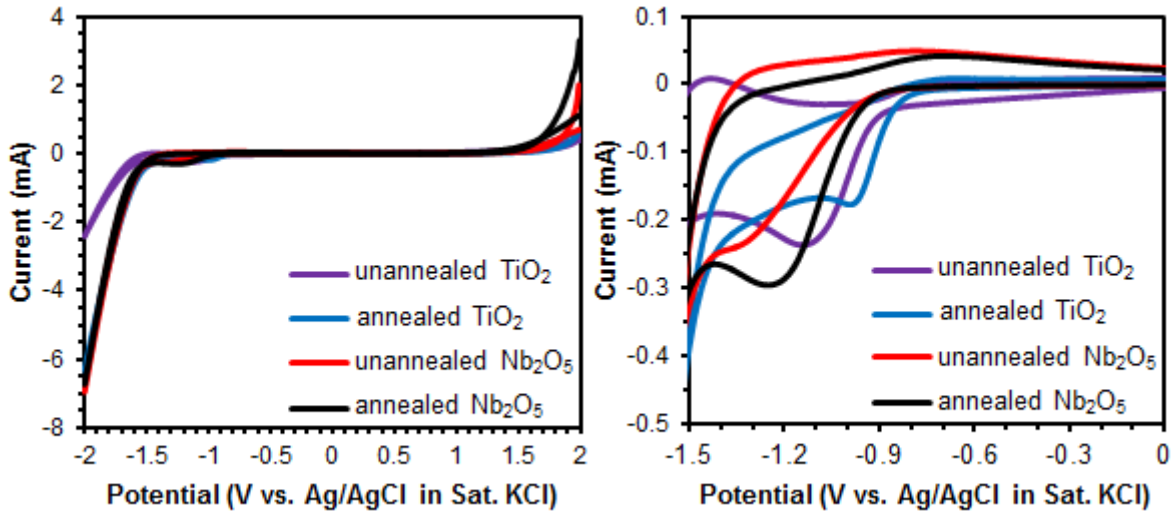

Figure 6.2. CVs of TiO_2 and Nb_2O_5 Thin Films.
CVs were performed in aqueous 1 M NaOH sweeping from 2 V to -2 V versus Ag/AgCl in saturated KCl at a sweep rate of 150 mV/s. Left: full sweep window. Right: Enlarged version of right to show features between 0 V and -1.5 V.

Both TiO_2 and Nb_2O_5 films show the expected lack of features over a large portion of the scanned region due to their semiconducting nature (see Figure 6.2 left). As aqueous NaOH is the

electrolyte, catalytic waves for water reduction/hydroxide oxidation are present at both extremes of applied potentials. Of particular note are the small current onset features observed for all films in the -1 V region, before the onset of (likely) water reduction. Figure 6.2 right is enlarged to highlight these features as they are indicative of the E_{CB} location of the films studied. As mentioned above, negligible charge is expected to flow from these films inside the band gap (note these experiments were conducted in ambient light at room temperature, so some electrons may be excited into the CB in these circumstances). As expected, a clear difference in current onset between Nb_2O_5 and TiO_2 is visible, with both metal oxides following the trend of annealed films having a more positive onset than unannealed films.

The variance in shape of the four CV traces makes determining an exact onset difficult. For simplicity, the potential at two separate current amplitudes was selected for comparison. This is depicted graphically in Figure 6.3.

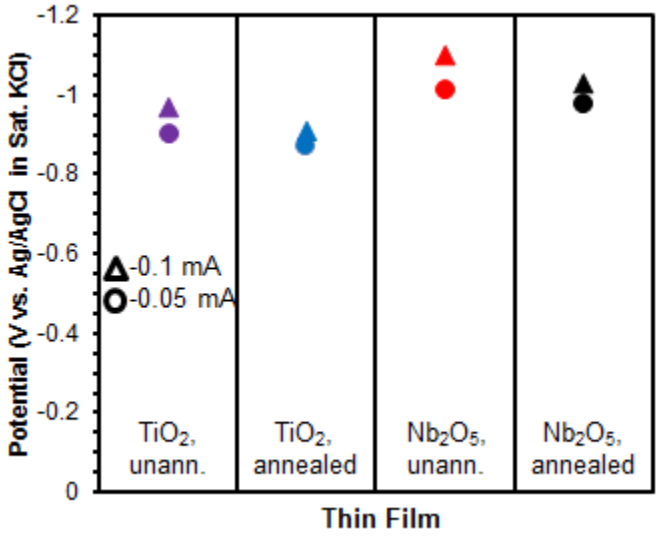

Figure 6.3. Graphical Representation of Onset Potential for TiO_2 and Nb_2O_5 Films by CV. The potentials selected are the potential at which certain current thresholds are met. Triangles represent the potential at -0.1 mA, and circles represent the potential at -0.05 mA.

The current amplitudes selected for comparison were -0.05 mA and -0.1 mA. The slanted baseline of the unannealed TiO_2 sample made selections closer to 0 mA difficult. Thus, while the derived current onset from this method is not precise, Figure 6.3 provides a reasonable comparison between the four types of films. Two separate current amplitudes are used to demonstrate the trend remains consistent, with the possible exception of unannealed Nb_2O_5, as evidenced by its differing slope in Figure 6.2. Note that the geometric surface area was constant across all measurements and the nature of film growth by ALD makes any surface roughness in the FTO consistent across all films, so these factors should have little effect on the measured current amplitudes. The potential values are presented in Table 6.1.

Table 6.1. Potential at Specified Current Amplitude for TiO_2 and Nb_2O_5 Film CVs.

V vs. Ag/AgCl in Sat. KCl	Unannealed TiO_2	Annealed TiO_2	Unannealed Nb_2O_5	Annealed Nb_2O_5
at -0.05 mA	-0.904	-0.869	-1.013	-0.978
at -0.1 mA	-0.968	-0.909	-1.099	-1.028

The onset potentials are around 100 mV more negative for Nb_2O_5 than for TiO_2 for both unannealed and annealed films, a difference that correlates well with the literature.[152, 156] Also of note is the ~ 60 mV difference in potential on the same film for different current amplitudes, meaning the choice of what value of current constitutes "onset" has a clear effect on the potential value. Thus, while the general trend in E_{CB} between Nb_2O_5 and TiO_2 might be gleaned from CV measurements, a more precise E_{CB} is difficult to extract. Thus, electrochemical impedance spectroscopy was employed in conjunction with the Mott-Schottky equation to determine the E_{CB} of ALD Nb_2O_5.

6.3.3. Electrochemical Impedance Spectroscopy of Nb_2O_5 and TiO_2 Thin Films

EIS was performed on both annealed and unannealed TiO_2 and Nb_2O_5 films in 1 M aqueous hydroxide solution. The Nyquist plots are presented in Figure 6.4.

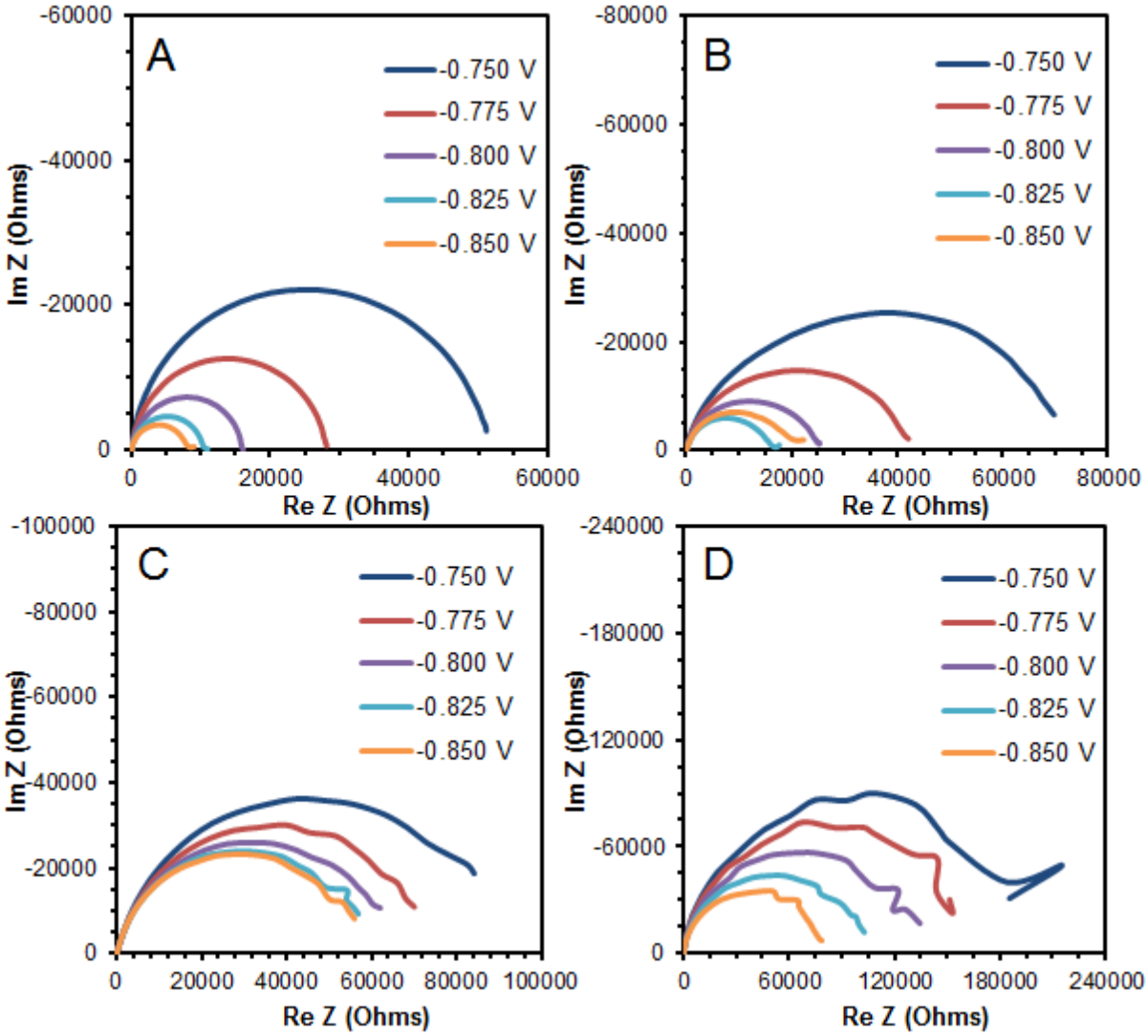

Figure 6.4. Nyquist Plots of Annealed and Unannealed TiO_2 and Nb_2O_5 Thin Films. Representative Nyquist plots at potentials relevant to Mott-Schottky analysis for A)unannealed TiO_2, B) annealed TiO_2, C) unannealed Nb_2O_5, and D) annealed Nb_2O_5, all in 1 M aqueous hydroxide solution. The potentials -0.750 V through -0.850 volts (all versus Ag/AgCl in saturated KCl) were chosen as the Mott-Schottky plots were linear in this region for all films. Note the large difference in scale for each plot.

For clarity, only the potentials that result in linear Mott-Schottky plots (see section 6.3.4) are shown in Figure 6.4. Immediately apparent is the decrease in semicircle diameter as the potential is increased in energy (*i.e.*, shifted to more negative values versus reference). From the above Nyquist plots were extracted charge transfer resistances and electrode capacitances by fitting the plots to the simple equivalent circuit shown in Figure 6.5.

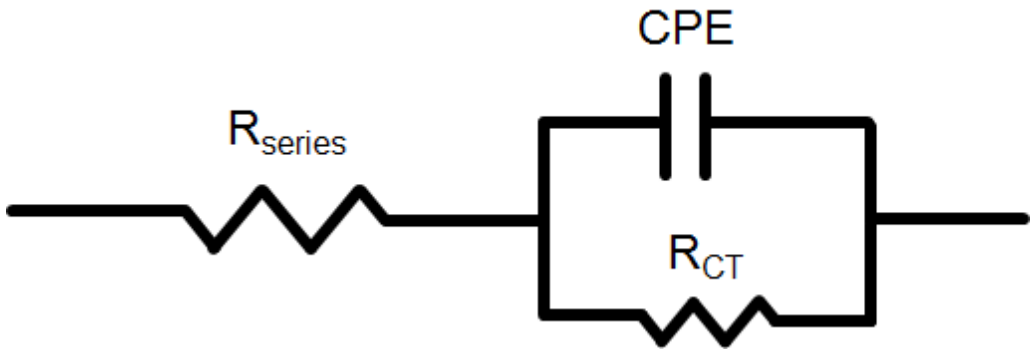

Figure 6.5. Equivalent Circuit for Fitting EIS Data.
The simple equivalent circuit used in all fittings of EIS data. A constant phase element (CPE) is used in place of a standard capacitor. The CPE is in parallel with a resistor (R_{CT}) representing the charge transfer resistance (*i.e.*, the resistance to electron transfer from the electrode to the solution). The R_{series} element represents the inherent resistance of both the solution and the FTO film.

Note that the equivalent circuit in Figure 6.5 uses a constant phase element (CPE) in place of a simple capacitor to account for any non-ideality in the capacitance behavior of the electrode. The fits result in values for capacitance and charge transfer resistance that scale expectedly with the diameters of the semicircles in the Nyquist plots above. These derived capacitance values were used in the extraction of the E_{FB} in the following section.

6.3.4. Mott-Schottky Analysis of Nb_2O_5 and TiO_2 Thin Films

Mott-Schottky treatment of metal oxide flat films can provide the location of the flat-band potential, E_{FB}, of the semiconductor from experimental measurements of capacitance provided

the semiconductor/electrolyte interface meets the necessary assumptions.[157, 158] If the assumptions are met incompletely, the Mott-Schottky treatment is still applicable, but some error may be introduced into a calculated E_{FB}. While it was not verified completely that this system met all assumptions, the Mott-Schottky treatment was nevertheless applied.[52, 148, 159-161] The Mott-Schottky equation can be written as in Equation 6.1:

$$\frac{A^2}{C^2} = \frac{2}{q\varepsilon\varepsilon_o N}\left(E - E_{FB} - \frac{kT}{q}\right) \qquad (6.1)$$

where A is the exposed surface area, C is the film capacitance, q is the fundamental charge of an electron, ε is the dielectric constant of the studied material (here taken to be 55 for TiO_2[52] and 41 for Nb_2O_5[162, 163]), ε_o is the permittivity of free space, N is the donor density of the semiconductor, E is the applied potential, k is Boltzmann's constant, and T is temperature. [52, 159] Thus, a plot of applied voltage versus A^2/C^2 should result in a straight line with the E_{FB} being equal to the x-intercept minus kT/q. If the dielectric constant of the material is known, the donor density N can also be calculated from the slope of the line. With these values in hand, the E_{CB} can be calculated according to Equation 6.2:

$$E_{CB} = q\left(E_{FB} - \frac{kT}{q}\ln\frac{N_C^*}{N}\right) \qquad (6.2)$$

where N_C^* is the effective density of electronic states in the semiconductor and is defined by Equation 6.3:

$$N_C^* = 2*\left(\frac{2\pi m_e^* kT}{h^2}\right)^{3/2} \qquad (6.3)$$

with m_e^* being the effective mass of the electron. For this work, the effective mass of the electron in TiO_2 is assumed to be 1.8 times the electron's resting mass[164] and in Nb_2O_5 2.3 times the resting mass.[165]

Armed with equations 6.1-6.3, Mott-Schottky plots were prepared from fitting the EIS data described in Section 6.3.3 for Nb_2O_5 and TiO_2 films fabricated by ALD. These plots are shown in Figure 6.6.

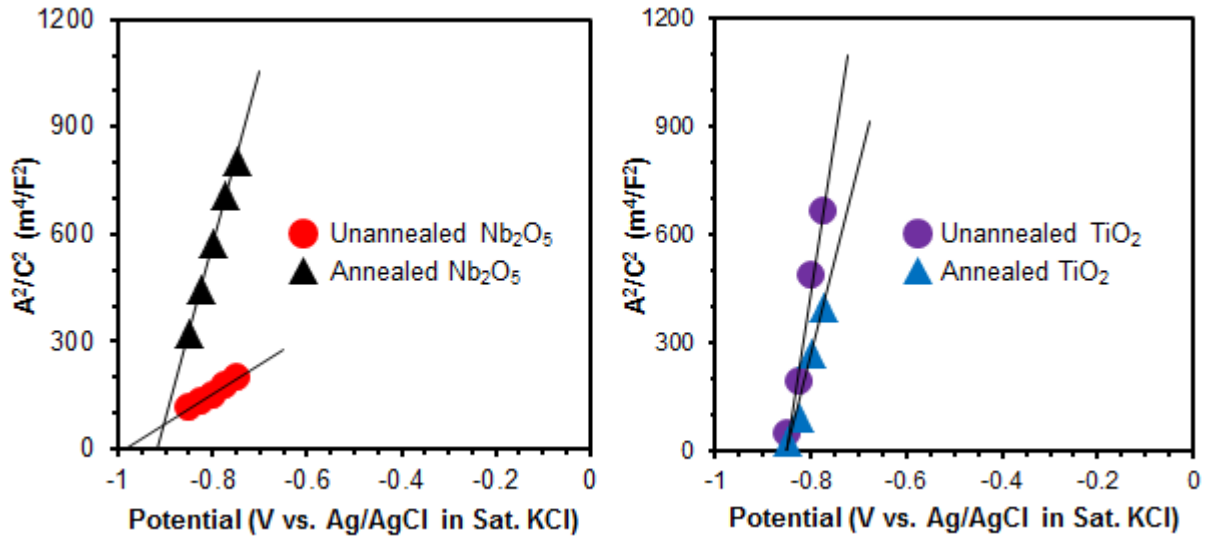

Figure 6.6. Mott-Schottky Plots of unannealed and annealed Nb_2O_5 and TiO_2 Electrodes. Mott-Schottky plots for Nb_2O_5 (left) and TiO_2 (right), annealed (triangles) and unannealed (circles), electrodes. The plots were constructed via fitting the Nyquist plots in Figure 6.4 to the equivalent circuit in Figure 6.5. Trend lines are forecast to show the approximate intercept with the x-axis.

While capacitance values were collected across the entire potential range of -0.55 V to -0.85 V, only the linear portion of the resulting Mott-Schottky plots are shown in Figure 6.6. From Equation 6.1, the E_{FB} is the x-intercept minus kT/q. Since all the measurements took place at room temperature, kT/q is a constant 26 mV for all films. A comparison of the x-intercept of the trend lines shown in Figure 6.6 thus gives the trend in E_{FB} across the films measured. Both TiO_2

films intercept the x-axis around -0.85 V, suggesting E_{FB} energies (when kT/q is subtracted) of ~ -0.88 V for both unannealed and annealed TiO_2. The Nb_2O_5 films both have x-intercepts higher in energy than TiO_2, giving approximate E_{FB} energies of -1.1 V and -0.94 V for unannealed and annealed Nb_2O_5, respectively. Note that these E_{FB} value are representative of the larger data set, with the average calculated E_{FB} energies and the associated errors shown in Table 6.2. However, the trend shown above holds for the calculated averages, and the E_{FB} differences are of the approximate magnitude previously described for TiO_2 and Nb_2O_5 fabricated by various methods.[152, 156]

Additional information about the electronic structure of the TiO_2 and Nb_2O_5 films, including donor density N and E_{CB}, can be extracted from the slope of the trend lines in Figure 6.6. From Equation 6.1, N is inversely related to the slope of the line, so steeper slopes in the Mott-Schottky plots correspond to lower donor densities. The calculated donor density in turn allows for the calculation of E_{CB} via Equation 6.2. The average values of E_{FB}, N, and E_{CB} are contained in Table 6.2 for all films in this study. Table 6.2 also shows the thickness of the space-charge layer W at -0.55 V as calculated by Equation 6.4:

$$W = \sqrt{\frac{2\varepsilon\varepsilon_o \Delta E}{qN}} \qquad (6.4)$$

where ΔE is the potential drop across the electrode, taken here to be the difference between the applied potential of -0.55 V and the E_{FB} of the electrode. Calculation of the SCL assured that the studied films were thick enough to avoid the added complexity that would arise from the SCL extending into the FTO substrate.

Table 6.2. Donor Density, E_{FB}, and E_{CB} for TiO_2 and Nb_2O_5 Films.

	[a]Unannealed TiO_2	[a]Annealed TiO_2	[b]Unannealed Nb_2O_5	[b]Annealed Nb_2O_5
N_c^* (m^{-3})	6.06×10^{25}	6.06×10^{25}	8.93×10^{25}	8.93×10^{25}
N (m^{-3})	$3.5 \times 10^{24} \pm 5.0 \times 10^{23}$	$1.4 \times 10^{25} \pm 9.1 \times 10^{24}$	$1.1 \times 10^{26} \pm 6.7 \times 10^{25}$	$6.66 \times 10^{24} \pm 6.0 \times 10^{23}$
[c]E_{FB} (V)	-0.888 ± 0.006	-0.913 ± 0.013	-1.092 ± 0.035	-0.941 ± 0.001
[c]E_{CB} (V)	-0.963 ± 0.006	-0.974 ± 0.021	-1.101 ± 0.028	-1.008 ± 0.003
[d]Space Charge Layer (nm)	25.4 ± 2.0	23.5 ± 4.6	7.1 ± 1.9	16.5 ± 0.8

[a]Average of 5 separate films
[b]Average of 3 separate films
[c]Versus Ag/AgCl in saturated KCl
[d]Calculated at -0.55 V, the smallest potential examined and energy at which the SCL is thickest

Though N_c^* is calculated from constants (see Equation 6.3), the differing effective mass of electrons in the two materials results in the different values. Perhaps most importantly from Table 6.2, the E_{CB} of Nb_2O_5 is higher than that of TiO_2 in all cases, which was anticipated based on literature.[54, 56, 151, 152, 156, 166] Because of their role in determining the energy of E_{CB} via Equation 6.2, the calculated donor densities N are of particular interest. It was anticipated that heat treatment of the films would decrease the donor density as oxygen vacancies, and thus electron trap sites, from the ALD process would be filled by annealing in air.[167] This was observed for Nb_2O_5, but the opposite effect was observed for TiO_2. Annealing temperature was not optimized for this study, so this observation could be the result of using an annealing temperature in air that resulted in more oxygen vacancies for the TiO_2 film.[168-170] The opposite trend in donor density before and after annealing for TiO_2 and Nb_2O_5 leads to an opposite trend in E_{CB} as well; annealing lowers the E_{CB} for Nb_2O_5 while raising the E_{CB} for TiO_2. Despite this, E_{CB} (as well as E_{FB}) is higher in energy for Nb_2O_5 across all electrodes. However, the difference in E_{CB} reported here between annealed films of TiO_2 and Nb_2O_5 is smaller in magnitude than typically observed for other systems (~ 30 mV compared to 80-100 mV elsewhere).[152, 156] One possible explanation may be found in the dielectric constants and effective electron masses used

for TiO_2 and Nb_2O_5. The actual dielectric and effective masses of the fabricated films were not measured and may be different.

EIS of select Nb_2O_5 films was also measured in pH 10.8 Na_2CO_3/$NaHCO_3$ aqueous buffer. The E_{CB} of metal oxide films is known to shift by approximately -60 mV/pH unit, meaning a change in pH from pH = 5 to pH = 10 would result in a -300 mV change in E_{CB} (with more negative E_{CB} values corresponding to higher E_{CB}).[171] Thus, upon moving from pH 13.6 to pH 10.8, an approximately 180 mV change in E_{CB} is expected. Figure 6.7 depicts the Mott-Schottky plots obtained from EIS measurements in the aforementioned buffer solution.

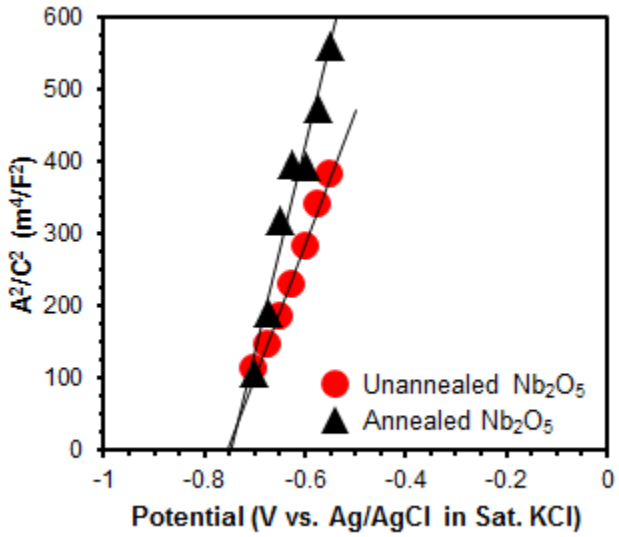

Figure 6.7. Mott-Schottky Plot for Nb_2O_5 Electrodes in pH 10.8 Aqueous Buffer.
Linear portions of the Mott-Schottky plots for unannealed (red circles) and annealed (black triangles) Nb_2O_5 electrodes in pH 10.8 Na_2CO_3/$NaHCO_3$ aqueous buffer solution. Plots were constructed via fitting of EIS data (not shown) to the equivalent circuit in Figure 6.5.

The data shown in Figure 6.7 results in calculated donor densities N of 1.9×10^{25} m^{-3} and 1.2×10^{25} m^{-3}, E_{FB} of -0.781 V and -0.773 V, and E_{CB} of -0.822 and -0.824 V for unannealed and annealed Nb_2O_5, respectively (SCL thickness was ~8 nm for both). While the trend between

unannealed and annealed electrodes has essentially disappeared, the E_{CB} values of ~ -0.820 V in pH 10.8 buffer are ~180 mV below the annealed Nb_2O_5, as expected. The disappearance of the annealed versus unannealed trend apparent in 1 M aqueous hydroxide is curious but was not explored further. It is possible that the carbonate buffer may be having some effect on surface states that was not present with the 1 M hydroxide, or vice versa.[172] Regardless, the expected decrease in E_{CB} in buffer solution lends credence to the use of Mott-Schottky analysis for these electrodes.

6.4. Conclusions

While there is some variance in the calculated values of N, E_{FB}, and E_{CB} across experiments, all data clearly points to a Nb_2O_5 E_{CB} that is higher in energy than that of TiO_2. While this was generally expected based on the previous literature, it is verified here specific to the ALD fabrication method. However, the observed difference is either smaller or larger in magnitude than expected, depending on whether annealed or unannealed Nb_2O_5 is used for comparison. If ALD Nb_2O_5 were to be employed as an insulating layer in DSC or perovskite solar cells, it would most likely be in the amorphous form. Since it is reasonable to assume the results obtained in 1 M aqueous hydroxide are more reliable than those in buffer based on the effect of surface and near surface hydration of metal oxides and the effect of ion penetration into the film,[172] the unannealed Nb_2O_5 films are assumed to have higher E_{CB}. This is a significant advantage in efforts to improve photovoltages in photovoltaic devices.

References

(1) *International Energy Outlook 2016 with Projections to 2040*; DOE/EIA-0484(2016); U.S. Energy Information Administration: Online, May 2016.

(2) IPCC, 2014: *Climate Change 2014: Mitigation of Climate Change. Contribution of Working Group III to the Fifth Assessment Report of the Intergovernmental Panel on Climate Change* [Edenhofer, O., R. Pichs-Madruga, Y. Sokona, E. Farahani, S. Kadner, K. Seyboth, A. Adler, I. Baum, S. Brunner, P. Eickemeier, B. Kriemann, J. Savolainen, S. Schlömer, C. von Stechow, T. Zwickel and J.C. Minx (eds.)]. Cambridge University Press, Cambridge, United Kingdom and New York, NY, USA.

(3) Lewis, S. L. The Paris Agreement Has Solved a Troubling Problem. *Nature* **2016,** *532*, 283.

(4) Smith, P.; Davis, S. J.; Creutzig, F.; Fuss, S.; Minx, J.; Gabrielle, B.; Kato, E.; Jackson, R. B.; Cowie, A.; Kriegler, E.; van Vuuren, D. P.; Rogelj, J.; Ciais, P.; Milne, J.; Canadell, J. G.; McCollum, D.; Peters, G.; Andrew, R.; Krey, V.; Shrestha, G.; Friedlingstein, P.; Gasser, T.; Grubler, A.; Heidug, W. K.; Jonas, M.; Jones, C. D.; Kraxner, F.; Littleton, E.; Lowe, J.; Moreira, J. R.; Nakicenovic, N.; Obersteiner, M.; Patwardhan, A.; Rogner, M.; Rubin, E.; Sharifi, A.; Torvanger, A.; Yamagata, Y.; Edmonds, J.; Yongsung, C. Biophysical and Economic Limits to Negative CO_2 Emissions. *Nature Clim. Change* **2016,** *6*, 42-50.

(5) Tsao, J.; Lewis, N.; Crabtree, G. Solar FAQs. 2005.

(6) O'Regan, B.; Gratzel, M. A Low-Cost, High-Efficiency Solar Cell Based on Dye-Sensitized Colloidal TiO_2 Films. *Nature* **1991,** *353*, 737-740.

(7) Lapides, A. M.; Sherman, B. D.; Brennaman, M. K.; Dares, C. J.; Skinner, K. R.; Templeton, J. L.; Meyer, T. J. Synthesis, Characterization, and Water Oxidation by a Molecular Chromophore-Catalyst Assembly Prepared by Atomic Layer Deposition. The "Mummy" Strategy. *Chem. Sci.* **2015,** *6*, 6398-6406.

(8) Kamire, R. J.; Majewski, M. B.; Hoffeditz, W. L.; Phelan, B. T.; Farha, O. K.; Hupp, J. T.; Wasielewski, M. R. Photodriven Hydrogen Evolution by Molecular Catalysts Using Al_2O_3-Protected Perylene-3,4-Dicarboximide on NiO Electrodes. *Chem. Sci.* **2017**.

(9) Swierk, J. R.; McCool, N. S.; Nemes, C. T.; Mallouk, T. E.; Schmuttenmaer, C. A. Ultrafast Electron Injection Dynamics of Photoanodes for Water-Splitting Dye-Sensitized Photoelectrochemical Cells. *J. Phys. Chem. C* **2016,** *120*, 5940-5948.

(10) Swierk, J. R.; Méndez-Hernández, D. D.; McCool, N. S.; Liddell, P.; Terazono, Y.; Pahk, I.; Tomlin, J. J.; Oster, N. V.; Moore, T. A.; Moore, A. L.; Gust, D.; Mallouk, T. E. Metal-Free Organic Sensitizers for Use in Water-Splitting Dye-Sensitized Photoelectrochemical Cells. *Proc. Natl. Acad. Sci. U.S.A.* **2015,** *112*, 1681-1686.

(11) Alibabaei, L.; Sherman, B. D.; Norris, M. R.; Brennaman, M. K.; Meyer, T. J. Visible Photoelectrochemical Water Splitting into H_2 and O_2 in a Dye-Sensitized Photoelectrosynthesis Cell. *Proc. Natl. Acad. Sci. U.S.A.* **2015,** *112*, 5899-5902.

(12) Swierk, J. R.; Mallouk, T. E. Design and Development of Photoanodes for Water-Splitting Dye-Sensitized Photoelectrochemical Cells. *Chem. Soc. Rev.* **2013,** *42*, 2357-2387.

(13) Grätzel, M. Solar Energy Conversion by Dye-Sensitized Photovoltaic Cells. *Inorg. Chem.* **2005,** *44*, 6841-6851.

(14) Nazeeruddin, M. K.; Kay, A.; Rodicio, I.; Humphry-Baker, R.; Mueller, E.; Liska, P.; Vlachopoulos, N.; Graetzel, M. Conversion of Light to Electricity by *cis*-X_2Bis(2,2'-bipyridyl-4,4'-dicarboxylate)ruthenium(II) Charge-Transfer Sensitizers (X = Cl^-, Br^-, I^-, CN^-, and SCN^-) on Nanocrystalline TiO_2 Electrodes. *J. Am. Chem. Soc.* **1993,** *115*, 6382-6390.

(15) Li, L. L.; Diau, E. W. G. Porphyrin-Sensitized Solar Cells. *Chem. Soc. Rev.* **2013,** *42*, 291-304.

(16) Yella, A.; Lee, H.-W.; Tsao, H. N.; Yi, C.; Chandiran, A. K.; Nazeeruddin, M. K.; Diau, E. W.-G.; Yeh, C.-Y.; Zakeeruddin, S. M.; Grätzel, M. Porphyrin-Sensitized Solar Cells with Cobalt (II/III)–Based Redox Electrolyte Exceed 12 Percent Efficiency. *Science* **2011,** *334*, 629-634.

(17) Daeneke, T.; Kwon, T.-H.; Holmes, A. B.; Duffy, N. W.; Bach, U.; Spiccia, L. High-Efficiency Dye-Sensitized Solar Cells with Ferrocene-Based Electrolytes. *Nat. Chem.* **2011,** *3*, 211-215.

(18) Scrascia, A.; De Marco, L.; Laricchia, S.; Picca, R. A.; Carlucci, C.; Fabiano, E.; Capodilupo, A. L.; Della Sala, F.; Gigli, G.; Ciccarella, G. Fluorine-Thiophene-Substituted Organic Dyes for Dye Sensitized Solar Cells. *J. Mater. Chem. A* **2013,** *1*, 11909-11921.

(19) Ren, X.; Jiang, S.; Cha, M.; Zhou, G.; Wang, Z.-S. Thiophene-Bridged Double D-Π-a Dye for Efficient Dye-Sensitized Solar Cell. *Chem. Mater.* **2012,** *24*, 3493-3499.

(20) Cameron, P. J.; Peter, L. M.; Hore, S. How Important Is the Back Reaction of Electrons Via the Substrate in Dye-Sensitized Nanocrystalline Solar Cells? *J. Phys. Chem. B* **2005,** *109*, 930-936.

(21) Kavan, L.; Tétreault, N.; Moehl, T.; Grätzel, M. Electrochemical Characterization of TiO_2 Blocking Layers for Dye-Sensitized Solar Cells. *J. Phys. Chem. C* **2014,** *118*, 16408-16418.

(22) Hagfeldt, A.; Boschloo, G.; Sun, L.; Kloo, L.; Pettersson, H. Dye-Sensitized Solar Cells. *Chem. Rev.* **2010,** *110*, 6595-6663.

(23) Carli, S.; Busatto, E.; Caramori, S.; Boaretto, R.; Argazzi, R.; Timpson, C. J.; Bignozzi, C. A. Comparative Evaluation of Catalytic Counter Electrodes for Co(III)/(II) Electron Shuttles in Regenerative Photoelectrochemical Cells. *J. Phys. Chem. C* **2013,** *117*, 5142-5153.

(24) Sapp, S. A.; Elliott, C. M.; Contado, C.; Caramori, S.; Bignozzi, C. A. Substituted Polypyridine Complexes of Cobalt(II/III) as Efficient Electron-Transfer Mediators in Dye-Sensitized Solar Cells. *J. Am. Chem. Soc.* **2002,** *124*, 11215-11222.

(25) Kang, D.-Y.; Lee, Y.; Cho, C.-Y.; Moon, J. H. Inverse Opal Carbons for Counter Electrode of Dye-Sensitized Solar Cells. *Langmuir* **2012,** *28*, 7033-7038.

(26) Stefik, M.; Yum, J.-H.; Hu, Y.; Gratzel, M. Carbon-Graphene Nanocomposite Cathodes for Improved Co(II/III) Mediated Dye-Sensitized Solar Cells. *J. Mater. Chem. A* **2013,** *1*, 4982-4987.

(27) Yum, J.-H.; Baranoff, E.; Kessler, F.; Moehl, T.; Ahmad, S.; Bessho, T.; Marchioro, A.; Ghadiri, E.; Moser, J.-E.; Yi, C.; Nazeeruddin, M. K.; Grätzel, M. A Cobalt Complex Redox Shuttle for Dye-Sensitized Solar Cells with High Open-Circuit Potentials. *Nat. Commun.* **2012,** *3*, 631.

(28) Pringle, J. M.; Armel, V.; MacFarlane, D. R. Electrodeposited PEDOT-on-Plastic Cathodes for Dye-Sensitized Solar Cells. *Chem. Commun.* **2010,** *46*, 5367-5369.

(29) Prasittichai, C.; Avila, J. R.; Farha, O. K.; Hupp, J. T. Systematic Modulation of Quantum (Electron) Tunneling Behavior by Atomic Layer Deposition on Nanoparticulate SnO2 and TiO2 Photoanodes. *J. Am. Chem. Soc.* **2013,** *135*, 16328-16331.

(30) Hamann, T. W.; Farha, O. K.; Hupp, J. T. Outer-Sphere Redox Couples as Shuttles in Dye-Sensitized Solar Cells. Performance Enhancement Based on Photoelectrode Modification Via Atomic Layer Deposition. *J. Phys. Chem. C* **2009,** *112*, 19756-19764.

(31) Prasittichai, C.; Hupp, J. T. Surface Modification of SnO_2 Photoelectrodes in Dye-Sensitized Solar Cells: Significant Improvements in Photovoltage Via Al_2O_3 Atomic Layer Deposition. *J. Phys. Chem. Lett.* **2010,** *1*, 1611-1615.

(32) Cao, F.; Oskam, G.; Meyer, G. J.; Searson, P. C. Electron Transport in Porous Nanocrystalline TiO_2 Photoelectrochemical Cells. *J. Phys. Chem.* **1996,** *100*, 17021-17027.

(33) Nakade, S.; Saito, Y.; Kubo, W.; Kitamura, T.; Wada, Y.; Yanagida, S. Influence of TiO_2 Nanoparticle Size on Electron Diffusion and Recombination in Dye-Sensitized TiO_2 Solar Cells. *J. Phys. Chem. B* **2003,** *107*, 8607-8611.

(34) Daeneke, T.; Mozer, A. J.; Kwon, T.-H.; Duffy, N. W.; Holmes, A. B.; Bach, U.; Spiccia, L. Dye Regeneration and Charge Recombination in Dye-Sensitized Solar Cells with Ferrocene Derivatives as Redox Mediators. *Energy Environ. Sci.* **2012,** *5*, 7090.

(35) Daeneke, T.; Mozer, A. J.; Uemura, Y.; Makuta, S.; Fekete, M.; Tachibana, Y.; Koumura, N.; Bach, U.; Spiccia, L. Dye Regeneration Kinetics in Dye-Sensitized Solar Cells. *J. Am. Chem. Soc.* **2012,** *134*, 16925-16928.

(36) Honsberg, C.; Bowden, S. Impact of Both Series and Shunt Resistance. http://pveducation.org/pvcdrom/solar-cell-operation/impact-of-both-series-and-shunt-resistance.

(37) Hao, F.; Dong, P.; Luo, Q.; Li, J.; Lou, J.; Lin, H. Recent Advances in Alternative Cathode Materials for Iodine-Free Dye-Sensitized Solar Cells. *Energy Environ. Sci.* **2013,** *6*, 2003-2019.

(38) National Renewable Energy Lab. Best Research Cell Efficiencies. http://www.nrel.gov/pv/assets/images/efficiency_chart.jpg.

(39) Boschloo, G.; Hagfeldt, A. Characteristics of the Iodide/Triiodide Redox Mediator in Dye-Sensitized Solar Cells. *Acc. Chem. Res.* **2009,** *42*, 1819-1826.

(40) Gregg, B. A.; Pichot, F.; Ferrere, S.; Fields, C. L. Interfacial Recombination Processes in Dye-Sensitized Solar Cells and Methods to Passivate the Interfaces. *J. Phys. Chem. B* **2001,** *105*, 1422-1429.

(41) Grätzel, M. Recent Advances in Sensitized Mesoscopic Solar Cells. *Acc. Chem. Res.* **2009,** *42*, 1788-1798.

(42) Peter, L. M. The GräTzel Cell: Where Next? *J. Phys. Chem. Lett.* **2011,** *2*, 1861-1867.

(43) Cong, J.; Yang, X.; Kloo, L.; Sun, L. Iodine/Iodide-Free Redox Shuttles for Liquid Electrolyte-Based Dye-Sensitized Solar Cells. *Energy Environ. Sci.* **2012,** *5*, 9180-9194.

(44) Hamann, T. W.; Jensen, R. A.; Martinson, A. B. F.; Van Ryswyk, H.; Hupp, J. T. Advancing Beyond Current Generation Dye-Sensitized Solar Cells. *Energy Environ. Sci.* **2008,** *1*, 66.

(45) Feldt, S. M.; Gibson, E. A.; Gabrielsson, E.; Sun, L.; Boschloo, G.; Hagfeldt, A. Design of Organic Dyes and Cobalt Polypyridine Redox Mediators for High-Efficiency Dye-Sensitized Solar Cells. *J. Am. Chem. Soc.* **2010,** *132*, 16714-16724.

(46) Feldt, S. M.; Wang, G.; Boschloo, G.; Hagfeldt, A. Effects of Driving Forces for Recombination and Regeneration on the Photovoltaic Performance of Dye-Sensitized Solar Cells Using Cobalt Polypyridine Redox Couples. *J. Phys. Chem. C* **2011,** *115*, 21500-21507.

(47) Klahr, B. M.; Hamann, T. W. Performance Enhancement and Limitations of Cobalt Bipyridyl Redox Shuttles in Dye-Sensitized Solar Cells. *J. Phys. Chem. C* **2009,** *113*, 14040-14045.

(48) Mathew, S.; Yella, A.; Gao, P.; Humphry-Baker, R.; CurchodBasile, F. E.; Ashari-Astani, N.; Tavernelli, I.; Rothlisberger, U.; Nazeeruddin, M. K.; Grätzel, M. Dye-Sensitized Solar Cells

with 13% Efficiency Achieved through the Molecular Engineering of Porphyrin Sensitizers. *Nat. Chem.* **2014,** *6*, 242-247.

(49) Saygili, Y.; Söderberg, M.; Pellet, N.; Giordano, F.; Cao, Y.; Muñoz-García, A. B.; Zakeeruddin, S. M.; Vlachopoulos, N.; Pavone, M.; Boschloo, G.; Kavan, L.; Moser, J.-E.; Grätzel, M.; Hagfeldt, A.; Freitag, M. Copper Bipyridyl Redox Mediators for Dye-Sensitized Solar Cells with High Photovoltage. *J. Am. Chem. Soc.* **2016,** *138*, 15087-15096.

(50) Cong, J.; Kinschel, D.; Daniel, Q.; Safdari, M.; Gabrielsson, E.; Chen, H.; Svensson, P. H.; Sun, L.; Kloo, L. Bis(1,1-bis(2-pyridyl)ethane)copper(I/II) as an Efficient Redox Couple for Liquid Dye-Sensitized Solar Cells. *J. Mater. Chem. A* **2016,** *4*, 14550-14554.

(51) Rorabacher, D. B. Electron Transfer by Copper Centers. *Chem. Rev.* **2004,** *104*, 651-697.

(52) Katz, M. J.; Vermeer, M. J.; Farha, O. K.; Pellin, M. J.; Hupp, J. T. Effects of Adsorbed Pyridine Derivatives and Ultrathin Atomic-Layer-Deposited Alumina Coatings on the Conduction Band-Edge Energy of TiO2 and on Redox-Shuttle-Derived Dark Currents. *Langmuir* **2013,** *29*, 806-814.

(53) Ondersma, J. W.; Hamann, T. W. Impedance Investigation of Dye-Sensitized Solar Cells Employing Outer-Sphere Redox Shuttles. *J. Phys. Chem. C* **2010,** *114*, 638-645.

(54) Chandiran, A. K.; Nazeeruddin, M. K.; Grätzel, M. The Role of Insulating Oxides in Blocking the Charge Carrier Recombination in Dye-Sensitized Solar Cells. *Adv. Funct. Mater.* **2014,** *24*, 1615-1623.

(55) Kogo, A.; Numata, Y.; Ikegami, M.; Miyasaka, T. Nb_2O_5 Blocking Layer for High Open-Circuit Voltage Perovskite Solar Cells. *Chem. Lett.* **2015,** *44*, 829-830.

(56) Sacco, A.; Di Bella, M. S.; Gerosa, M.; Chiodoni, A.; Bianco, S.; Mosca, M.; Macaluso, R.; Calì, C.; Pirri, C. F. Enhancement of Photoconversion Efficiency in Dye-Sensitized Solar Cells Exploiting Pulsed Laser Deposited Niobium Pentoxide Blocking Layers. *Thin Solid Films* **2015,** *574*, 38-42.

(57) Kim, H.-N.; Moon, J. H. Enhanced Photovoltaic Properties of Nb_2O_5-Coated TiO_2 3D Ordered Porous Electrodes in Dye-Sensitized Solar Cells. *ACS Appl. Mater. Interfaces* **2012,** *4*, 5821-5825.

(58) Son, H.-J.; Wang, X.; Prasittichai, C.; Jeong, N. C.; Aaltonen, T.; Gordon, R. G.; Hupp, J. T. Glass-Encapsulated Light Harvesters: More Efficient Dye-Sensitized Solar Cells by Deposition of Self-Aligned, Conformal, and Self-Limited Silica Layers. *J. Am. Chem. Soc.* **2012,** *134*, 9537-9540.

(59) Son, H.-J.; Prasittichai, C.; Mondloch, J. E.; Luo, L.; Wu, J.; Kim, D. W.; Farha, O. K.; Hupp, J. T. Dye Stabilization and Enhanced Photoelectrode Wettability in Water-Based Dye-

Sensitized Solar Cells through Post-Assembly Atomic Layer Deposition of TiO_2. *J. Am. Chem. Soc.* **2013,** *135*, 11529-11532.

(60) Son, H.-J.; Kim, C. H.; Kim, D. W.; Jeong, N. C.; Prasittichai, C.; Luo, L.; Wu, J.; Farha, O. K.; Wasielewski, M. R.; Hupp, J. T. Post-Assembly Atomic Layer Deposition of Ultrathin Metal-Oxide Coatings Enhances the Performance of an Organic Dye-Sensitized Solar Cell by Suppressing Dye Aggregation. *ACS Appl. Mater. Interfaces* **2015,** *7*, 5150-5159.

(61) Bisquert, J.; Cahen, D.; Hodes, G.; Rühle, S.; Zaban, A. Physical Chemical Principles of Photovoltaic Conversion with Nanoparticulate, Mesoporous Dye-Sensitized Solar Cells. *J. Phys. Chem. B* **2004,** *108*, 8106-8118.

(62) Hardin, B. E.; Snaith, H. J.; McGehee, M. D. The Renaissance of Dye-Sensitized Solar Cells. *Nat. Photonics* **2012,** *6*, 162-169.

(63) Hamann, T. W. The End of Iodide? Cobalt Complex Redox Shuttles in DSSCs. *Dalton Trans.* **2012,** *41*, 3111-3115.

(64) Feldt, S. M.; Gibson, E. A.; Gabrielsson, E.; Sun, L.; Boschloo, G.; Hagfeldt, A. Design of Organic Dyes and Cobalt Polypyridine Redox Mediators for High-Efficiency Dye-Sensitized Solar Cells. *J. Am. Chem. Soc.* **2010,** *132*, 16714-16724.

(65) Bai, Y.; Yu, Q.; Cai, N.; Wang, Y.; Zhang, M.; Wang, P. High-Efficiency Organic Dye-Sensitized Mesoscopic Solar Cells with a Copper Redox Shuttle. *Chem. Commun.* **2011,** *47*, 4376-4378.

(66) Hattori, S.; Wada, Y.; Yanagida, S.; Fukuzumi, S. Blue Copper Model Complexes with Distored Tetragonal Geometry Acting as Effective Electron-Transfer Mediators in Dye-Sensitized Solar Cells. *J. Am. Chem. Soc.* **2005,** *127*, 9648-9654.

(67) Li, T. C.; Spokoyny, A. M.; She, C.; Farha, O. K.; Mirkin, C. A.; Marks, T. J.; Hupp, J. T. Ni(III)/(IV) Bis(Dicarbollide) as a Fast, Noncorrosive Redox Shuttle for Dye-Sensitized Solar Cells. *J. Am. Chem. Soc.* **2012,** *132*, 4580-4582.

(68) Wang, M.; Chamberland, N.; Breau, L.; Moser, J.-E.; Humphry-Baker, R.; Marsan, B.; Zakeeruddin, S. M.; Graetzel, M. An Organic Redox Electrolyte to Rival Triiodide/Iodide in Dye-Sensitized Solar Cells. *Nat. Chem.* **2010,** *2*, 385.

(69) Sakamoto, H.; Igarashi, S.; Uchida, M.; Niume, K.; Nagai, M. Highly Efficient All Solid State Dye-Sensitized Solar Cells by the Specific Interaction of Cui with Ncs Groups II. Enhancement of the Photovoltaic Characteristics. *Org. Electron.* **2012,** *13*, 514-518.

(70) Hsu, C. Y.; Chen, Y. C.; Lin, R. Y.; Ho, K. C.; Lin, J. T. Solid-State Dye-Sensitized Solar Cells Based on Spirofluorene (Spiro-OMeTAD) and Arylamines as Hole Transporting Materials. *Phys. Chem. Chem. Phys.* **2012,** *14*, 14099-14109.

(71) Karlin, K. D.; Yandell, J. K. Redox Behavior of Blue Copper Model Complexes. Reodx Potentials and Electron-Transfer Kinetics of Some Copper(II)-Copper(I) Complexes with Nitrogen and Thioether Donors. *Inorg. Chem.* **1984,** *23*, 1184-1188.

(72) Davies, K. M.; Whyte, K. D.; Liebermann Jr, J.; Mahr, J. A. Effect of Solvent on the Stability and Electron-Transfer Kinetics of 1,8-Bis(2-Pyridyl)-3,6-Dithiaether Copper(II). *Polyhedron* **1991,** *10*, 1647-1651.

(73) Davies, K. M.; Whyte, K. D.; Gilbert, A. H. Electrolyte Effects in Electron Transfer Reactions of 1,8-Bis(2-Pyridyl)-3,6-Dithiaoctane Copper(II) with Ferrocene in Acetonitrile. Specific Rate Enhancement by Tetrafluoroborate Ion. *Inorg. Chim. Acta* **1990,** *177*, 121-126.

(74) Mara, M. W.; Bowman, D. N.; Buyukcakir, O.; Shelby, M. L.; Haldrup, K.; Huang, J.; Harpham, M. R.; Stickrath, A. B.; Zhang, X.; Stoddart, J. F.; Coskun, A.; Jakubikova, E.; Chen, L. X. Electron Injection from Copper Diimine Sensitizers into TiO2: Structural Effects and Their Implications for Solar Energy Conversion Devices. *J. Am. Chem. Soc.* **2015,** *137*, 9670-9684.

(75) Katz, M. J.; DeVries Vermeer, M. J.; Farha, O. K.; Pellin, M. J.; Hupp, J. T. Dynamics of Back Electron Transfer in Dye-Sensitized Solar Cells Featuring 4-Tert-Butyl-Pyridine and Atomic-Layer-Deposited Alumina as Surface Modifiers. *J. Phys. Chem. B* **2015,** *119*, 7162-7169.

(76) Depending on TBP concentration, solvent molecules (acetonitrile), rather than TBP, may occupy the fifth of fifth and sixth coordination sites of Cu(II).

(77) Lewis-bases such as TBP have been used previously as an additional coordinating ligand to control the redox potential of certain cobalt shuttles. See M. K. Kashif, J. C. Axelson, N. W. Duffy, C. M. Forsyth, C. J. Chang, J. R. Long, L. Spiccia and U. Bach, *J. Am. Chem. Soc.*, 2012, **134**, 16646-16653.

(78) Goodwin, H. A.; Lions, F. Quadridentate Chelate Compounds. II. *J. Am. Chem. Soc.* **1960,** *82*, 5013-5023.

(79) Stoll, S.; Schweiger, A. Easyspin, a Comprehensive Software Package for Spectral Simulation and Analysis in Epr. *Journal of Magnetic Resonance* **2006,** *178*, 42-55.

(80) Davoust, C. E.; Doan, P. E.; Hoffman, B. M. Q-Band Pulsed Electron Spin-Echo Spectrometer and Its Application to Endor and Eseem. *Journal of Magnetic Resonance, Series A* **1996,** *119*, 38-44.

(81) Scholl, H. J.; Huettermann, J. Esr and Endor of Copper(II) Complexes with Nitrogen Donors: Probing Parameters for Prosthetic Group Modeling of Superoxide Dismutase. *J. Phys. Chem.* **1992,** *96*, 9684-9691.

(82) Amundsen, A. R.; Whelan, J.; Bosnich, B. Biological Analogues. On the Nature of the Binding Sites of Copper-Containing Proteins. *J. Am. Chem. Soc.* **1977,** *99*, 6730-6739.

(83) Chang, Y.-C.; Wu, H.-P.; Reddy, N. M.; Lee, H.-W.; Lu, H.-P.; Yeh, C.-Y.; Diau, E. W.-G. The Influence of Electron Injection and Charge Recombination Kinetics on the Performance of Porphyrin-Sensitized Solar Cells: Effects of the 4-Tert-Butylpyridine Additive. *Phys. Chem. Chem. Phys.* **2013,** *15*, 4651-4655.

(84) Hoffeditz, W. L.; Katz, M. J.; Deria, P.; Martinson, A. B. F.; Pellin, M. J.; Farha, O. K.; Hupp, J. T. High-Surface-Area Architectures for Improved Charge Transfer Kinetics at the Dark Electrode in Dye-Sensitized Solar Cells. *ACS Appl. Mater. Interfaces* **2014,** *6*, 8646-8650.

(85) Barnes, P. R. F.; Anderson, A. Y.; Koops, S. E.; Durrant, J. R.; O'Regan, B. C. Electron Injection Efficiency and Diffusion Length in Dye-Sensitized Solar Cells Derived from Incident Photon Conversion Efficiency Measurements. *J. Phys. Chem. C* **2009,** *113*, 1126-1136.

(86) Burschka, J.; Dualeh, A.; Kessler, F.; Baranoff, E.; Cevey-Ha, N. L.; Yi, C.; Nazeeruddin, M. K.; Gratzel, M. Tris(2-(1h-Pyrazol-1-Yl)Pyridine)Cobalt(III) as P-Type Dopant for Organic Semiconductors and Its Application in Highly Efficient Solid-State Dye-Sensitized Solar Cells. *J. Am. Chem. Soc.* **2011,** *133*, 18042-18045.

(87) Ku, Z.; Li, X.; Liu, G.; Wang, H.; Rong, Y.; Xu, M.; Liu, L.; Hu, M.; Yang, Y.; Han, H. Transparent Nis Counter Electrodes for Thiolate/Disulfide Mediated Dye-Sensitized Solar Cells. *J. Mater. Chem. A* **2013,** *1*, 237-240.

(88) Jhang, Y.-H.; Tsai, Y.-T.; Tsai, C.-H.; Hsu, S.-Y.; Huang, T.-W.; Lu, C.-Y.; Chen, M.-C.; Chen, Y.-F.; Wu, C.-C. Nanostructured Platinum Counter Electrodes by Self-Assembled Nanospheres for Dye-Sensitized Solar Cells. *Org. Electron.* **2012,** *13*, 1865-1872.

(89) Hatton, B.; Mishchenko, L.; Davis, S.; Sandhage, K. H.; Aizenberg, J. Assembly of Large-Area, Highly Ordered, Crack-Free Inverse Opal Films. *Proc. Natl. Acad. Sci. U.S.A.* **2010,** *107*, 10354-10359.

(90) Doña Rodríguez, J. M.; Herrera Melián, J. A.; Pérez Peña, J. Determination of the Real Surface Area of Pt Electrodes by Hydrogen Adsorption Using Cyclic Voltammetry. *J. Chem. Educ.* **2000,** *77*, 1195.

(91) Williams, V. O.; DeMarco, E. J.; Katz, M. J.; Libera, J. A.; Riha, S. C.; Kim, D. W.; Avila, J. R.; Martinson, A. B. F.; Elam, J. W.; Pellin, M. J.; Farha, O. K.; Hupp, J. T. Fabrication of Transparent-Conducting-Oxide-Coated Inverse Opals as Mesostructured Architectures for Electrocatalysis Applications: A Case Study with NiO. *ACS Appl. Mater. Interfaces* **2014,** *6*, 12290-12294.

(92) Hauch, A.; Georg, A. Diffusion in the Electrolyte and Charge-Transfer Reaction at the Platinum in Dye-Sensitized Solar Cells. *Electrochim. Acta* **2001,** *46*, 3457-3466.

(93) Hod, I.; Tachan, Z.; Shalom, M.; Zaban, A. Internal Photoreference Electrode: A Powerful Characterization Method for Photoelectrochemical Quantum Dot Sensitized Solar Cells. *J. Phys. Chem. Lett.* **2011,** *2*, 1032-1037.

(94) Hodes, G. Photoelectrochemical Cell Measurements: Getting the Basics Right. *J. Phys. Chem. Lett.* **2012,** *3*, 1208-1213.

(95) Zhang, X.; Peng, T.; Song, S. Recent Advances in Dye-Sensitized Semiconductor Systems for Photocatalytic Hydrogen Production. *J. Mater. Chem. A* **2016,** *4*, 2365-2402.

(96) Mahmood, A. Triphenylamine Based Dyes for Dye Sensitized Solar Cells: A Review. *Sol. Energy* **2016,** *123*, 127-144.

(97) Armaroli, N.; Balzani, V. Solar Electricity and Solar Fuels: Status and Perspectives in the Context of the Energy Transition. *Chem. Eur. J.* **2016,** *22*, 32-57.

(98) Sathiyan, G.; Sivakumar, E. K. T.; Ganesamoorthy, R.; Thangamuthu, R.; Sakthivel, P. Review of Carbazole Based Conjugated Molecules for Highly Efficient Organic Solar Cell Application. *Tetrahedron Lett.* **2016,** *57*, 243-252.

(99) Cecconi, B.; Manfredi, N.; Ruffo, R.; Montini, T.; Romero-Ocaña, I.; Fornasiero, P.; Abbotto, A. Tuning Thiophene-Based Phenothiazines for Stable Photocatalytic Hydrogen Production. *ChemSusChem* **2015,** *8*, 4216-4228.

(100) Click, K. A.; Beauchamp, D. R.; Huang, Z.; Chen, W.; Wu, Y. Membrane-Inspired Acidically Stable Dye-Sensitized Photocathode for Solar Fuel Production. *J. Am. Chem. Soc.* **2016,** *138*, 1174-1179.

(101) Ripolles-Sanchis, T.; Guo, B.-C.; Wu, H.-P.; Pan, T.-Y.; Lee, H.-W.; Raga, S. R.; Fabregat-Santiago, F.; Bisquert, J.; Yeh, C.-Y.; Diau, E. W.-G. Design and Characterization of Alkoxy-Wrapped Push-Pull Porphyrins for Dye-Sensitized Solar Cells. *Chem. Commun.* **2012,** *48*, 4368-4370.

(102) DeRosa, M. C.; Crutchley, R. J. Photosensitized Singlet Oxygen and Its Applications. *Coord. Chem. Rev.* **2002,** *233–234*, 351-371.

(103) Kytka, M.; Gerlach, A.; Schreiber, F.; Kováč, J. Real-Time Observation of Oxidation and Photo-Oxidation of Rubrene Thin Films by Spectroscopic Ellipsometry. *Appl. Phys. Lett.* **2007,** *90*, 131911.

(104) Margulies, E. A.; Wu, Y.-L.; Gawel, P.; Miller, S. A.; Shoer, L. E.; Schaller, R. D.; Diederich, F.; Wasielewski, M. R. Sub-Picosecond Singlet Exciton Fission in Cyano-Substituted Diaryltetracenes. *Angew. Chem.* **2015,** *127*, 8803-8807.

(105) Kim, D. H.; Losego, M. D.; Hanson, K.; Alibabaei, L.; Lee, K.; Meyer, T. J.; Parsons, G. N. Stabilizing Chromophore Binding on TiO2 for Long-Term Stability of Dye-Sensitized Solar Cells Using Multicomponent Atomic Layer Deposition. *Phys. Chem. Chem. Phys.* **2014,** *16*, 8615-8622.

(106) Hanson, K.; Losego, M. D.; Kalanyan, B.; Ashford, D. L.; Parsons, G. N.; Meyer, T. J. Stabilization of [Ru(Bpy)2(4,4′-(Po3h2)Bpy)]2+ on Mesoporous TiO2 with Atomic Layer Deposition of Al2O3. *Chem. Mater.* **2013,** *25*, 3-5.

(107) Jeong, N. C.; Son, H.-J.; Prasittichai, C.; Lee, C. Y.; Jensen, R. A.; Farha, O. K.; Hupp, J. T. Effective Panchromatic Sensitization of Electrochemical Solar Cells: Strategy and Organizational Rules for Spatial Separation of Complementary Light Harvesters on High-Area Photoelectrodes. *J. Am. Chem. Soc.* **2012,** *134*, 19820-19827.

(108) Splan, K. E.; Hupp, J. T. Permeable Nonaggregating Porphyrin Thin Films That Display Enhanced Photophysical Properties. *Langmuir* **2004,** *20*, 10560-10566.

(109) Lee, S. J.; Mulfort, K. L.; Zuo, X.; Goshe, A. J.; Wesson, P. J.; Nguyen, S. T.; Hupp, J. T.; Tiede, D. M. Coordinative Self-Assembly and Solution-Phase X-Ray Structural Characterization of Cavity-Tailored Porphyrin Boxes. *J. Am. Chem. Soc.* **2008,** *130*, 836-838.

(110) Wang, C.; Pålsson, L.-O.; Batsanov, A. S.; Bryce, M. R. Molecular Wires Comprising Π-Extended Ethynyl- and Butadiynyl-2,5-Diphenyl-1,3,4-Oxadiazole Derivatives: Synthesis, Redox, Structural, and Optoelectronic Properties. *J. Am. Chem. Soc.* **2006,** *128*, 3789-3799.

(111) Riha, S. C.; Libera, J. A.; Elam, J. W.; Martinson, A. B. F. Design and Implementation of an Integral Wall-Mounted Quartz Crystal Microbalance for Atomic Layer Deposition. *Rev. Sci. Instrum.* **2012,** *83*, 094101.

(112) Avila, J. R.; DeMarco, E. J.; Emery, J. D.; Farha, O. K.; Pellin, M. J.; Hupp, J. T.; Martinson, A. B. F. Real-Time Observation of Atomic Layer Deposition Inhibition: Metal Oxide Growth on Self-Assembled Alkanethiols. *ACS Appl. Mater. Interfaces* **2014,** *6*, 11891-11898.

(113) Nilsen, O.; Mohn, C. E.; Kjekshus, A.; Fjellvåg, H. Analytical Model for Island Growth in Atomic Layer Deposition Using Geometrical Principles. *J. Appl. Phys.* **2007,** *102*, 024906.

(114) Elam, J. W.; Routkevitch, D.; Mardilovich, P. P.; George, S. M. Conformal Coating on Ultrahigh-Aspect-Ratio Nanopores of Anodic Alumina by Atomic Layer Deposition. *Chem. Mater.* **2003,** *15*, 3507-3517.

(115) Cao, F.; Oskam, G.; Searson, P. C. A Solid State, Dye Sensitized Photoelectrochemical Cell. *J. Phys. Chem.* **1995,** *99*, 17071-17073.

(116) Hanson, K.; Losego, M. D.; Kalanyan, B.; Parsons, G. N.; Meyer, T. J. Stabilizing Small Molecules on Metal Oxide Surfaces Using Atomic Layer Deposition. *Nano Lett.* **2013,** *13*, 4802-4809.

(117) Klahr, B.; Hamann, T. Water Oxidation on Hematite Photoelectrodes: Insight into the Nature of Surface States through in Situ Spectroelectrochemistry. *J. Phys. Chem. C* **2014,** *118*, 10393-10399.

(118) Teng, C.; Yang, X.; Yuan, C.; Li, C.; Chen, R.; Tian, H.; Li, S.; Hagfeldt, A.; Sun, L. Two Novel Carbazole Dyes for Dye-Sensitized Solar Cells with Open-Circuit Voltages up to 1 V Based on Br−/Br3− Electrolytes. *Org. Lett.* **2009,** *11*, 5542-5545.

(119) Wu, J.; Lan, Z.; Lin, J.; Huang, M.; Huang, Y.; Fan, L.; Luo, G. Electrolytes in Dye-Sensitized Solar Cells. *Chem. Rev.* **2015,** *115*, 2136-2173.

(120) Ogunsolu, O. O.; Wang, J. C.; Hanson, K. Inhibiting Interfacial Recombination Events in Dye-Sensitized Solar Cells Using Self-Assembled Bilayers. *ACS Appl. Mater. Interfaces* **2015,** *7*, 27730-27734.

(121) Pathak, S. K.; Abate, A.; Leijtens, T.; Hollman, D. J.; Teuscher, J.; Pazos, L.; Docampo, P.; Steiner, U.; Snaith, H. J. Towards Long-Term Photostability of Solid-State Dye Sensitized Solar Cells. *Adv. Energy Mater.* **2014,** *4*, 1301667.

(122) Lau, G. P. S.; Tsao, H. N.; Yi, C.; Zakeeruddin, S. M.; Grätzel, M.; Dyson, P. J. Enhancing the Stability of Porphyrin Dye-Sensitized Solar Cells by Manipulation of Electrolyte Additives. *ChemSusChem* **2015,** *8*, 255-259.

(123) Wang, J. C.; Murphy, I. A.; Hanson, K. Modulating Electron Transfer Dynamics at Dye–Semiconductor Interfaces Via Self-Assembled Bilayers. *J. Phys. Chem. C* **2015,** *119*, 3502-3508.

(124) Kim, D. H.; Losego, M. D.; Peng, Q.; Parsons, G. N. Atomic Layer Deposition for Sensitized Solar Cells: Recent Progress and Prospects. *Adv. Mater. Interfaces* **2016,** *3*, 1600354.

(125) DeVries, M. J.; Pellin, M. J.; Hupp, J. T. Dye-Sensitized Solar Cells: Driving-Force Effects on Electron Recombination Dynamics with Cobalt-Based Shuttles. *Langmuir* **2010,** *26*, 9082-9087.

(126) Johansson, P. G.; Kopecky, A.; Galoppini, E.; Meyer, G. J. Distance Dependent Electron Transfer at TiO_2 Interfaces Sensitized with Phenylene Ethynylene Bridged Ru^{II}–Isothiocyanate Compounds. *J. Am. Chem. Soc.* **2013,** *135*, 8331-8341.

(127) Pettersson, K.; Wiberg, J.; Ljungdahl, T.; Mårtensson, J.; Albinsson, B. Interplay between Barrier Width and Height in Electron Tunneling: Photoinduced Electron Transfer in Porphyrin-Based Donor−Bridge−Acceptor Systems. *J. Phys. Chem. A* **2006,** *110*, 319-326.

(128) Wenger, O. S. How Donor−Bridge−Acceptor Energetics Influence Electron Tunneling Dynamics and Their Distance Dependences. *Acc. Chem. Res.* **2011,** *44*, 25-35.

(129) Davis, W. B.; Ratner, M. A.; Wasielewski, M. R. Conformational Gating of Long Distance Electron Transfer through Wire-Like Bridges in Donor−Bridge−Acceptor Molecules. *J. Am. Chem. Soc.* **2001,** *123*, 7877-7886.

(130) Hayes, R. T.; Wasielewski, M. R.; Gosztola, D. Ultrafast Photoswitched Charge Transmission through the Bridge Molecule in a Donor−Bridge−Acceptor System. *J. Am. Chem. Soc.* **2000,** *122*, 5563-5567.

(131) Jin, S.; Tagliazucchi, M.; Son, H.-J.; Harris, R. D.; Aruda, K. O.; Weinberg, D. J.; Nepomnyashchii, A. B.; Farha, O. K.; Hupp, J. T.; Weiss, E. A. Enhancement of the Yield of Photoinduced Charge Separation in Zinc Porphyrin–Quantum Dot Complexes by a Bis(Dithiocarbamate) Linkage. *J. Phys. Chem. C* **2015,** *119*, 5195-5202.

(132) Brennan, T. P.; Bakke, J. R.; Ding, I. K.; Hardin, B. E.; Nguyen, W. H.; Mondal, R.; Bailie, C. D.; Margulis, G. Y.; Hoke, E. T.; Sellinger, A.; McGehee, M. D.; Bent, S. F. The Importance of Dye Chemistry and $TiCl_4$ Surface Treatment in the Behavior of Al_2O_3 Recombination Barrier Layers Deposited by Atomic Layer Deposition in Solid-State Dye-Sensitized Solar Cells. *Phys. Chem. Chem. Phys.* **2012,** *14*, 12130-12140.

(133) Zaban, A.; Greenshtein, M.; Bisquert, J. Determination of the Electron Lifetime in Nanocrystalline Dye Solar Cells by Open-Circuit Voltage Decay Measurements. *ChemPhysChem* **2003,** *4*, 859-864.

(134) Edwards, P. P.; Gray, H. B.; Lodge, M. T. J.; Williams, R. J. P. Electron Transfer and Electronic Conduction through an Intervening Medium. *Angew. Chem. Int. Ed.* **2008,** *47*, 6758-6765.

(135) Guo, Z.; Ambrosio, F.; Pasquarello, A. Oxygen Defects in Amorphous Al_2O_3: A Hybrid Functional Study. *Appl. Phys. Lett.* **2016,** *109*, 062903.

(136) Avila, J. R.; Katz, M. J.; Farha, O. K.; Hupp, J. T. Barrier-Layer-Mediated Electron Transfer from Semiconductor Electrodes to Molecules in Solution: Sensitivity of Mechanism to Barrier-Layer Thickness. *J. Phys. Chem. C* **2016,** *120*, 20922-20928.

(137) Li, Z.; Park, T.-H.; Rawson, J.; Therien, M. J.; Borguet, E. Quasi-Ohmic Single Molecule Charge Transport through Highly Conjugated Meso-to-Meso Ethyne-Bridged Porphyrin Wires. *Nano Lett.* **2012,** *12*, 2722-2727.

(138) Sedghi, G.; Garcia-Suarez, V. M.; Esdaile, L. J.; Anderson, H. L.; Lambert, C. J.; Martin, S.; Bethell, D.; Higgins, S. J.; Elliott, M.; Bennett, N.; Macdonald, J. E.; Nichols, R. J. Long-Range Electron Tunnelling in Oligo-Porphyrin Molecular Wires. *Nat Nano* **2011,** *6*, 517-523.

(139) Gilbert Gatty, M.; Kahnt, A.; Esdaile, L. J.; Hutin, M.; Anderson, H. L.; Albinsson, B. Hopping Versus Tunneling Mechanism for Long-Range Electron Transfer in Porphyrin Oligomer Bridged Donor–Acceptor Systems. *J. Phys. Chem. B* **2015,** *119*, 7598-7611.

(140) Correa Baena, J. P.; Steier, L.; Tress, W.; Saliba, M.; Neutzner, S.; Matsui, T.; Giordano, F.; Jacobsson, T. J.; Srimath Kandada, A. R.; Zakeeruddin, S. M.; Petrozza, A.; Abate, A.; Nazeeruddin, M. K.; Gratzel, M.; Hagfeldt, A. Highly Efficient Planar Perovskite Solar Cells through Band Alignment Engineering. *Energy Environ. Sci.* **2015,** *8*, 2928-2934.

(141) Zhou, H.; Chen, Q.; Li, G.; Luo, S.; Song, T.-b.; Duan, H.-S.; Hong, Z.; You, J.; Liu, Y.; Yang, Y. Interface Engineering of Highly Efficient Perovskite Solar Cells. *Science* **2014,** *345*, 542-546.

(142) Jain, S. M.; Qiu, Z.; Haggman, L.; Mirmohades, M.; Johansson, M. B.; Edvinsson, T.; Boschloo, G. Frustrated Lewis Pair-Mediated Recrystallization of $CH_3NH_3PbI_3$ for Improved Optoelectronic Quality and High Voltage Planar Perovskite Solar Cells. *Energy Environ. Sci.* **2016**, DOI:10.1039/C1036EE02544G.

(143) Arora, N.; Orlandi, S.; Dar, M. I.; Aghazada, S.; Jacopin, G.; Cavazzini, M.; Mosconi, E.; Gratia, P.; De Angelis, F.; Pozzi, G.; Graetzel, M.; Nazeeruddin, M. K. High Open-Circuit Voltage: Fabrication of Formamidinium Lead Bromide Perovskite Solar Cells Using Fluorene–Dithiophene Derivatives as Hole-Transporting Materials. *ACS Energy Letters* **2016,** *1*, 107-112.

(144) Dong, C.; Xiang, W.; Huang, F.; Fu, D.; Huang, W.; Bach, U.; Cheng, Y.-B.; Li, X.; Spiccia, L. Controlling Interfacial Recombination in Aqueous Dye-Sensitized Solar Cells by Octadecyltrichlorosilane Surface Treatment. *Angew. Chem. Int. Ed.* **2014,** *53*, 6933-6937.

(145) Williams, V. O.; Jeong, N. C.; Prasittichai, C.; Farha, O. K.; Pellin, M. J.; Hupp, J. T. Fast Transporting ZnO–TiO_2 Coaxial Photoanodes for Dye-Sensitized Solar Cells Based on Ald-Modified SiO_2 Aerogel Frameworks. *ACS Nano* **2012,** *6*, 6185-6196.

(146) Li, T. C.; Góes, M. S.; Fabregat-Santiago, F.; Bisquert, J.; Bueno, P. R.; Prasittichai, C.; Hupp, J. T.; Marks, T. J. Surface Passivation of Nanoporous TiO_2 Via Atomic Layer Deposition of ZrO_2 for Solid-State Dye-Sensitized Solar Cell Applications. *J. Phys. Chem. C* **2009,** *113*, 18385-18390.

(147) Liang, J.; Zhang, G.; Sun, W. Post-Treatment on Dye-Sensitized Solar Cells with $TiCl_4$ and Nb_2O_5. *RSC Advances* **2014,** *4*, 6746-6751.

(148) Barea, E.; Xu, X.; Gonzalez-Pedro, V.; Ripolles-Sanchis, T.; Fabregat-Santiago, F.; Bisquert, J. Origin of Efficiency Enhancement in Nb2O5 Coated Titanium Dioxide Nanorod Based Dye Sensitized Solar Cells. *Energy Environ. Sci.* **2011,** *4*, 3414-3419.

(149) Ahn, K.-S.; Kang, M.-S.; Lee, J.-K.; Shin, B.-C.; Lee, J.-W. Enhanced Electron Diffusion Length of Mesoporous TiO2 Film by Using Nb2O5 Energy Barrier for Dye-Sensitized Solar Cells. *Appl. Phys. Lett.* **2006,** *89*, 013103.

(150) Chen, S. G.; Chappel, S.; Diamant, Y.; Zaban, A. Preparation of Nb2O5 Coated TiO2 Nanoporous Electrodes and Their Application in Dye-Sensitized Solar Cells. *Chem. Mater.* **2001,** *13*, 4629-4634.

(151) Le Viet, A.; Jose, R.; Reddy, M. V.; Chowdari, B. V. R.; Ramakrishna, S. Nb2O5 Photoelectrodes for Dye-Sensitized Solar Cells: Choice of the Polymorph. *J. Phys. Chem. C* **2010,** *114*, 21795-21800.

(152) Lenzmann, F.; Krueger, J.; Burnside, S.; Brooks, K.; Grätzel, M.; Gal, D.; Rühle, S.; Cahen, D. Surface Photovoltage Spectroscopy of Dye-Sensitized Solar Cells with TiO_2, Nb_2O_5, and $SrTiO_3$ Nanocrystalline Photoanodes: Indication for Electron Injection from Higher Excited Dye States. *J. Phys. Chem. B* **2001,** *105*, 6347-6352.

(153) Blanquart, T.; Niinistö, J.; Heikkilä, M.; Sajavaara, T.; Kukli, K.; Puukilainen, E.; Xu, C.; Hunks, W.; Ritala, M.; Leskelä, M. Evaluation and Comparison of Novel Precursors for Atomic Layer Deposition of Nb2O5 Thin Films. *Chem. Mater.* **2012,** *24*, 975-980.

(154) Vratny, F.; Micale, F. Reflectance Spectra of Non-Stoichiometric Titanium Oxide, Niobium Oxide, and Vanadium Oxide. *Transactions of the Faraday Society* **1963,** *59*, 2739-2749.

(155) Scaife, D. E. Oxide Semiconductors in Photoelectrochemical Conversion of Solar Energy. *Sol. Energy* **1980,** *25*, 41-54.

(156) Sayama, K.; Sugihara, H.; Arakawa, H. Photoelectrochemical Properties of a Porous Nb2O5 Electrode Sensitized by a Ruthenium Dye. *Chem. Mater.* **1998,** *10*, 3825-3832.

(157) Cardon, F.; Gomes, W. P. On the Determination of the Flat-Band Potential of a Semiconductor in Contact with a Metal or an Electrolyte from the Mott-Schottky Plot. *J. Phys. D: Appl. Phys.* **1978,** *11*, L63.

(158) De Gryse, R.; Gomes, W. P.; Cardon, F.; Vennik, J. On the Interpretation of Mott-Schottky Plots Determined at Semiconductor/Electrolyte Systems. *J. Electrochem. Soc.* **1975,** *122*, 711-712.

(159) Gelderman, K.; Lee, L.; Donne, S. W. Flat-Band Potential of a Semiconductor: Using the Mott–Schottky Equation. *J. Chem. Educ.* **2007,** *84*, 685.

(160) Cameron, P. J.; Peter, L. M. Characterization of Titanium Dioxide Blocking Layers in Dye-Sensitized Nanocrystalline Solar Cells. *J. Phys. Chem. B* **2003,** *107*, 14394-14400.

(161) Albery, W. J.; O'Shea, G. J.; Smith, A. L. Interpretation and Use of Mott-Schottky Plots at the Semiconductor/Electrolyte Interface. *J. Chem. Soc., Faraday Trans.* **1996,** *92*, 4083-4085.

(162) Kukli, K.; Ritala, M.; Leskelä, M. Development of Dielectric Properties of Niobium Oxide, Tantalum Oxide, and Aluminum Oxide Based Nanolayered Materials. *J. Electrochem. Soc.* **2001,** *148*, F35-F41.

(163) Störmer, H.; Weber, A.; Fischer, V.; Ivers-Tiffée, E.; Gerthsen, D. Anodically Formed Oxide Films on Niobium: Microstructural and Electrical Properties. *J. Eur. Ceram. Soc.* **2009,** *29*, 1743-1753.

(164) Jung, H. S.; Kim, H. Origin of Low Photocatalytic Activity of Rutile TiO2. *Electronic Materials Letters* **2009,** *5*, 73-76.

(165) Ohsawa, T.; Okubo, J.; Suzuki, T.; Kumigashira, H.; Oshima, M.; Hitosugi, T. An N-Type Transparent Conducting Oxide: Nb12o29. *J. Phys. Chem. C* **2011,** *115*, 16625-16629.

(166) Zaban, A.; Chen, S. G.; Chappel, S.; Gregg, B. A. Bilayer Nanoporous Electrodes for Dye Sensitized Solar Cells. *Chem. Commun.* **2000**, 2231-2232.

(167) Hejin Park, H.; Heasley, R.; Gordon, R. G. Atomic Layer Deposition of Zn(O,S) Thin Films with Tunable Electrical Properties by Oxygen Annealing. *Appl. Phys. Lett.* **2013,** *102*, 132110.

(168) Dang, V.-S.; Parala, H.; Kim, J. H.; Xu, K.; Srinivasan, N. B.; Edengeiser, E.; Havenith, M.; Wieck, A. D.; de los Arcos, T.; Fischer, R. A.; Devi, A. Electrical and Optical Properties of TiO2 Thin Films Prepared by Plasma-Enhanced Atomic Layer Deposition. *physica status solidi (a)* **2014,** *211*, 416-424.

(169) Lee, B. H.; Jeon, Y.; Zawadzki, K.; Qi, W.-J.; Lee, J. Effects of Interfacial Layer Growth on the Electrical Characteristics of Thin Titanium Oxide Films on Silicon. *Appl. Phys. Lett.* **1999,** *74*, 3143-3145.

(170) Wilk, G. D.; Wallace, R. M.; Anthony, J. M. High-K Gate Dielectrics: Current Status and Materials Properties Considerations. *J. Appl. Phys.* **2001,** *89*, 5243-5275.

(171) Lyon, L. A.; Hupp, J. T. Energetics of the Nanocrystalline Titanium Dioxide/Aqueous Solution Interface: Approximate Conduction Band Edge Variations between H0 = −10 and H- = +26. *J. Phys. Chem. B* **1999,** *103*, 4623-4628.

(172) Augustyn, V.; Simon, P.; Dunn, B. Pseudocapacitive Oxide Materials for High-Rate Electrochemical Energy Storage. *Energy Environ. Sci.* **2014,** *7*, 1597-1614.